

## **2 RESEARCH ACHIEVEMENTS OF THE CRPP IN 1999**

The main experimental device at the CRPP is the tokamak TCV (Tokamak à Configuration Variable). TCV is being equipped with a powerful electron cyclotron heating scheme: when completed the additional heating will allow the injection of 4.5MW of radio frequency power. The primary goal of TCV is the study of confinement of particle and energy as the plasma shape is modified.

The theoretical studies of magnetic confinement systems have concentrated on exploring new configurations in the 3D geometry of the stellarator family. Such work is necessary in the long term, since even if the tokamak is the most advanced magnetic confinement system known at present, the inherent advantages of a stellarator justify pursuing this parallel line of research. Both tokamaks and stellarators exhibit enhanced transport losses experimentally and studying the reasons is the second pillar of the theory group at the CRPP. Understanding these losses might lead to ideas for reducing them, which could have an enormous impact on all magnetic confinement devices.

The CRPP participates in the design and development of high power gyrotrons for fusion research, not only at the CRPP but also for other magnetic confinement experiments. These systems are evolving in the direction of maximising the pulse length at their nominal power.

Constructing a thermonuclear reactor would require two major technical developments, namely improving the available materials for the innermost part of the reactor and improving the superconducting magnet systems for providing the magnetic fields which are the fundamental components of a magnetic confinement system. These two activities are both pursued at the CRPP in its Villigen laboratories.

Plasmas are not only of interest for magnetic confinement, but are also becoming recognised more and more as a valuable and economical tool in various areas of industrial production. The underlying knowledge and experience of plasma physics at the CRPP is being put to good use in a series of industrial partnerships to promote plasma processing in industry and to help industry with specific problems related to their plasma systems. These activities are expanding at present, limited by the available personnel rather than the possible scope of activities and are performed outside the frame of the Association EURATOM-Confédération Suisse.

This very broad scope of activities range from long calculations on the world's fastest super-computers for the rather exotic field of magnetic confinement of high temperature plasmas to the quest for better and faster preparation of machine tool surfaces or packaging surfaces and makes the CRPP an extremely good example of the importance of studying, understanding and mastering the 4<sup>th</sup> state of matter, namely the plasma state. The remainder of this section is devoted to the detailed results of all of these studies during 1999.

## **2.1 The TCV tokamak**

It has become clear over the last few years that the success of economically viable tokamak based thermonuclear reactors, of which ITER would be an experimental prototype, relies heavily on the achievement of high performance regimes. Gains in the maximum plasma pressure without instabilities of the plasma magnetic confinement as well as improvements to the tokamak confinement can be obtained by adjusting the spatial variation, usually called the profile, of important plasma parameters such as the plasma pressure or the electrical current as well as by an appropriate choice of the plasma geometry.

TCV is well suited for work in this promising direction. Its additional heating system using EC wave beams can target very precise locations in the plasma and therefore finely modify the temperature and current density profiles. This system so far consists of 6 gyrotrons delivering 0.5MW each whose frequency is selected to resonate with the electron cyclotron motion. The launching direction of each of the 6 narrow beams can be adjusted by mobile mirrors, in both vertical and horizontal directions, giving a large freedom of choice of the region in the plasma to be heated. During 1999, three of these beams were routinely available and the remaining three became operational only at the end of the year. TCV also has a world-wide unique shaping system that allows the creation of a huge variety of cross-section shapes up to very high elongation, giving control of the main plasma and divertor geometry. This overview highlights the most salient progress made on TCV during 1999 while later sections give more details.

**High performance ECH plasma:** Advanced studies for operational schemes of a tokamak reactor showed the importance of regimes in which the plasma current necessary for confining the plasma is continuously driven by electromagnetic waves. The goal is to avoid the plasma current being inductively sustained by an external transformer whose current swing capability limits the pulse duration to less than an hour. EC waves launched with a parallel component to the magnetic field can generate suprathermal electrons leading to a driven current.

For the first time on a tokamak, a 2 second pulse was maintained in TCV using as sole current source three EC beams of 0.5MW each, without any induction from the transformer, in a plasma with some of the reactor relevant parameters. Additionally the ability of the system to target specific locations within the plasma was essential to tune the power spatial distribution, in order to guarantee plasma stability and thus to reach steady-state conditions.

It has been discovered during the last decade that the plasma performance in terms of confinement quality, a crucial point for future reactors, depends closely on the spatial distribution of the plasma current. It is thought that controlling the shear in the magnetic field lines through an appropriate tailoring of this current distribution helps in suppressing most of the turbulence responsible for heat losses.

Again combining the spatial precision of the EC beams and their local influence on the electrical current, substantial improvement in the global thermal energy confinement time of 40% and a record electron temperature for TCV of 10keV were obtained. The well-known transition from L-mode (low confinement) to H-mode (high confinement) was also achieved while injecting 1.5MW of ECH.

**Physics of ECH plasmas:** Achievement of high performance ECH plasmas implies a good understanding of the underlying physical processes. This fundamental study encompasses several aspects.

The distribution function of the suprathermal electrons created during Electron Cyclotron Current Drive (ECCD) pulses has been experimentally studied through measurements of the associated bremsstrahlung emission spectrum. Agreement between the emission intensity and its photon temperature with the wave propagation angle and the current drive efficiency brings additional confidence to our understanding.

EC experiments are complemented by an experimental determination of the spatial distribution of the ECH heat deposition based on the dynamic response of the thermal energy content of the plasma. Applying appropriate signal processing to available measurements yields an experimental estimation of the absorbed power as well as the absorption location. These can corroborate simulation predictions despite the complexity of the wave launching and the beam propagation.

Very localised ECH heat deposition is a useful tool for studying the internal stability of the plasma. Unstable phenomena may affect the performance of a fusion burning plasma but may also help preventing ash and impurity accumulation in the plasma core. High spatial and temporal resolution tomography of the soft X-ray emissivity allowed us to follow the growth and relaxation of the so called "sawtooth" instability, associated with the presence of a magnetic island, which is perturbed by central ECH power deposition. These experimental results have been simulated by a heuristic model. High power injection in the plasma core also lead to the onset of neoclassical tearing modes, also linked to magnetic islands, which may ultimately impose a crucial limitation in thermonuclear regime plasmas.

**Plasma shaping:** The main advantage of an elongated cross-section compared with a circular plasma is the potential increase in the maximum sustainable plasma current: an elongation of 3 for example gives an increase of a factor 5 in the current. This in turn brings improvement in the maximum plasma pressure and in the energy confinement time characterising the quality of the thermal insulation. During 1999, elongations up to 2.64 were achieved, the highest elongation ever produced in a conventional aspect ratio tokamak. The drawback of high elongation configurations is the necessity of a fast vertical position feedback loop. These configurations have been made possible by continuous optimisation of the vertical position control system combined with the development of adequate and now experimentally tested models for the plasma vertical deformation.

The shaping capabilities of TCV can also be applied to vary the geometry of the divertor, which is located outside the hot plasma and whose magnetic topology controls the interaction between the particles escaping the main plasma and the vessel walls. Reducing the associated heat load to technologically acceptable levels on tokamak reactors remains a key issue. A particularity of the TCV divertor, despite the small size of the machine, is that the connection length of the field line trajectory from the main plasma to the wall can be increased to values comparable to ITER. The spread of the heat flux on the wall can also be widely varied. Divertor operation regimes have been explored with a growing set of measurements to provide valuable information for benchmarking divertor simulation codes.

Appropriate plasma shaping during the formation of the plasma has also proved to be a way of avoiding its premature termination by a so-called locked mode disruption. Disruption control is important for reactor size tokamaks because disruptions generate large electrical and mechanical stresses.

The wide variety of shapes has also been used to substantiate a theory based on the role of the magnetic entropy in the plasma equilibrium.

### **2.1.1 High performance ECH plasmas**

#### **Full ECCD**

A steady-state, fully non-inductive plasma current has been sustained for the first time in a tokamak using electron cyclotron current drive only. In this discharge, 123kA of current were sustained for the entire gyrotron pulse duration of 2s. Careful distribution of the power deposited from three 0.5MW gyrotrons across the plasma minor radius was essential for reaching steady-state conditions. With central current drive, up to 153kA of current was driven transiently for 100ms. The non-inductive scenario is confirmed by the ability to recharge the Ohmic transformer. The dependence of the current drive efficiency on the minor radius has also been investigated.

First, using 2 gyrotrons, we demonstrated the steady recharging of the Ohmic transformer at a rate of about 1kA/s for 1.5s at  $I_p=80\text{kA}$ ,  $n_{e0}=1.9\cdot 10^{19}\text{m}^{-3}$  with 1MW of on-axis ECCD. This was obtained with toroidal launch angles of  $35^\circ$ . Using 3 gyrotrons, 1.5MW, aiming at the plasma centre in order to maximise the current drive efficiency, which depends on the local temperature, we replaced 153kA of plasma current for about 100ms. This yields a current drive of 0.013 [ $10^{20}\text{A/Wm}^2$ ], after correction for about 20% of bootstrap current. However the driven current profile in this configuration is too peaked and is MHD unstable, which is why the discharges disrupt after about 100ms which is of the order of the current redistribution time. Therefore we had to distribute the deposited power over the minor radius, albeit losing some efficiency due to lower temperature. The control of the driven current profile was obtained by changing the poloidal angles of the mirrors such that one beam aims at the plasma centre, one at  $r/a\sim 0.3$  and one at  $r/a\sim 0.5$ . In this way a broader current profile was obtained and no MHD activity was observed. An example of full current replacement for the whole gyrotron pulse is shown in Fig. 2.1.1. The current in the transformer is constant as soon as the ECCD is turned on, indicating that no current is induced in the plasma anymore. The time evolution of internal inductance and elongation ( ) indicated the current redistribution time. The plasma current in this case is 123kA, with  $n_e=10^{19}\text{m}^{-3}$ ,  $T_{e0}\sim 3.5\text{keV}$  and we estimate about 15% of bootstrap current. The average current drive efficiency is about 0.006 in agreement with the results obtained with the ray-tracing code.

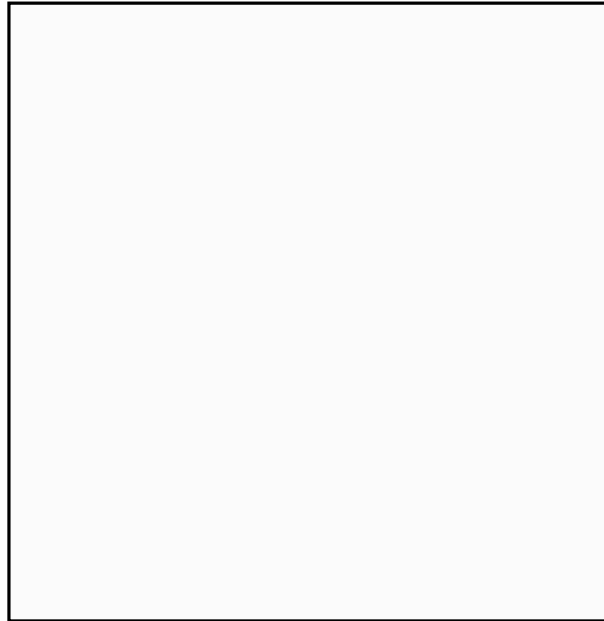


**Fig. 2.1.1**      ***Demonstration of steady-state non-inductive current drive on TCV***

We were also able to measure accurately the amount of current driven by the outermost beam, at  $r/a \sim 0.5$ . This was obtained by comparing shots with this beam in heating, toroidal angle  $= 0^\circ$ , and ECCD, toroidal angle  $= 35^\circ$ , modes. Either by comparing the difference in loop voltage or the difference in total plasma current that the 3 beams can fully replace, we obtained about 8kA difference. This shows that the local efficiency, normalised to the local temperature, is not constant over the minor radius as was found on the DIII-D tokamak. This is in agreement with a loss of current drive efficiency due to the particle trapping effect. Our results are much closer to the theoretical value obtained with TORAY, even though still about two times larger.

### **Temperature and density profile modification by ECH and ECCD**

The current distribution can be modified both by ECH, increasing the temperature and therefore the plasma conductivity locally, and by ECCD. The driven current over and above that obtained just from the heating was studied by scanning the toroidal launching angles in the co- and counter-ECCD directions, with both on axis and near  $q=1$  power deposition. The parameters were  $I_p=170\text{kA}$ ,  $\langle n_e \rangle \sim 1 \cdot 10^{19}\text{m}^{-3}$ ,  $\nu = 1.25$ ,  $P_{\text{ECH}}=1.5\text{MW}$ . The resulting temperature profiles are shown in Fig. 2.1.2 for on-axis deposition for counter-ECCD (toroidal angle  $= -28^\circ$ ) and for co-ECCD (toroidal angle  $= +21^\circ$ ) together with the ECH case and the Ohmic target plasma. The horizontal axis is the height of the measurement along the vertical Thomson scattering laser beam, at  $R=0.88\text{m}$ . The continuous lines correspond to fitted profiles with the constraint that the temperatures be constant on the reconstructed magnetic surfaces. Maximum temperatures around 5keV on axis are obtained both with ECH and co-ECCD. With counter-ECCD, extremely peaked electron temperature profiles are generated with over 10keV on axis. Even in the case of deposition off-axis near  $r/a=0.3$ , the temperature profiles remain fairly peaked, with peak temperatures in the range 2-3keV, as long as some of the ECH power is deposited inside the  $q=1$  surface. When all the deposition is well outside the  $q=1$  surface,  $r/a=0.7$ , the temperature profile is rather flat, with central

electron temperatures close to the Ohmic conditions, as shown in Fig. 2.1.3, indicating poor retention of the additional energy.

Counter-ECCD deposited near the magnetic axis improved the central energy confinement with a twofold increase of the central electron temperature and the formation of a steep core temperature gradient. The central heat transfer coefficient deduced from profile analysis is found to decrease by a factor of 4.0 and the global electron energy confinement time increases by a factor of 2.0 in these discharges, compared with plasmas with ECH alone or co-ECCD. The confinement improvement in the case of central counter current drive reached a factor of 3.0 above RLW and TCV-IAEA-98 scalings, whereas for central ECH it only reached a factor of 1.5 above the same.

Simulations by the PRETOR transport code suggest that this improved confinement could be due to sawtooth stabilisation induced by the central safety factor  $q_0$  rising above unity;  $q_0 < 1$  for co-ECCD and ECH discharges in which sawtooth activity is observed. This result is in agreement with the experiment, as sawteeth are present in discharges with central co-ECCD or ECH but not with counter-ECCD. The poorer central confinement observed in sawtooth discharges is due to the periodic core energy relaxations during the sawtooth crashes. Removing sawteeth from the model, the confinement and temperatures dramatically increase to the experimental values found.

Changes to the electron density profile induced by ECH and ECCD depend on the deposition location. With deposition inside the sawtooth inversion radius, density "pump-out" from the core is observed on a time scale of a few milliseconds, while an overall density increase is observed over a longer timescale. Within the first 5-10ms after ECH or ECCD turn-on, the central electron density can drop by some 10%, but with no clear dependence on the value of the ECH power. The density profiles can even become hollow with central deposition. The pump-out phenomenon is not yet explained, while the rise in total particle content is believed to result from increased particle sources at the walls, attributable to the increased power load. Power deposition outside the inversion radius causes a reduction of the local density, resulting in density profile peaking.

Unlike thermal transport, particle transport does not vary appreciably from ECH to co-ECCD or counter-ECCD: while the temperature profile peaks significantly in the counter-ECCD case, the density profile remains the same.

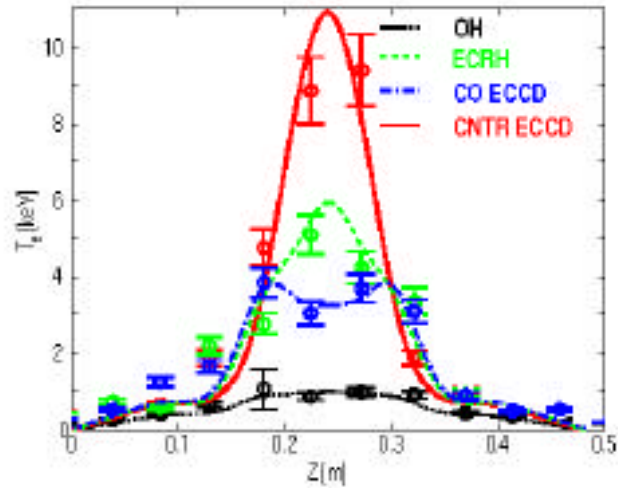


**Fig. 2.1.2** *Electron temperature profiles with counter-ECCD ( $-28^\circ$  toroidal injection angle) and co-ECCD ( $+21^\circ$  toroidal injection angle) and with ECH. An Ohmic case is shown for reference. The power deposition is central.*

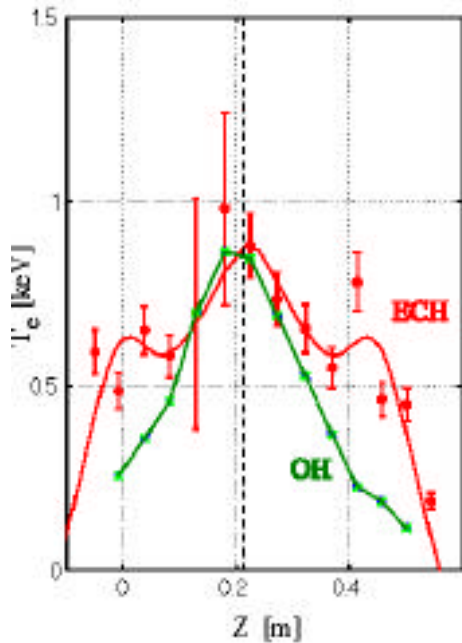


**Fig. 2.1.3** *Electron temperature profile for far off-axis heating near  $r/a=0.7$  and for the corresponding Ohmic phase.*

### L-mode to H-mode transitions in ECH plasmas

The region of the operational domain where the Ohmic H-mode is accessible is quite large in TCV. One operational boundary is the plasma density: H-modes were only obtained in plasmas with a line average density larger than  $3.5 \cdot 10^{19} \text{m}^{-3}$ . With the toroidal magnetic field of 1.5T, the EC 2nd harmonic frequency is cut off at local densities greater than  $4.25 \cdot 10^{19} \text{m}^{-3}$ . In order that at least half of the minor radius be accessible to the EC wave, the plasma line average density had to be maintained below  $3.5 \cdot 10^{19} \text{m}^{-3}$ . Nevertheless, LH transitions were observed at these lower densities in ECH plasmas. A new low density limit was observed at  $\sim 2.5 \cdot 10^{19} \text{m}^{-3}$ : below this density, LH transitions have not been observed despite the

1.5MW of ECH power, as shown in Fig. 2.1.4. In the narrow range of density where the H-mode was accessible, the threshold power appeared to increase as the plasma density decreases, a result in contradiction with the behaviour in Ohmic plasmas. Although further experiments are required to confirm it, no significant dependence of the threshold power on the plasma shape was observed.

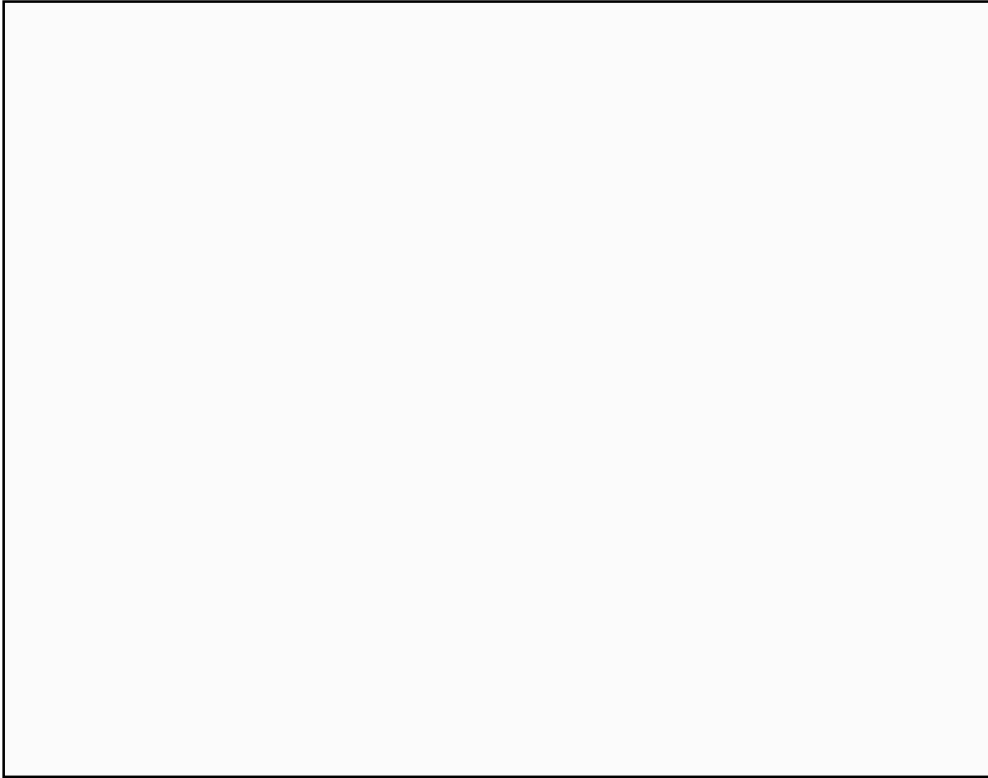


**Fig. 2.1.4** *Threshold power as a function of the plasma density. The vertical lines indicate the low density limits with Ohmic and ECH heating. L-mode time slices are shown for densities below  $2.5 \cdot 10^{19} \text{m}^{-3}$  in order to indicate the range of density and power where LH transitions were not obtained.*

## **2.1.2 Physics of ECH plasmas**

### **Fast electron dynamics**

A multichordal hard X-ray camera, on loan from the CEA (Cadarahe, France), has been used to study the distribution in space and energy, as well as the temporal dynamics, of bremsstrahlung emission from suprathermal electrons during ECCD experiments with up to 1.5MW of injected power. The resolution of the measurement is  $\sim 2\text{cm}$  in space,  $\sim 7\text{keV}$  in energy in the range 10-200keV and  $\sim 2\text{-}5\text{ms}$  in time. A clear non-Maxwellian tail in the electron distribution function, characterised by effective photon temperatures in the 20-50keV range, has been identified in all cases in which the toroidal injection angle was larger than  $\sim 10^\circ$ . The hard X-ray intensity increases with the angle, in both the co- and counter-ECCD directions (Fig. 2.1.5); this is consistent with the behaviour of the current drive efficiency, which has also been found to be higher at larger angles. In the pure heating case ( $0^\circ$  injection), the photon temperature is in agreement with the

electron temperature measured by Thomson scattering, indicating that the distribution is Maxwellian under those conditions.

To study the fast electron dynamics on a fast time scale, we have modulated the ECCD power and added the photon counts over several successive intervals. We have thereby obtained an effective resolution of 0.3ms, well below the characteristic relaxation time which is found to be in the order of 1-3ms (Fig. 2.1.6) and consistent with the collisional slowing-down time for electrons in the energy range under consideration.

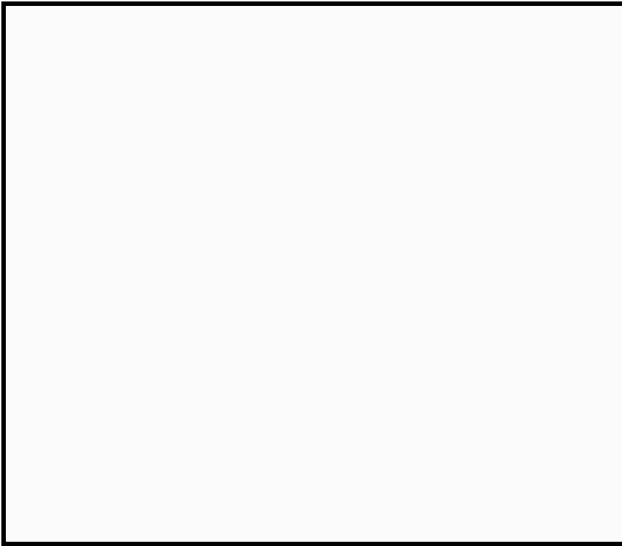


**Fig. 2.1.5** *Hard X-ray emission from the plasma centre in the 40-50keV range as a function of the toroidal injection angle with 1.5MW of central ECCD.*



**Fig. 2.1.6** *Hard X-ray emission for four different energies and ECCD power vs time (central co-ECCD). The photon counts are summed over 10 successive modulation periods.*

### Experimental determination of the ECH deposition profile

The dynamic response to ECH power variation, seen in of the electron temperature inferred from the soft X-ray emissivity, has been studied to determine the power deposition profile. Several excitations have already been analysed, such as square wave modulations and time evolution at the turn on/off of the ECH. To diminish the pollution of the signals due to the sawtooth instability, a method based on the Generalized Singular Value Decomposition (GSVD) has been developed. It was possible to reduce the sawtooth contribution on average by a factor of 10. Together with the diamagnetic loop, used to estimate the power absorbed by the plasma, the GSVD has also been successfully applied to treat the signals at the shut off of the ECH, with the purpose of developing a fast guess power deposition localisation procedure to be applied after each discharge.

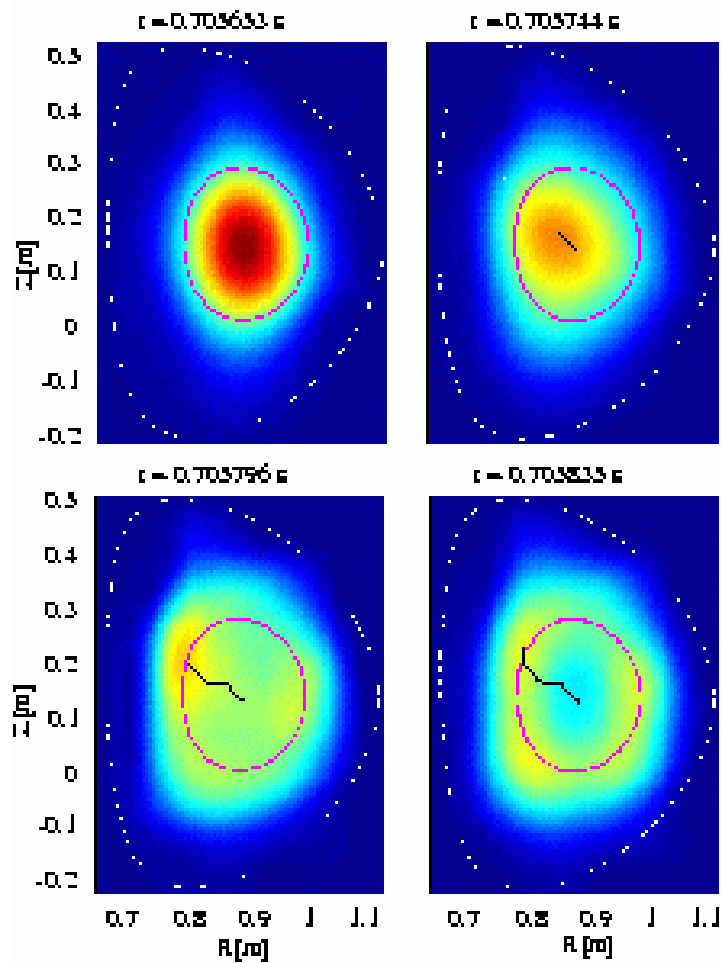


*Fig. 2.1.7* Soft X-ray tomography showing the transformation of a peaked profile into a hollow profile during the sawtooth crash, with central power deposition.

### Sawtooth modelling with localised ECH

A heuristic model for the interpretation of the variety of sawteeth observed with ECH in TCV has been developed. It includes the combined effects of the  $m=1$

magnetic island dynamics, a localised heat source, significant heat diffusivity along field lines, finite cross field heat diffusivity and plasma rotation. The model also includes the convective kink-like motion associated with the reconnection process. In the experiment, the presence of convective motion during the reconnection process is revealed by dramatic changes to the profiles during the rapid sawtooth crash. The characteristic convection time is shorter than the radial transport time. In the case of central power deposition, the tomographically reconstructed soft X-ray profile appears peaked just before the crash, then, while displacing to the side during the crash, is gradually transformed into a ring shaped, hollow profile, as shown in Fig. 2.1.7. The same picture is seen in the Thomson scattering electron temperature profiles. These effects are also found in the model simulations, which show the gradual transformation of the centrally heated, peaked profile, into a hollow profile after crash, as a result of the convective flow, as shown in Fig. 2.1.8.

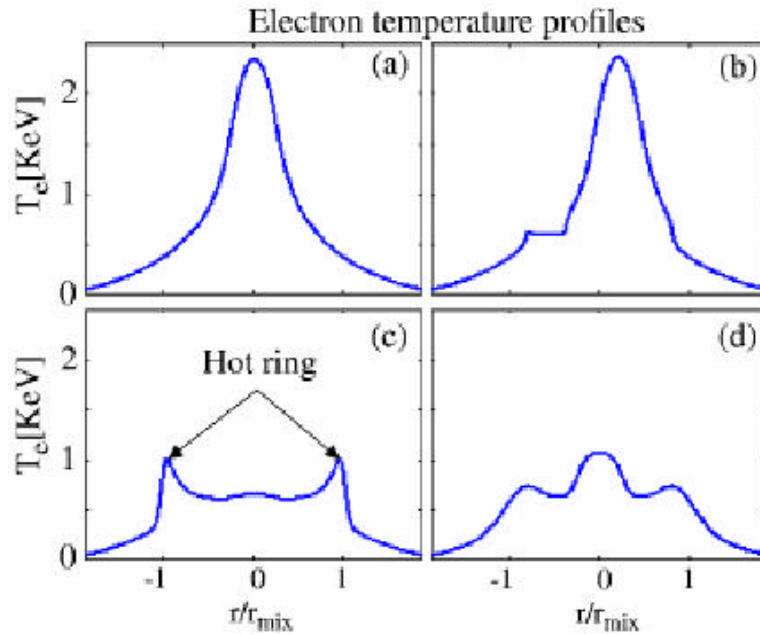


**Fig. 2.1.8** *Simulated electron temperature profiles during a triangular sawtooth with on-axis ECH power deposition: (a) pre-crash phase; (b) during the hot core displacement; (c) at complete magnetic reconnection, just after the sawtooth crash the hot ring is formed; (d) early during reheat ramp.*

### Neoclassical tearing modes

The onset of neoclassical tearing modes has been observed in TCV discharges when additional ECH power of at least 1MW was applied in the plasma centre. These modes have an  $m/n=2/1$  or  $3/2$  structure and have been observed with magnetic fluctuation measurements and on the soft X-ray tomography. The island significantly degrades the energy confinement. The evolution of the island width, derived from magnetic measurements, is well described by the modified Rutherford equation. The onset of the neoclassical mode is observed at low densities with central densities ranging from  $1-3 \cdot 10^{19} \text{m}^{-3}$  and with  $n$  ranging from 0.5 to 1.0. The values of the toroidal beta are low compared to values reported from other experiments, implying that local pressure gradients on the resonant flux surface

must be important for the destabilisation of neoclassical tearing modes in TCV. This has been demonstrated in experiments where modifications of the ECH power deposition profile and hence the pressure profile lead to significant changes of the island width while the global pressure remained constant. The mode can be suppressed by a broadening of the power deposition profile.

### Up-Down asymmetry due to ECCD

Experiments showed an up-down asymmetry, with respect to the ECH heating location, in the soft X-ray emission during sweeps of the ECH beam through the plasma. It was suggested that this asymmetry is caused by a small amount of ECCD that occurs during a nominally-ECH sweep with no toroidal angle, due to the changing geometry between the microwave beam and the total local magnetic field near the resonance.

Further investigations were carried out to identify the source of this asymmetry. Figure 2.1.9 shows that by inverting the toroidal magnetic field direction, the asymmetry reverses as expected based on the change in the field line geometry. Figure 2.1.10 demonstrates the linear relationship between the toroidal injection angle and the sawtooth period when absorption occurs near  $q=1$ : the equivalent local angle at the field line is indicated on the plot. With zero toroidal angle, the local angle at the field line is  $\sim 5^\circ$  leading to co-ECCD with positive  $B$ . One important technical implication is that off-axis current drive is more effective above the midplane than below the midplane for a given toroidal angle, outside launch and positive  $B$  direction.

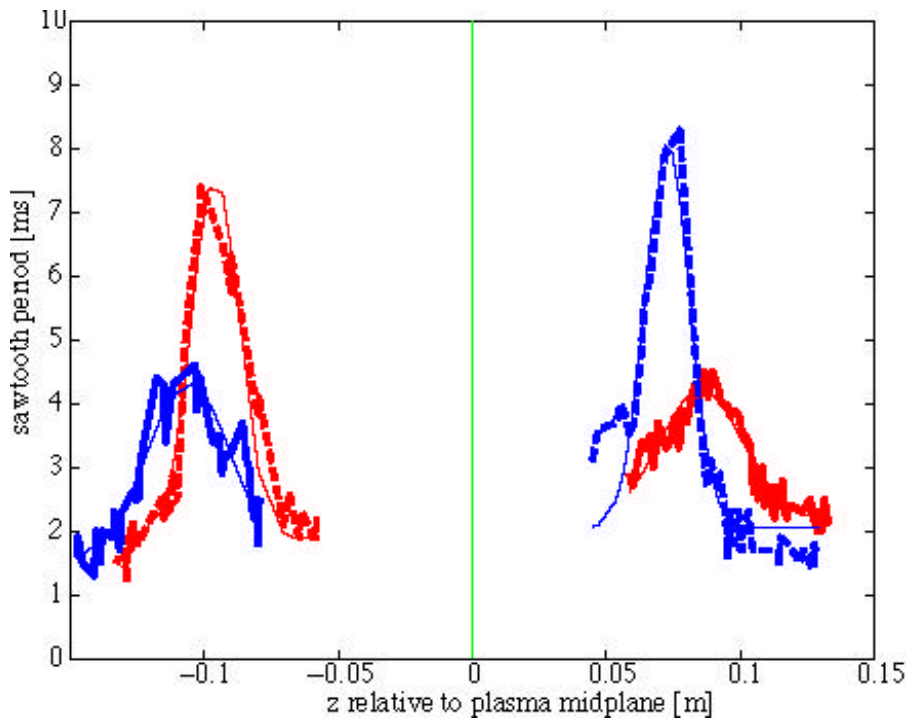


**Fig.2.1.9** When the ECH beam is swept across the  $q=1$  radius, the sawtooth period peaks near the  $q=1$  radius. For  $B_\phi > 0$  (blue curves) the peak near the upper  $q=1$  is highest. For  $B_\phi < 0$  (red curves) the peak near

*the lower  $q=1$  is highest. Under these two conditions (dashes) a small amount of co-ECCD is present. The smaller peaks (thick solid lines) correspond to counter-ECCD. The toroidal injection angle is zero for all 4 sweeps. The sweeps on the left are performed with an equatorial launcher and those on the right with an upper lateral launcher.*

The PRETOR code has been modified to include the effects of current drive and shows a qualitative agreement with the experiments: the sawtooth period is lengthened during co-ECCD relative to counter-ECCD. Further investigations will be carried out to quantify this effect. Calculations to date indicate that the maximum sawtooth period occurs when absorption is near the mixing radius of the sawtooth instability.

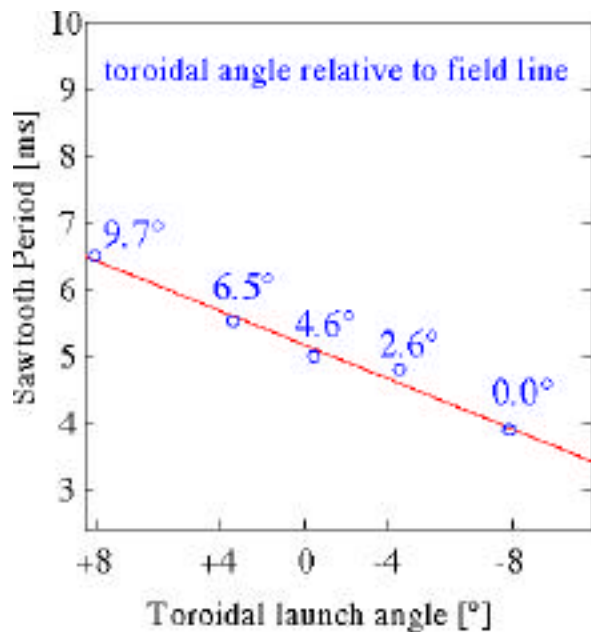


**Fig. 2.1.10** Adding a toroidal angle increases the co-ECCD near the upper part of the  $q=1$  surface, for positive  $B_\phi$ , and the sawtooth period increases (+8° case). Decreasing the toroidal angle eliminates the current drive and the sawtooth period decreases (-8° case).

### 2.1.3 Plasma shaping

#### Vertical Position Control in TCV: Comparison of Model Predictions with Experimental Results

The creation of tokamak plasmas with highly elongated cross-sections is one of the main aims of TCV. Elongated plasmas are inherently unstable with respect to vertical displacement, and they require passive conductors and active feedback coils for stabilisation. The creation of elongated plasmas becomes more difficult as the elongation grows since the growth rate of the vertical displacement instability increases rapidly with elongation. In TCV, elongations up to 2.64 have been achieved, which represents the highest elongation ever produced in a single-axis tokamak with conventional aspect ratio. This result has been made possible through continuous optimisation of the vertical position control system.

The TCV vertical position control system is extremely complex with a large number of adjustable parameters. Experimental optimisation by trial-and-error methods is hopeless. Consequently, theoretical models have been constructed, and the model predictions have been compared with experimental results. Recently, we have developed a Deformable Plasma Model (DPM) and we have shown that its predictions agree well with experimental measurements. Figure 2.1.11 shows a comparison of experimental and theoretical stability limits of the vertical position control system, under closed loop conditions. The stability is analysed as a function of the feedback gains, P (proportional gain) and D (derivative gain). DPM predicts a stable domain for intermediate values of P and D, and unstable solutions everywhere else (dotted areas). Stable experimental conditions are shown as open squares. Experiments with intermittent or saturated, low amplitude oscillations are shown as solid squares. Experiments outside the domain defined by the solid squares produced growing oscillations and disruptions. The experimentally determined stable domain coincides well with the stable domain predicted by DPM. The good agreement between DPM results and experiments will allow us to use this model for further optimisation of the TCV control system or for design studies of new tokamaks.

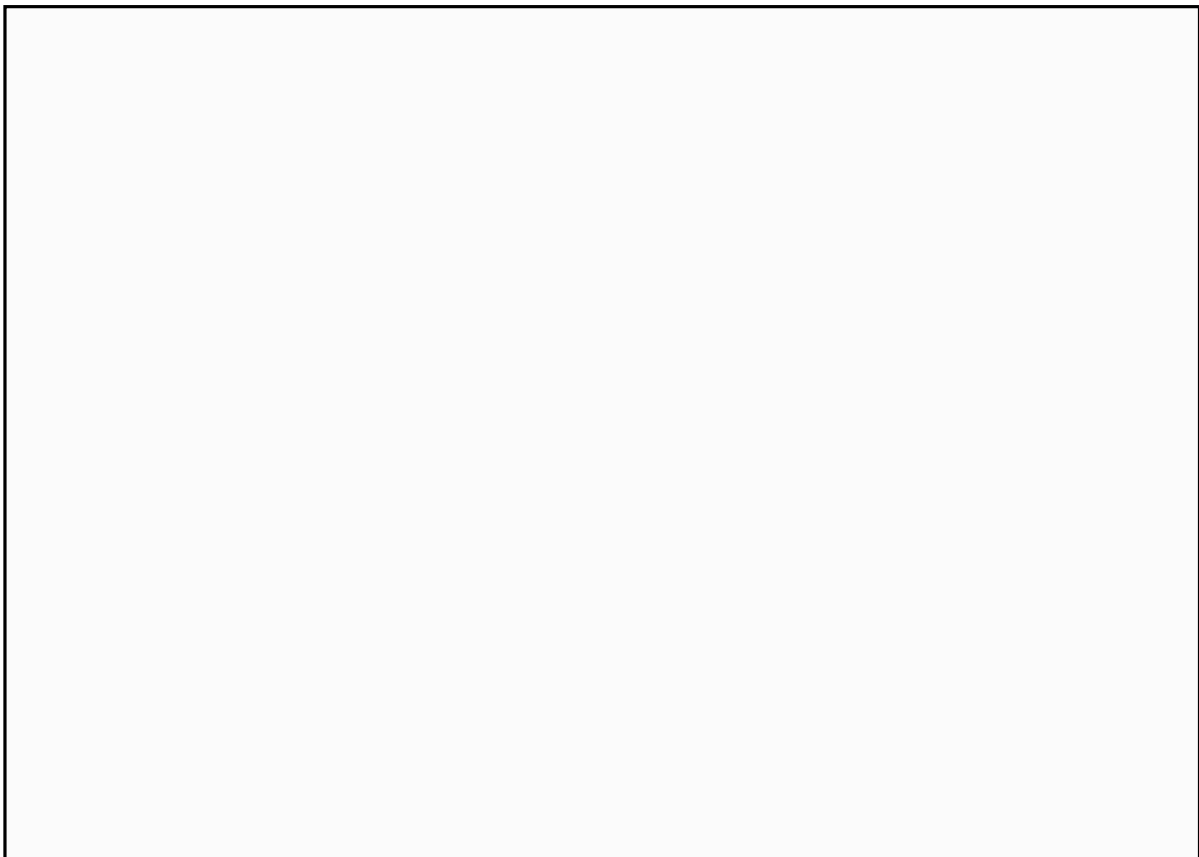


*Fig. 2.1.11 Comparison of closed loop stability predictions with experimental results in TCV.*

### **Plasma response modelling using the DINA code**

Work was started on non-linear simulations of the TCV shape and position feedback control loops using the DINA code, in collaboration with the Kurchatov

Institute and the TRINITY Institute. The geometry of the TCV coils, vessel and diagnostics have been implemented in the code, together with a precise modelling of the feedback electronics. The first simulations were successfully performed at the end of the year showing remarkably good agreement with the experimental data.

### **Divertor detachment in Ohmic plasmas**

Study of the detachment phenomena, whereby particle and energy fluxes arriving at tokamak divertor targets can be drastically reduced whilst maintaining good core confinement, continues to be an important component of the TCV research programme. The flexibility of TCV for plasma shape creation allows equilibria to be developed with long magnetic connection lengths from the midplane to the divertor targets. Such long distances facilitate the development of temperature gradients along the field and promote particle flux amplification at the divertor targets, leading to the high recycling and detached plasma states. Such regimes of operation are those in which future fusion reactors based on the tokamak concept are expected to operate.

Using discharge scenarios in which the central density is ramped progressively through the discharge towards the density limit, the detachment process is being studied with particular emphasis on magnetic equilibria which are only possible in the TCV tokamak. These are extremely open diverted configurations, often characterised by large asymmetries in divertor strike zone geometry. They offer interesting possibilities to study the nature of detachment in geometries in which much of the total midplane-target connection length is found in the poloidal distance from X-point to target and not, as in conventional diverted configurations, where the greatest fraction of this connection length is found in the region from midplane to X-point. One such example is shown in Fig. 2.1.12 where the tomographically inverted D emission from the divertor volume, indicating the deuterium atom density, increases dramatically as detachment proceeds. That the latter is indeed occurring is clearly illustrated by the steady loss of ion particle flux measured close to the divertor strike point as the plasma density increases. These measurements and others are being compared with the results of simulations using the complex plasma boundary codes that are employed for the design of next step tokamaks. Efforts also continue to expand the variety of equilibria under study at TCV and to improve the quality and number of edge diagnostics.

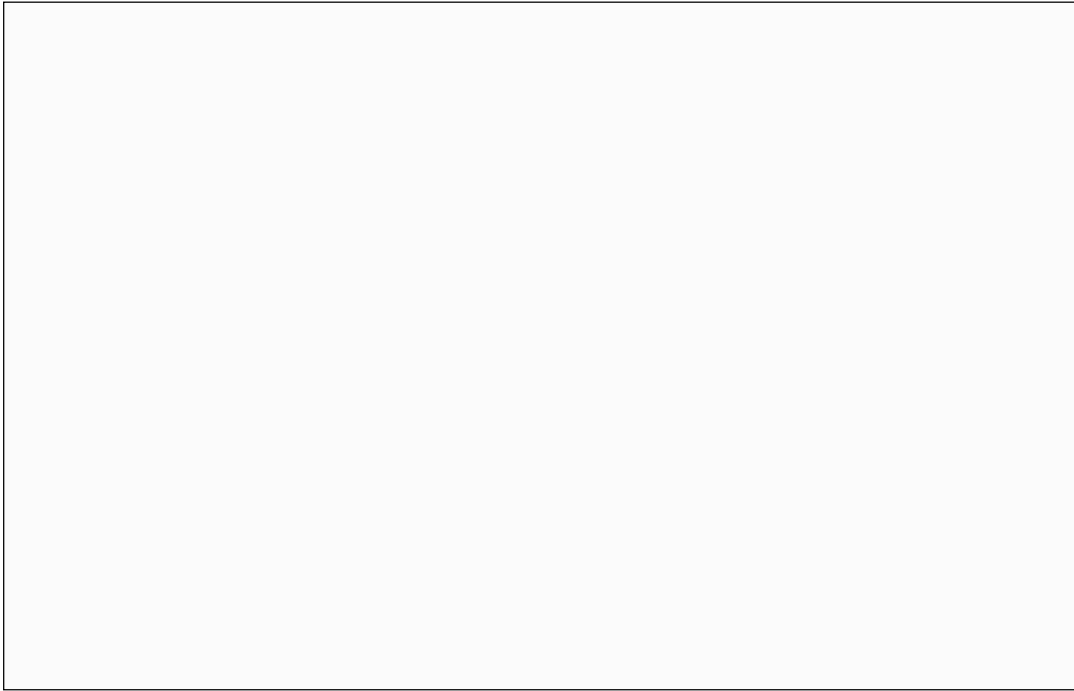


**Fig. 2.1.12** *Illustrating plasma detachment in TCV at the outer target of a single-null lower diverted equilibrium with long X-point to target poloidal distance. The progressive increase in visible light emission from the excitation of neutral deuterium in the cold divertor zone (top pictures) as plasma density rises (bottom left) is accompanied by a complete decrease in ion particle flux (bottom right) arriving at the divertor target near the outer strike zone*

### Locked mode avoidance

Locked mode induced disruptions have occasionally been observed during plasma creation in TCV. A clustering technique was used to locate the region of the TCV operational domain where those modes start growing. The 'dangerous' region is then found to be defined by little overall plasma shaping qualified by  $(\delta^2 + (\kappa-1)^2) < 0.2$ , a narrow range of plasma density,  $2 < n_e [10^{19} \text{m}^{-3}] < 4.5$  and safety factor around 3. Figure 2.1.13 shows the dangerous region on the density: shaping map.

Different test discharges were performed on TCV to verify this statistical result. In the first set of experiments, the plasma was shaped from circular up to an elongation of 1.4 and a triangularity of 0.3 at high safety factor ( $\sim 4-5$ ). Then, the safety factor was lowered down to 2.5. None of those 15 discharges disrupted whatever the density was. In the second set of 13 discharges, the safety factor was decreased prior to the increase of the plasma shape and 6 of them terminated in a disruption. For those 6 evolutions, the density was in the fatal range at the time the plasma was crossing  $q=3$ . For the cases with density outside the fatal range, none of them led to a disruption. These dedicated experiments confirmed the statistical description of the dangerous/non-dangerous domain and clearly indicate the advantage of plasma shaping for operation below  $q=3$ . This result also suggests that traditional wariness of crossing  $q=3$  has been at least partly due to older circular tokamak experience.

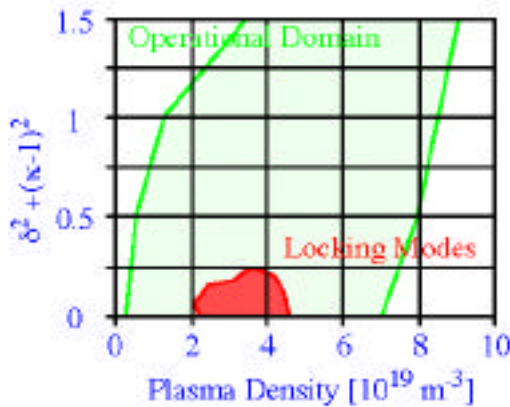


**Fig. 2.1.13** *In the whole operational domain already covered in TCV, the region where locked modes start to grow, leading to the subsequent disruption, is located at little plasma shaping for a limited range of densities. These locked modes start to grow only if these conditions are encountered during the crossing of  $q=3$*

### Evidence for the role of magnetic entropy in stationary tokamak discharges

The profiles of plasma parameters from a large variety of Ohmic plasmas in the TCV tokamak have been compared with a theory based on the assumption that the magnetic entropy is stationary in a tokamak, considered as an open system interacting with the Ohmic transformer. Experimentally, the sawtooth inversion radius and the profiles in the confinement region, depend solely on the parameter  $\langle j \rangle / (q_0 j_0)$  where  $\langle j \rangle$  is the cross sectional averaged current density. The observations agree with the model predictions, which integrate the force balance equation, the effects of sawtoothing and Ohm's law. For each value of  $\langle j \rangle / (q_0 j_0)$  and  $q_0$ , the theory predicts a rigid current profile and a range of possible pressure profiles. The stiffness of the temperature profile, Fig. 2.1.14, which follows from the rigid current profile, implies a correlation between density and pressure profiles, which is observed in the experiment. The range of variation of the electron pressure

profile, Fig. 2.1.15, which is smaller than expected, shows that the theory, as it stands, is still incomplete.

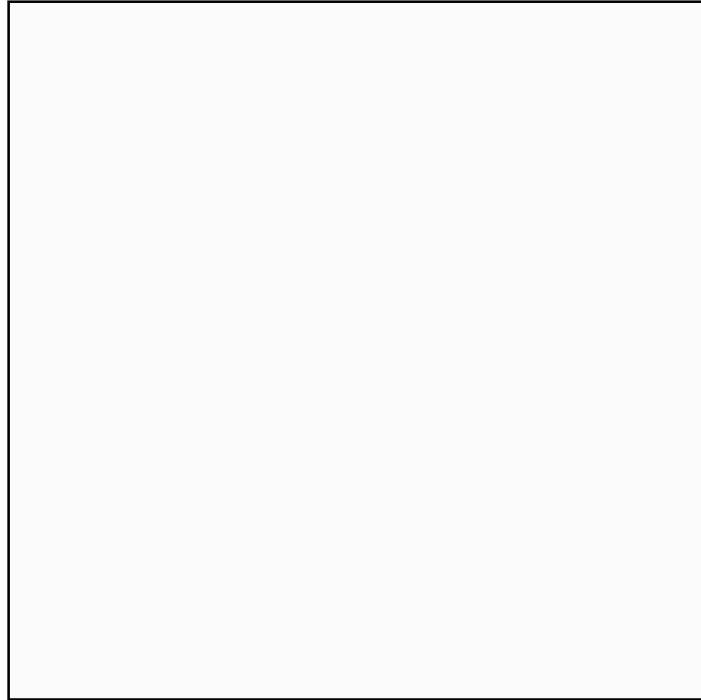


**Fig. 2.1.14** *Scaling (theory and experiment) of the electron temperature profile width  $\langle T_e \rangle / T_e(r_{inv})$*

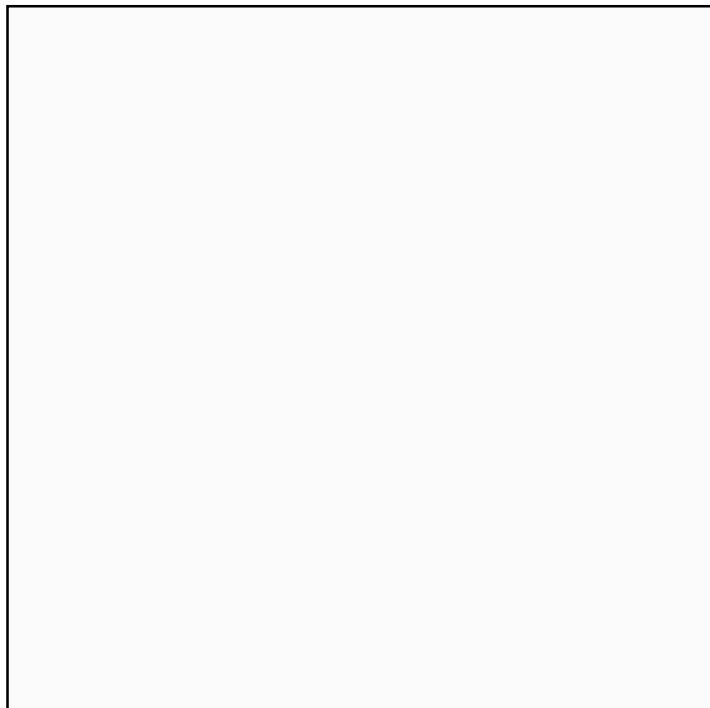


**Fig. 2.1.15** *Scaling of the pressure profile width  $\langle p_e \rangle / p_e(r_{inv})$  and  $\langle p_e \rangle / p_e(0)$ .*

### Triangularity dependence of energy confinement with ECH power

The shape dependence of the energy confinement in ECH plasmas was investigated for power up to 1.5MW,  $P_{ECH}/P_{OH} \sim 2-9$ . Plasma and shape parameters were scanned in a wide range for central power deposition conditions (elongations  $1.1 < \kappa < 2.15$ , triangularities  $-0.65 < \delta < 0.5$ , current  $0.2 < I_p < 0.7 \text{ MA}$  and central density  $1 < n_{e019} < 3.5$ ). In deriving a scaling law for the electron energy confinement time, the dependence on  $\kappa$  and  $I_p$  cannot be separately determined in the present data set. Thus the general power law obtained contains a free parameter  $\alpha_I$ :

$$\tau_{Ee} = 2n_{e_{av}19}^{\alpha_n} P^{\alpha_P} (6I_p)^{\alpha_I} \kappa^{\alpha_\kappa} (1+\delta)^{\alpha_\delta} \left[ ms, m^{-3}, MW, MA \right]$$

with  $\alpha_n = 0.46 \pm 0.2$ ,  $\alpha_P = -0.7 \pm 0.1$ ,  $\alpha_I = -0.35 \pm 0.3$ ,  $\alpha_\kappa = 1.4(1 - \alpha_I) \pm 0.4$ . Good fits are obtained with  $\alpha_I$  in the range 0 to 0.7. Thus the electron energy confinement time increases with a combination of elongation and plasma current.

This scaling displays similarities with the ITER-98L and Rebut-Lallia-Watkins (RLW) scaling law, in particular for the power and density dependence. The ITER-98L scaling law, however, does not account for the beneficial effect of negative triangularities, an effect much better accounted for in the critical temperature gradient RLW model scaling. The beneficial effect of negative triangularities, previously observed in Ohmic discharges, continues to be seen at the present power levels. The benefit of low or slightly negative triangularity on confinement is however most effective at low total power and decreases without totally disappearing at the highest powers used so far, as shown in Fig. 2.1.16. High power experiments at up to 3MW should help to clarify the trend so far observed up to 1.5MW.

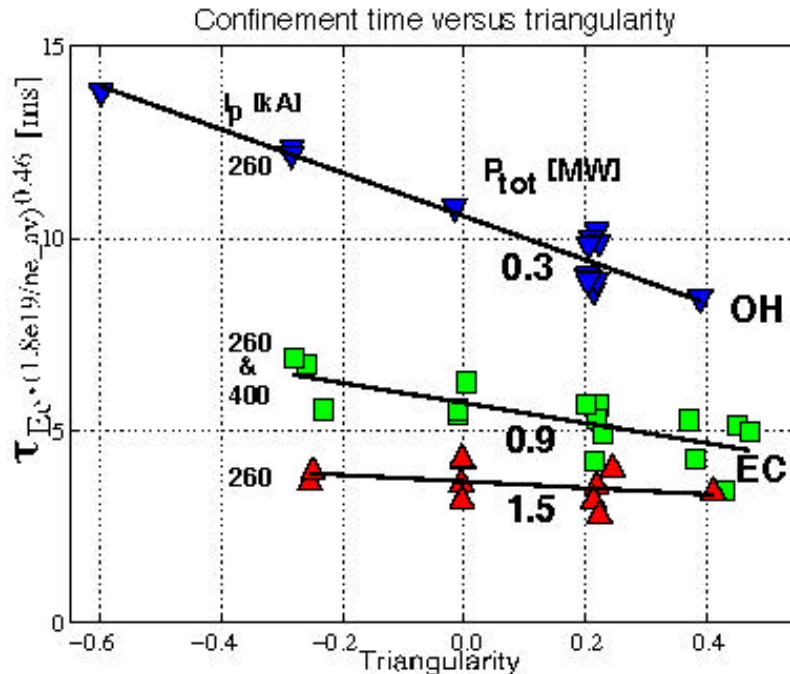


**Fig. 2.1.16** *Triangularity dependence of the energy confinement time for three total power ranges of centrally EC deposited power ( $\kappa=1.5$ , density range:  $1.3 < n_{e019} < 3$ , confinement time normalised to  $n_{e_{av}} = 2 \cdot 10^{19} m^{-3}$ ).*

*The power range for the low power "0.3MW" class is the largest ( $\pm 16\%$ ); the higher confinement at negative triangularity reflects therefore predominantly an effect of plasma shape.*

## **2.2 Theory and numerical simulation**

### **2.2.1 Macroscopic stability of tokamaks**

The main purpose of this work is to determine the operational limits of tokamaks imposed by fast-growing, macroscopic, fluid types of instabilities.

#### **Configurations with a magnetic separatrix**

The MHD equilibrium and stability codes developed specifically for configurations with a magnetic separatrix have been further upgraded. An analytic fast poloidal phase extraction has been implemented, allowing the study of global modes up to arbitrarily large toroidal mode numbers. The bootstrap current calculation has been introduced in a new, free-boundary version of the equilibrium code CAXE, with a possibility to prescribe only the driven part of the plasma current. The specification of a given safety factor profile is also possible. A new version of the KINX stability code is being developed to compute the kink mode stability in the presence of plasma rotation and a resistive vacuum vessel. Also, a workstation version of KINX with optimised memory requirement is under development.

The application of the above codes has focused this year on low aspect ratio configurations. The goals were motivated by power plant optimisation requirements: high beta, high normalised beta  $\beta_N = \beta / (I/aB)$  and high bootstrap current fraction. Such high beta values implicitly require operation in the second-stability region for ballooning modes and wall stabilisation of external kink modes. The other requirement was to make these computations on free-boundary equilibria and to study the influence of the plasma shape.

We could obtain second ballooning mode stable, free-boundary equilibria with a nearly 100% bootstrap current fraction. A moderate positive outboard squareness of the plasma shape was found to be sufficient to reach  $\beta_N > 8$ . Both triangularity and separatrix proximity were found to be favourable for external kink mode stability. For an equilibrium with a boundary at 99% of the separatrix flux and a triangularity  $\delta = 0.6$ ,  $\delta = 63\%$ ,  $\beta_N = 8.3$ , the marginal conformal wall positions are  $a_w/a = 1.75, 1.5, 1.4$  for toroidal mode numbers  $n = 1, 2, 3$  respectively.

#### **Other codes**

A number of MHD codes has been installed at CRPP: the non-linear resistive code XTOR - in collaboration with H. Lutjens (Ecole Polytechnique, France), the linear non-ideal code PEST3, the new version of the ideal KINX code - in collaboration with S. Medvedev (Keldysh Institute, Moscow, Russia). The codes were tested and are used now for analysis of MHD stability of TCV discharges and for studies of the dependence of MHD stability of tokamak plasmas on plasma shape. Several TCV shots with different shapes have been analysed by XTOR and KINX codes and the

strong dependence of ideal kink growth rate on shaping parameters was found. The preliminary calculations of the suppression of internal kink mode by diamagnetic rotation were performed using the XTOR code.

### **2.2.2 Optimisation of 3-D magnetic confinement configurations**

The design of 3D magnetic confinement configurations is a much more difficult task than for tokamaks. The three-dimensionality, while adding degrees of freedom, requires special care in order that the configuration actually confines. One way to overcome the difficulty is to try to obtain "quasi-symmetry" (QS), a 3D magnetic configuration in which the modulus of B only depends on two independent variables: a radial variable (magnetic surface index) and a combination of poloidal and toroidal co-ordinates. The confinement of particles in such devices becomes comparable to that of an axisymmetric tokamak.

Unfortunately, the quasi-symmetry condition is difficult to obtain in practice and the concept of "pseudo-symmetry" (PS) has been developed. Locally trapped particles are absent in such systems and the mod-B lines on magnetic flux surfaces do not form closed contours. The mod-B depends only on the radial variable and a combination of the angular variables in a more general set of straight field line co-ordinates than the Boozer frame that characterises QS devices. Furthermore, unlike QS criteria, PS conditions can be satisfied throughout the plasma volume. Pseudo-symmetry is less restrictive than quasi-symmetry which must satisfy the additional constraints that the bounce averaged particle trajectories lie on the flux surfaces and that the banana orbit width remains invariant in the direction of QS (i.e., in the direction in which the combination of angular variables is constant). In order to build a configuration optimiser, a target function called WATER has been developed that measures the area of local ripples in the magnetic field strength along a field line. The minimisation of this area makes a 3D configuration approach pseudo-symmetric conditions. Also, the expression of PS condition in the near-axis approximation was obtained so that it can be implemented in the numerical optimiser package.

We have also explored a class of magnetic confinement systems consisting of "hybrid" tokamaks/stellarators in which the rotational transform is produced in part by a net toroidal plasma current and in part by external coils.

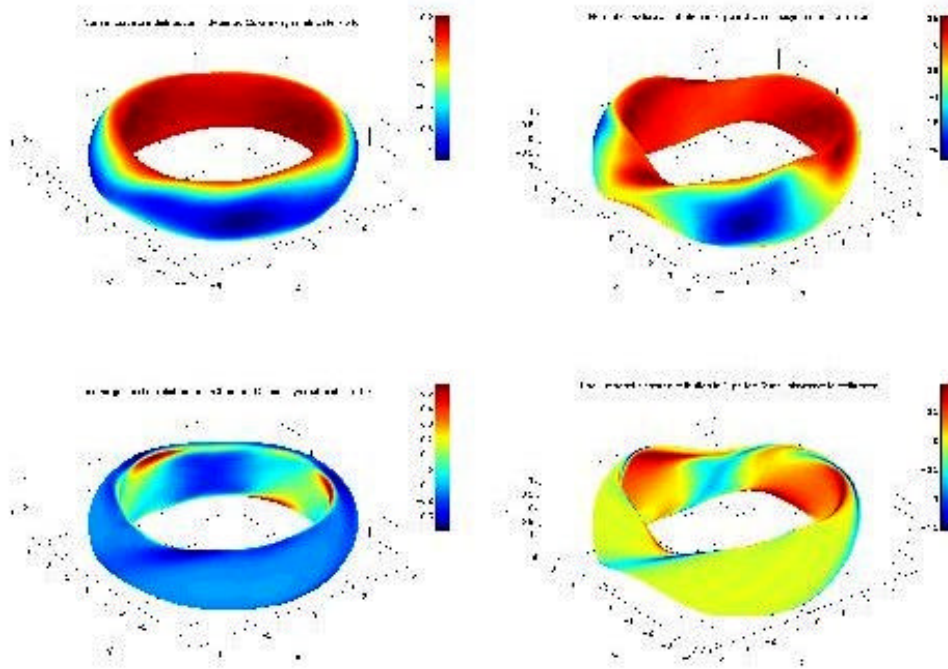


**Fig.2.2.1** *The normal magnetic curvature (top) and the local magnetic shear (bottom) distributions on a toroidal magnetic flux surface near mid-volume at  $\beta=5.3\%$  for a nearly axisymmetric configuration (left) and a 3D system with quasisymmetry features (right).*

### **3-D magnetic confinement configurations**

#### ***A three-field period system with quasi-axisymmetric features***

The ideal MHD stability properties of a three-field period stellarator system with quasi-axisymmetric features has been investigated. A pressure profile that is near marginal stability to localised ideal ballooning modes has been determined and yields a limiting  $\beta = 5.3\%$  value. Half of the edge rotational transform is produced with a hollow bootstrap-like current profile and the other half results from 3D plasma shaping effects. A sequence of configurations has been developed in which the non-axisymmetric components of the plasma boundary shape are reduced in magnitude to recover the equivalent axisymmetric tokamak. The magnitudes of the toroidal plasma current and the pressure on axis are adjusted to maintain the maximum rotational transform in the plasma fixed at 0.484 and the  $\beta$  fixed at 5.3%. The global external kink modes are stabilised by the 3D deformation of the plasma while the ballooning stability properties are deteriorated.

#### ***Spherical Tokamak/Sphellamak hybrid configuration***

The global and local ideal MHD stability properties of a hybrid Spherical Tokamak and Sphellamak device have been examined. The system consists of 10 toroidal field (TF) coils and 10 Furth-Hartman type coils that produce a helical field. The TF coil current is 160kA and the helical coil current varies from zero to 180kA. Bootstrap-like hollow toroidal plasma currents produce the bulk of the rotational

transform. As the helical coil current is increased, the toroidal plasma current is reduced from 265kA to 250kA to maintain the safety factor  $q \sim 2.2$  at the edge. A transition from axisymmetric to quasi-axisymmetric conditions in a compact system has been demonstrated when the current in the helical coils becomes comparable to that of the TF coils at  $\sim 14.4\%$ . To achieve ballooning stability, the pressure profile must be increasingly flattened around the vanishing global shear region near the edge of the plasma as the current in the helical coils and consequently the plasma shape distortion become larger. In all the cases examined, a closely fitting near conformal conducting wall is required to guarantee stability with respect to low order global external kinks. However, the proximity of the conducting wall can be relaxed as the 3D plasma shaping becomes more pronounced.

The improvement in the global external ideal MHD properties and the deterioration of the ballooning properties can be understood in the two systems in terms of the behaviour of the normal magnetic field line curvature and the local magnetic shear. On average, the magnetic field line curvature does not change significantly with the plasma boundary shaping, but it does become enhanced locally. The local magnetic shear, on the other hand, acquires a helical stripe of appreciable magnitude within each field period that inhibits the formation of global mode structures that align with the pitch of the magnetic field lines. However, in the region between the helical stripe patterns, the local magnetic shear tends to vanish which coincides with the domain of increased normal magnetic field line curvature. Consequently, ballooning type mode structures that concentrate in this enhanced curvature-vanishing local shear region can be more effectively destabilised.

As a first step towards the investigation of particle confinement properties of fully 3D systems, we have studied the effect of a perturbation of a tokamak equilibrium by helical external coils, thus modelling the Dynamic Ergodic Divertor (DED) in the TEXTOR tokamak. The behaviour of magnetic field lines and of particle drift orbits have been investigated in a reversed shear configuration. We have observed that a robust magnetic field line barrier with respect to the perturbation occurs near the maximum of the safety factor profile of the underlying unperturbed equilibrium state. This is a consequence of the non-applicability of the Kolmogorov-Arnold-Moser (KAM) theorem for non-monotonic profiles. A clear effect is seen on the lost particles at the plasma edge: the DED is much less effective in extracting the passing particles for the reversed shear case compared with a monotonic shear case.

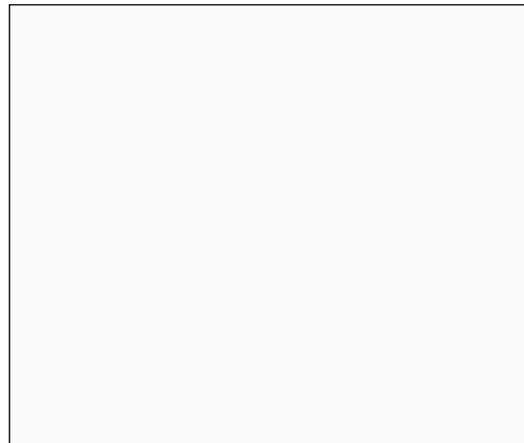
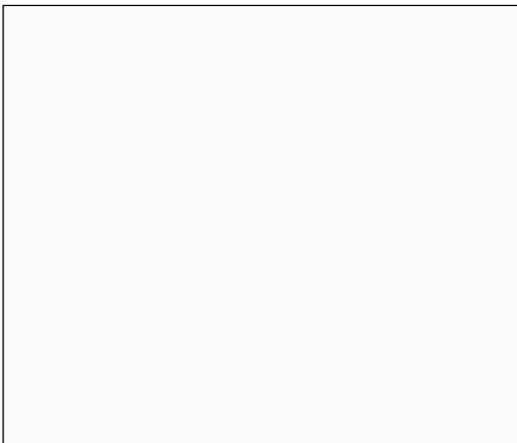


**Fig. 2.2.2** *Contour plots of particle positions lost at the edge of the TEXTOR-94 tokamak, for a monotonic  $q$  profile (left) and a reversed shear profile (right), shown versus toroidal (horizontal axis) and poloidal (vertical axis) angles.*

Concerning the particle drift orbits, we have defined the notion of a radius of confinement within which all particles that are launched are almost perfectly confined. The confinement radius decreases with increasing particle energy but saturates at the radius of maximum safety factor value. Thus the particles feel the effect of the magnetic field line barrier. We interpret this phenomenon as a "transport" barrier for particles. The magnetic field line diffusion coefficient is reduced by a factor of 10 and the fraction of particles lost is 4 times smaller than in a standard monotonic shear case. Trapped particles are unaffected by the high field side DED coils and are lost in the ripples of the magnetic field.

### **2.2.3 Microinstabilities in tokamaks**

Our present understanding of anomalous transport in magnetically confined plasmas is based on various underlying microinstabilities driven by equilibrium gradients. While local models using the ballooning transform or the flux-tube representation have already been developed elsewhere, the global approach in which the relevant gyrokinetic equations are solved in the whole plasma domain in the appropriate geometry is a step forward. One important question is to determine how far local models can provide a reliable theoretical prediction. In this context, results from the ballooning eigenvalue code, which solves the gyrokinetic electrostatic equation for the case of full ion dynamics, have been compared with global gyrokinetic code results. The GLOGYSTO global spectral code has been run for two scenarios with different toroidal wave numbers and Larmor radii, but being isodynamical in the frame of the lowest order ballooning approximation. A discrepancy between mode growth rates has been found: with the ballooning representation they are overestimated by a factor 1.7 with respect to the higher toroidal wave number case and by a factor 3-4 to the lower one. We note that the ballooning results are not better than those from a local dispersion relation. The conclusion is that a global approach is mandatory in order to get a quantitatively correct prediction.

Several advances have been made in the refinement of the models used in our global codes. In the context of a time evolution Particle-In-Cell (PIC) approach for solving gyrokinetic equations, a modified quasi-neutrality equation has been developed. In the previous version of the code, the finite Larmor radius (FLR) effects appeared through a second order correction term in FLR in the quasi-neutrality equation. In order to study microinstabilities in realistic fusion device geometry, this limit has been relaxed using a more sophisticated correction term. The algorithm has already been implemented in the case of adiabatic electrons with electrostatic perturbations. Several versions of the code have been written and they are currently under test. The next step of this work will be the development of a similar algorithm for codes solving the same problem in the case of kinetic electrons and electromagnetic perturbations.

There is mounting experimental and theoretical evidence that the presence of radial electric fields, generating ExB flows, is an essential ingredient in the appearance of "transport barriers", which are characterised by both reduced transport and

reduced micro-turbulence levels. Our contribution to this understanding has been the inclusion of ExB flows in both our spectral and time evolution PIC global codes. In the linear approach, a prescribed equilibrium radial electric field is given. First results show a strong stabilising effect on the toroidal ITG mode. One of the most remarkable findings is that a completely shearless ExB flow seems at least as effective in stabilising the mode as a sheared ExB flow, Fig.2.2.3. More analysis is needed to interpret these results fully. The immediate future will see a benchmarking comparison of spectral and PIC codes before analysis of some experimental cases.

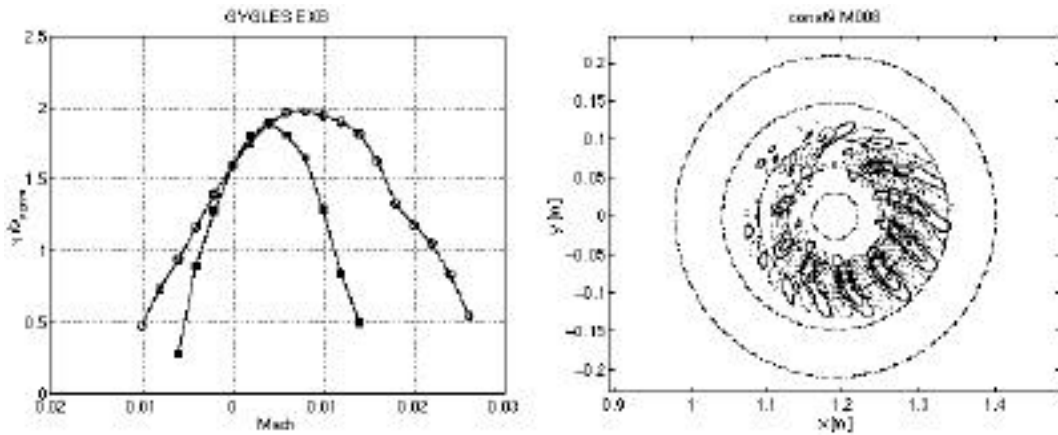


**Fig.2.2.3** *Left: Growth rate of the most unstable toroidal ITG mode versus Mach number for shearless ExB flow (filled symbols) and sheared ExB flows (open symbols). Right: Contour plot of equipotentials for a shearless ExB flow with Mach=-0.08.*

Electron dynamics and electromagnetic effects also play an important role, already with beta values typical of present-day fusion experiments. While the electrostatic ITG mode is stabilised by increasing beta, another mode is destabilised: originally baptised the "kinetic ballooning mode", it is of electromagnetic nature and passing electrons play an important role in driving it unstable.

As a first step, a new code has been developed which solves the general electromagnetic kinetic dispersion relation for microinstabilities. This local code can solve the full electron dynamics and includes the effects of trapped electrons, trapped ions and of the Shafranov shift. In a second step, the GLOGYSTO global spectral code was modified to include finite beta effects. The approximation of quasi-adiabatic electrons is used and so far only passing particles are taken into account. First results show a similar stabilising influence of finite beta on the toroidal ITG mode, in qualitative agreement with the local dispersion relation. More numerical work is needed to find electromagnetic modes, in particular the inclusion of the drive of passing electrons, which was so far neglected.

In a parallel development, we are developing the time evolution, finite element, PIC approach with the aim of treating the electron dynamics and electromagnetic effects. The difficulty, compared with the previous purely electrostatic and adiabatic electron response, is twofold. Firstly, the electron transit time must be resolved. Secondly, the presence of Alfvénic or quasi-electrostatic high frequency modes, which are physically stable but unfortunately destabilised by the explicit time integration scheme adopted so far, must be handled. Therefore, as a first step,

a time-implicit scheme has been introduced into the electrostatic linear gyrokinetic code in order to treat the drift-kinetic electrons, instead of using the simple Boltzmann distribution for all the electrons. Benchmarking of the code has already been accomplished. The results show that: (1) there is a limitation of the timestep to values smaller by a factor of 10 at least than the passing electron transit time, although the same implicit method is "unconditionally stable" in a simple uniform unmagnetized plasma and (2) the complex frequencies practically do not depend on the mass ratio  $m_i/m_e$  for values above about 200. The electromagnetic effects should be included next.

#### **2.2.4 *Microinstabilities in stellarators***

Drift waves are commonly held responsible for anomalous transport in tokamak configurations and in particular for the anomalously high heat loss. On the other hand, the next generation of stellarators should be characterised by the much smaller neo-classical transport and by particle confinement close to that of tokamaks. There is nevertheless a strong interest in the stellarator community to study the properties of drift waves in 3D magnetic configurations. To satisfy this interest we have developed the first global gyrokinetic code aimed at the investigation of linear drift wave stability in general toroidal geometry. As a first application, two configurations have been studied, the Quasi-Axisymmetric Stellarator with three fields periods (QAS3) currently developed at the Princeton Plasma Physics Laboratory and the Helically Symmetric eXperiment (HSX) which started operation at the University of Wisconsin last summer. The QAS3 is characterised by a tokamak-like field in the outer part of the torus. In this structure the drift waves are mainly affected by the skewness of the field lines (the magnetic shear) and hardly at all by the shape of the plasma. The results are very close to those obtained for a tokamak. On the other hand, results for the HSX configuration, which is characterised by a dominantly helical magnetic field, show a clear 3D effect, namely a strong toroidal variation of the drift wave mode structure. This variation is a clear function of the 3D plasma shape, Fig. 2.2.4.

#### **2.2.5 *Neo-classical theory***

We have developed the standard kinetic approach of neo-classical theory to obtain a set of relatively simple kinetic equations suitable for implementation in a numerical code to compute all neo-classical transport coefficients within the same general formulation, in particular those related to perpendicular transport. These equations have been implemented in the Fokker-Planck code CQL3D, which uses the full collision operator and a realistic axisymmetric configuration of the flux surfaces. All the coefficients have been computed in the banana regime for a wide variety of equilibrium parameters. The kinetic approach, the numerical results and a set of fitting formulas which allow to easily compute all the neo-classical transport coefficients at all aspect ratios, in general axisymmetric equilibria, have been collected together in a single paper for convenience.

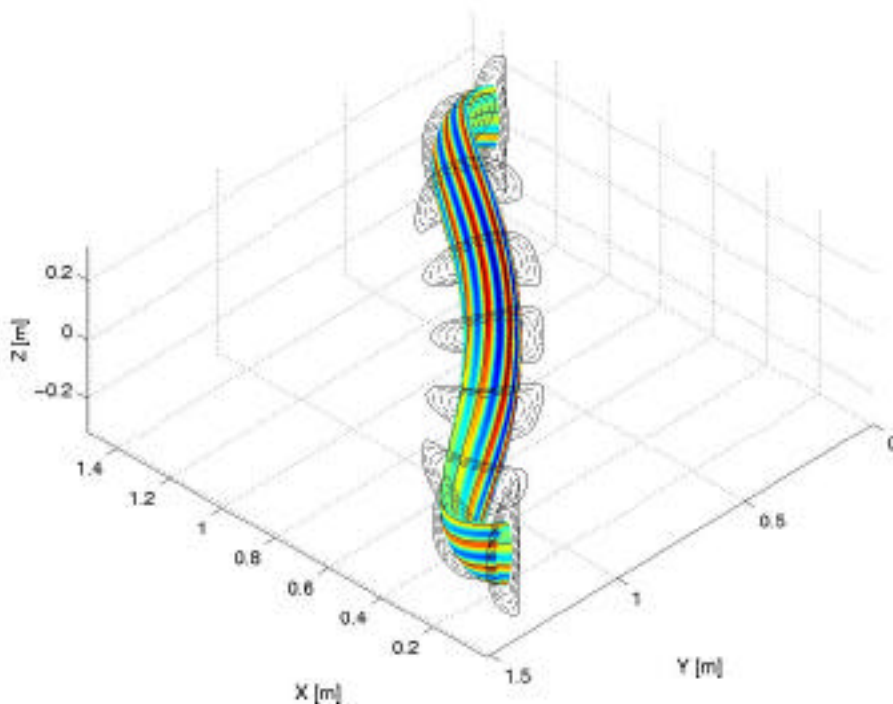


**Fig. 2.2.4** *Contour plot of an ITG mode in the quasi-helically symmetric stellarator HSX computed with the global gyrokinetic code EUTERPE. Only one of the four field-periods of the device is shown.*

### **2.2.6 1D fluid transport**

The PRETOR 1D transport code is used to simulate TCV discharges with very different plasma boundary shapes, in order to validate the most commonly used transport models over a wide range of plasma parameters.

The MMM95 (Multi Mode Model 1995) and IFS/PPPL (Institute for Fusion Studies/Princeton Plasma Physics Laboratory) are two almost completely theoretical transport models and have been implemented in PRETOR. First applications of these two transport models in the simulation of the electron temperature profile of TCV Ohmic discharges have given satisfactory results. However, a model validation analysis over a large domain of plasma parameters needs a reliable ion temperature diagnostic, which will be available on TCV in the near future.

Simulations of ECH and ECCD discharges with the RLW (Rebut-Lallia-Watkins) empirical transport model are in very good agreement with the experimental data. In particular, in PRETOR calculations, sawtooth stabilisation has been identified as responsible for the central electron temperature enhancement during counter EC current drive experiments.

### **2.2.7 RF wave heating and destabilisation by fast particles**

We have started the development of a novel RF global wave code applicable to 3D systems. Plasma heating by electromagnetic waves in the Alfvén and Ion Cyclotron range of frequencies in 3D configurations is studied using the wave propagation equation in potential formulation written in Boozer magnetic co-ordinates. This equation has to be solved numerically with finite elements for discretisation in the radial variable and Fourier decomposition in the poloidal and toroidal co-ordinates.

Analysis of JET discharges in which Alfvén Eigenmodes (AE) of intermediate toroidal mode numbers ( $n=5-10$ ) were observed by the passive detection system, implying they were unstable, have been performed using both the fully kinetic PENN model and the hybrid fluid-kinetic LION model. The emphasis has been on finite beta effects in hot-ion mode discharges heated by NBI and minority ICRH. The modes are observed at frequencies consistently 10%-20% below the centre of the gap. Both LION and PENN predictions agree with the experimental results for the eigenfrequency and also for the stabilising role of finite beta, the underlying physical mechanism of which is, however, quite different.

In the LION computations, the modes correspond to core-localised Toroidicity Alfvén Eigenmodes (TAE). Their eigenfrequencies are close to the lower gap edge and gets closer and closer as beta increases. The eigenmodes get more and more radially peaked, which results in an increase in the parallel electric field and therefore in electron Landau damping. These LION results are in agreement with the observations that, as beta rises, the highest  $n$  TAEs disappear first, because the damping is proportional to  $n^2$  while the drive, proportional to  $n$ , does not vary much with  $n$ .

While the kinetic results also predict a stabilisation of TAEs with increasing plasma beta, detailed analysis reveals a completely different mechanism. Contrary to the fluid prediction of a core-localised TAE becoming increasingly peaked with beta, there is substantial mode conversion to the kinetic Alfvén wave which extends far from the plasma core region. This extension actually increases with beta and when the kinetic wave reaches the high shear region near the separatrix it is heavily damped.

We have also started an investigation of strongly reversed shear configurations characterised by a high  $q$  value at the centre. This makes the AE eigenfrequencies drop to values in the drift frequency range. Preliminary computations with the PENN code indicate that AEs are then much more unstable than in standard scenarios.

## **2.3 Materials for fusion**

The main objective of the materials group is to study the effects of radiation on materials and their implications for the degradation of their mechanical properties. Initially, the fundamental aspects of irradiation damage are investigated with experiments on pure materials and model alloys as well as with computational models. In the frame of the study of irradiation damage production and accumulation, results on irradiated pure fcc and bcc metals and on model alloys, computer simulations of irradiation induced defects and of transmission electron microscopy images are presented in Section 2.3.1. Investigations on technical alloys have been undertaken on low activation steels (OPTIMAX series and F82H) in

non-irradiated and irradiated conditions. The results obtained on these low activation steels are presented in Sections 2.3.2 and 2.3.3. Titanium alloys are also candidate low activation materials and in Section 2.3.4 it is shown that the  $\beta$ -phase alloys are relevant candidates. Since Irradiation Assisted Stress Corrosion Cracking (IASCC) of steels is an important problem for structures operating in an irradiating environment, IASCC has also been studied for stainless steels and the results are presented in Section 2.3.5.

### 2.3.1 The early stages of damage

#### Defect microstructure and tensile properties of pure fcc and bcc metals and model alloys after low dose irradiation

The effects of the crystal structure on the defect microstructure produced by high energy recoils in pure metals and model alloys, their dose dependence and resulting mechanical properties have been studied. The metals and alloys considered here are: pure Cu, Pd, Au, Fe, Mo and the model alloy Fe-12Cr with and without C. The irradiation matrix included doses from  $10^{-5}$  to  $10^{-1}$ dpa at temperatures between  $0.2-0.3T_M$  (where  $T_M$  is the melting point of the material), that is, below the stage at which vacancies start to evaporate from defect clusters. These low doses allow the study of the behaviour of the material in the condition in which independent cascades are produced to the level where saturation is achieved, that is, as cascades begin to overlap. The main results obtained are:

- While the observed defect distributions have comparable mean sizes (1.5-3nm) in all the materials irradiated in this range of doses, in Cu, 90% of the defects observed are stacking fault tetrahedra (SFT's). In contrast, in Pd, both SFT's and small loops are observed at doses  $10^{-2}$ dpa. For doses  $> 10^{-2}$ dpa only loops are found. In Fe, as well as in both austenitic (304 and 316) and ferritic-martensitic (F82H) steels, irradiated with 590MeV protons, the defect microstructure consists also of loops with mean sizes in the range 2.3-3.2nm. The most recent set of results is shown in Fig. 2.3.1, which includes alloys of technological interest and indicates that their behaviour is comparable.

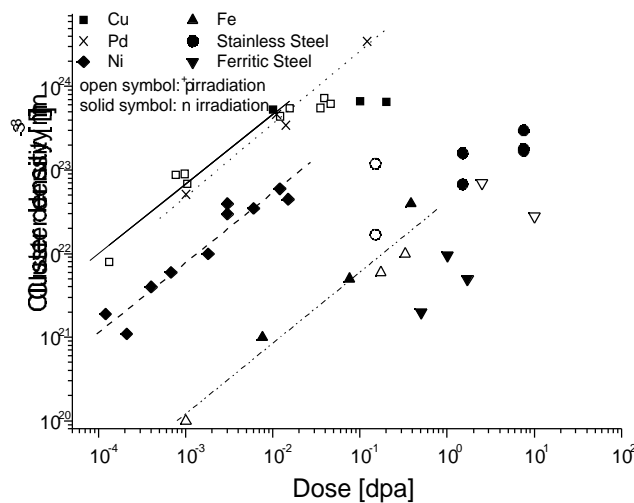


**Fig. 2.3.1 Defect cluster accumulation in pure metals and technical alloys**

- The accumulation of SFT's in Cu reaches saturation at a dose of  $10^{-2}$ dpa with a density of  $7 \times 10^{23} \text{m}^{-3}$ . No saturation has been observed as yet for the loop accumulation in Pd or, at higher doses, in Fe. In the case of Pd, the highest value measured for the loop density is  $4 \cdot 10^{24} \text{m}^{-3}$ .
- The mean defect cluster size remains constant with increasing dose in the defined range of doses and irradiation temperatures. This is true for SFT's in Cu even beyond saturation. In the case of loops, their mean size has been shown to increase at doses higher than 1dpa in austenitic stainless steels or at higher temperatures in pure Fe.
- In terms of defect accumulation, fcc Cu and Pd show similar behaviour, with an almost linear dependence of the number density on the dose expressed in dpa. Although the type of dependence is comparable, in the case of bcc Fe a remarkable difference is found in the accumulation rate: three orders of magnitude higher doses are needed in Fe to reach the same number density of clusters as in Cu.
- The tensile behaviour of Cu and Pd is similar. Substantial radiation hardening occurs in both metals: at saturation, the yield stress in Cu has increased by a factor of 100. As the dose is increased, a broad yield point develops, followed by a yield region with strong serrations while the mean stress remains approximately constant up to shear strains of about 0.15-0.2, at which point work hardening starts. Work hardening is lowered in the irradiated metal to the extent that it disappears in Fe irradiated beyond 0.1dpa.
- A strong strain localisation takes place during deformation. Dislocation channeling is the dominant deformation mode. Deformation twinning is also observed in stainless steels. The channel has a peculiar scaling, present in all the materials examined: the width of the channel is limited to 100nm while the distance between channels remains at about 1 micron.
- Intergranular cracking has been systematically found in irradiated iron, austenitic stainless steels and ferritic-martensitic steels at doses of  $10^{-3}$ dpa or higher. It is believed the intrinsic mechanism for the loss of ductility in irradiated materials is strain localisation by dislocation channeling or twinning deformation modes.

The case of Fe and the Fe-12Cr model alloys is of particular relevance in the understanding of the behaviour of the irradiated ferritic/martensitic steels. The Fe-12Cr alloy was irradiated at room temperature and 250°C up to a dose of 0.2dpa. TEM observations show that the defect microstructure produced by 590MeV protons in the Fe-12Cr alloy consists of small defect clusters, probably interstitial in character. The structure is comparable to that previously observed in irradiated Fe. At room temperature, the average defect size is around 3.3nm. Somewhat higher mean sizes (~4.8nm) are found after irradiation at 250°C. The cluster density of pure irradiated Fe at room temperature and at 523°K increases with the dose, but at a slightly different rate. In Fe, it is well established that the deformation mode at room temperature is dislocation channeling. Such a deformation mode has now also been observed after deformation of the irradiated

12Cr alloy. The channel width is typically 60-100nm and it develops on {110} type slip planes, see Fig. 2.3.2.

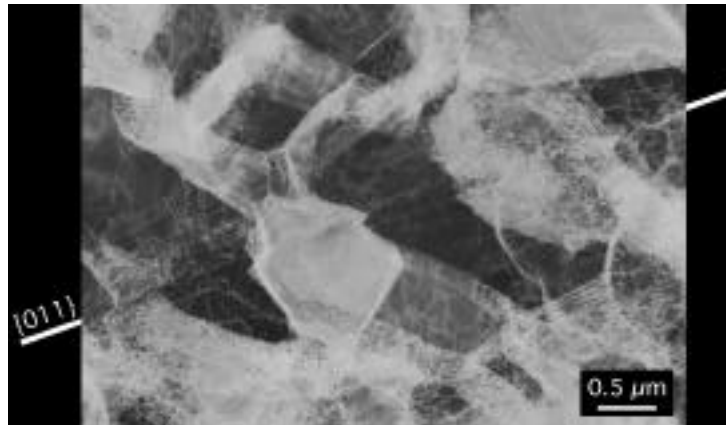


**Fig. 2.3.2** Channel in the deformed Fe-12Cr irradiated to 0.2dpa at 250°C

### **Defects and radiation induced phase transformations in intermetallics**

Intermetallic thin films of Ni<sub>3</sub>Al and NiAl of stoichiometric composition have been produced by magnetron sputtering onto (100) Si and (110)Ni substrates. The thin films have nanograin sizes ranging from 50 to 100nm and exhibit fiber textures in the <110> and <111> directions when deposited onto Si. The films have been fully characterised by TEM, secondary ion mass spectroscopy and scanning tunnelling microscopy. A fully ordered lattice is obtained in both intermetallics. A single crystalline heteroepitaxial growth relation of (110)[110]<sub>L12</sub> || (110)[110]<sub>fcc</sub> is obtained in Ni<sub>3</sub>Al, while a granular-heteroepitaxial growth mode exhibiting the inverse Nishima-Wassermann relation (211)[211]<sub>B2</sub> || (110)[110]<sub>fcc</sub> is observed in NiAl for the first time.

Both thin films and single crystals of NiAl and Ni<sub>3</sub>Al have been irradiated with Ni ions with energies up to 6MeV and fluences of 10<sup>15</sup>ions.cm<sup>-2</sup>. TEM observations show the presence of defect clusters in densities of up to 10<sup>22</sup>m<sup>-3</sup> but no evidence of amorphization by the displacement cascades, contrary to what was predicted by previous modelling.

The image simulation method described here below was tentatively applied to the study of the defect clusters induced by displacement cascades in NiAl and Ni<sub>3</sub>Al. Disordered zones were evidenced in both materials, while amorphous material was found in NiAl after two cascades were shot in the sample. It was shown that high resolution imaging mode may be used to visualise radiation damage when the defocus values far from Scherzer were chosen.

### **Computer simulation of irradiation induced defects**

Previous results in Al have been extended by calculations of the formation and binding energies of voids, hexagonal, circular and triangular loops and SFT's containing up to 631 point defects. For clusters of less than 300 vacancies, SFT's have the lowest formation energy, while voids are favoured at larger sizes. The SFT

formation though, is restricted by their development from Frank type loops, which have higher energies than voids and become then the predominant defect cluster. Comparisons between MD (molecular dynamics) atomistic calculations and those performed using classical elastic dislocation theory, suggests that continuum theory is applicable down to subnanometer sizes in the case of interstitial loops while it is approximately a factor of ten higher for vacancy Frank type loops.

As previously indicated, experimental observations indicate that in Cu, the main stable defect formed during irradiation is stacking fault tetrahedra (SFT), with a size distribution that has a maximum at about 2nm. The formation of vacancy loops (VL's) and SFT's in Cu has been simulated with different potentials as well as their growth and thermal stability. Two types of potentials were used: a long range pair potential (LRPP) obtained from generalised pseudopotential theory and a many body potential (MBP) of the Finnis-Sinclair type. In simulations with the LRPP, significant atomic relaxation is observed: triangular vacancy platelets relax into regular SFT's, small hexagonal clusters form Frank loops, while large hexagonal clusters (with more than 37 vacancies) dissociate into six truncated SFT's, with the side equal to the  $\langle 110 \rangle$  side of the hexagon. With the MPB, none of the planar vacancy platelets relaxes into a VL or SFT, but they remain as unrelaxed microvoids. Further studies using the LRPP show that while VL's can grow without limitations, the growth of SFT's containing more than 91 vacancies is difficult. The growth is based on jog formation and movement and it is shown that although in small SFT's (36 vacancies, 1.8nm), jog formation and movement at the middle of an edge or at a vertex is possible, for large SFT's, absorption of a vacancy in the edge does not provoke jog movement and the system has to store a number of vacancies before the jog moves. The vacancies so stored have a low binding energy, reducing the effective stability of the growing tetrahedron and therefore delaying or preventing the growth.

In order to investigate the effects of bond directionality on the cascades produced in bcc metals, a new type of interatomic potential, which takes into account the angular distribution of the electronic density has been used. The so-called Embedded Defect method has been used by Passianot and colleagues to define an interatomic potential for Mo. The potential was implemented in MOLDYCASKE and displacement cascades produced by primary knock-on atoms (PKA) of up to 50keV have been studied. The calculated orientation dependence of the displacement threshold energy is shown to be in good agreement with experimental values. An important fraction of the defects are in clusters: the fraction of defects in clusters of more than two defects increases to be more than 60 to 70% of the total fraction at PKA energies higher than 20keV. The di-interstitials are  $\langle 110 \rangle$  dumbbells, while the large clusters are formed by  $\langle 111 \rangle$  crowdions and they are glissile in this direction at 300°K. There is evidence of intracascade movement of interstitial clusters.

### **Relating computer simulations to experiments: Simulations of transmission electron microscopy images**

It is important to relate simulation results to experiments. The main experimental technique used to study the defect microstructure is their "post-mortem" (meaning long after their evolution has been completed) observation by transmission electron microscopy (TEM). Correlating TEM image simulations with those of molecular dynamics allows the validation of the atomistic models of the simulated defects, such as dislocation loops and stacking fault tetrahedra, by comparison with

experimental observations. It can also serve the purpose of improving the values obtained from experimental measurements of defect densities, size and type, by corrected analysis of the images.

Predefined crystalline defects were simulated using MD in order to investigate: (i) the visibility of the defect cluster in terms of image contrast, (ii) the limits to which its type can be identified by its TEM image features and (iii) the correlation between its real size and its TEM image size. Interstitial-type Frank loops in Al and SFT's in Cu were analyzed. It appeared that a Frank loop-type cluster defect in Al would in principle be visible experimentally down to surprisingly small sizes (from 2 interstitials upwards), provided that sample preparation is optimised, while SFT's in Cu would be more difficult to identify below a size of 19 vacancies.

Using TEM techniques, we investigated the defect clusters generated by high-energy displacement cascades obtained by MD simulations. The TEM images are simulated using a novel approach for conventional images that is based on the multislice method. The approach was applied to the case of a 10keV cascade in Al, a 30keV cascade in Ni and a 50keV cascade in Cu.

The TEM image simulations show that in Al a 10keV cascade induces diluted damage that will be difficult, if not impossible, to observe experimentally using classical weak beam imaging. In Ni, the 30keV cascade induces a number of defects with some clusters of 10 interstitials or less in size. The weak beam image shows white contrasts related to the defect clusters, which could in principle be observed experimentally. The 50keV cascade in Cu induces larger clusters than in Al and Ni with sizes up to 40 interstitials, some of which would be visible in the experimental weak beam images. However, many of the clusters and all the individual point defects remain invisible in the weak beam image acquired from the three metals. The damage inferred from the weak beam image is less than 20% of the actual damage in all three metals.

Surprisingly, it appears that high resolution imaging using defocus values different from the ones giving a strong lattice image might be used to visualise a larger fraction of the radiation induced defects than that observed with the weak beam technique.

To summarise, TEM image simulations allow us to close the gap between the molecular dynamics simulations and the experimental TEM observations. They provide a unique tool to check the simulation results.

### **2.3.2 The low activation ferritic-martensitic steels**

The low activation ferritic-martensitic steels known as OPTIMAX\* steels have been developed as candidate structural materials for the first wall of future fusion reactors. They contain about 9wt%Cr and their detailed composition is based on that of MANET steels where Ni, Mo and Nb have been replaced by the W, V and Ta low activation elements. A series of casts with different contents of W, Mn and N have been produced from high purity components under clean processing conditions. The main difference between the different casts is that the steel

---

\* OPTIMAX is a low activation steel developed by CRPP in collaboration with Sulzer Innotec

designated as OPTIMAX A contains 0.56wt% Mn and 0.0007wt% N, while the conditions are reversed in alloy B that contains 0.037wt% Mn and 0.003wt% N. In OPTIMAX C and D, the W content was raised to 2wt%, with a higher N content in the alloy D.

Charpy and tensile specimens of OPTIMAX A have been irradiated at a temperature of 523°K in the Materials Test Reactor in Peten (NL) to a dose of 2.5dpa. In parallel, a number of tensile specimens of OPTIMAX A, B, C and D have been irradiated in the PIREX facility, at the Paul Scherrer Institute, with 590MeV protons. These irradiations were performed at ambient temperature and 523°K to doses up to about 2dpa and at 623°K to about 1dpa.

## Testing results

### (i) *The unirradiated steels*

All the specimens were deformed up to fracture. The critical stress was measured on the various stress-strain curves at 0.2% plastic strain. The strain rate sensitivity of the stress was investigated by performing load relaxation experiments all along the stage of plastic deformation of the stress-strain curves. Preliminary analysis of load relaxation experiments concerned only OPTIMAX A. Charpy tests were also performed on the four OPTIMAX compositions.

In the *tensile tests*, the resulting critical stresses range from 402MPa for OPTIMAX B to 517MPa for OPTIMAX C at ambient temperature and from 298MPa for OPTIMAX B to 440MPa for OPTIMAX C at 523°K. The OPTIMAX D (resp. A) exhibits the maximum (resp. minimum) ductility (total plastic strain at fracture) at ambient temperature, while the OPTIMAX C (or A) exhibits the maximum (or minimum) ductility at 523°K.

The activation volumes that were deduced from load relaxation appear quite small, varying between about 40 and  $130b^3$  for OPTIMAX A, depending on the stress value, where  $b$  is the Burgers vector magnitude of a  $1/2\langle 111 \rangle$  dislocation. They decrease with increasing applied stress, with no significant dependence on temperature.

*Charpy tests* revealed that the unirradiated OPTIMAX steels exhibit a ductile-to-brittle transition temperature (DBTT) between 190°K and 250°K, depending on the alloy composition, far below room temperature. The lowest DBTT value was found for the OPTIMAX A.

### (ii) *Post-irradiation results*

The *tensile behaviour* of the OPTIMAX steels is strongly affected by proton irradiation at ambient temperature. In particular, a drastic increase in the critical stress is observed, together with a decrease of the total plastic strain at fracture. Both phenomena, namely the hardening and the loss of ductility, are strongly and positively dependent on irradiation dose. The effect of irradiation at 523°K is similar, at a lower level of hardening, the tests having been performed at the same temperature as that of the irradiation.

In terms of composition, after proton irradiation at ambient temperature to a dose of 1dpa, the OPTIMAX C exhibits the lowest critical stress and the highest ductility, while at the opposite the OPTIMAX B (or A) exhibits the highest critical stress (or the lowest ductility). After irradiation at 523°K to the same dose, the OPTIMAX A exhibits the lowest critical stress and ductility, while the OPTIMAX C (or B) exhibits the highest critical stress (or the highest ductility).

Taking the relative values with respect to those of unirradiated specimens, the hardening increase by proton irradiation at ambient temperature (or 523°K) to a dose of about 1dpa is at a minimum for OPTIMAX C (or A) and a relative loss of ductility that is minimum for OPTIMAX A at both irradiation temperatures. Although the absolute critical stress values that were measured for proton-irradiated OPTIMAX steels appear much smaller than those previously measured

for the F82H steel, their hardening behaves the same way as a function of dose, increasing with the cube root of the dose, Fig. 2.3.3.

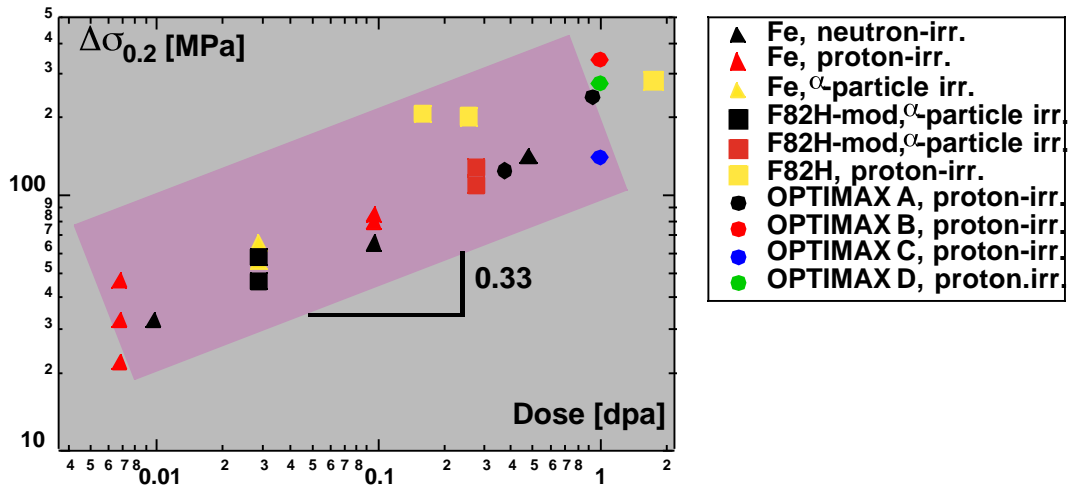


**Fig. 2.3.3** The dose dependence of the radiation hardening ( $\Delta\sigma_{0.2} = \sigma_{0.2}^{irr} - \sigma_{0.2}^{unirr}$ ) of ferritic-martensitic steels.

The effects of neutron-irradiation at 523°K to a dose of 2.5dpa on the DBTT of OPTIMAX A have been investigated. It was found that while the DBTT value of unirradiated specimens is about 190°K with an upper shelf energy of 9J, it increases to about 268°K for irradiated specimens, while keeping the same upper shelf energy value. Hence, the shift of the DBTT appears much smaller for OPTIMAX A (78°K) than for F82H (141°K), see Fig. 2.3.4. F82H is another promising low activation material of slightly lower Cr and higher W content with respect to OPTIMAX A. In addition, and contrary to F82H (326°K), the irradiation-induced DBTT value of 268°K found for OPTIMAX A is still far below the ambient temperature.

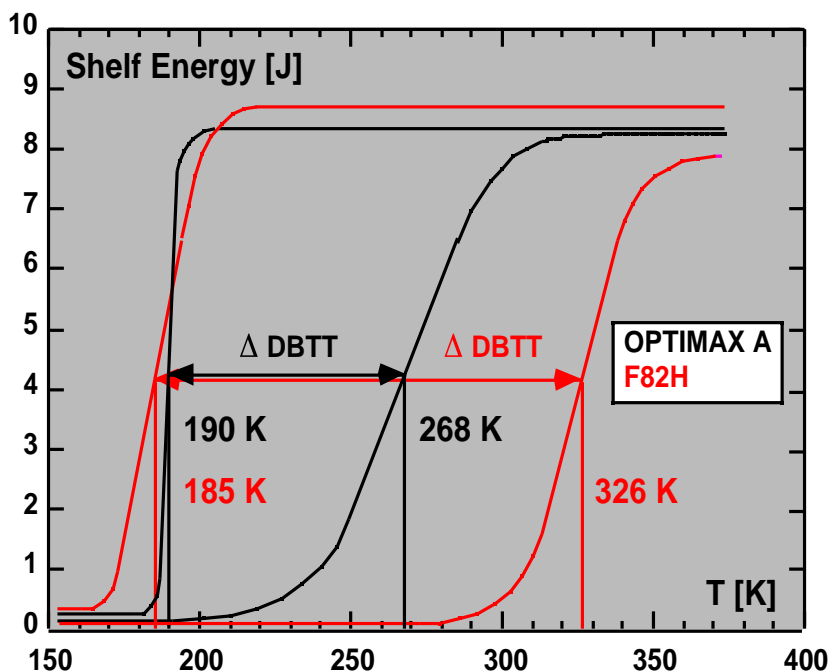


**Fig. 2.3.4** The behaviour of the ductile-brittle transition temperature (DBTT) after neutron irradiation to 2.5dpa.

### Electron microscopy of LAS

In order to reduce magnetism and radioactivity, sample preparation was optimised and a new procedure was developed. Samples are punched to produce 1mm disks. These disks are then inserted in a 1mm hole punched into the centre of a 3mm disk of 316 stainless steel. The assembly is then glued with epoxy and mechanically polished to about 100 $\mu$ m before the final electropolish using 20% perchloric acid and 80% methanol at 0°C and 18V. Relative to a sample that was punched to 3mm, no modification of the structure that could have been induced by the 1mm punching could be detected. Time between sample preparation and its transfer to the TEM is about 10 minutes and samples are kept in water-free ethanol. Samples older than 4 hours are generally discarded. These are important steps to minimise oxidation. It showed for the first time radiation damage in ferritic steels at low doses, such as 0.7dpa (F82H).

TEM observations show that irradiations with protons lead to the formation of few visible defect clusters with sizes of 1 to 2nm, with no clear difference in size and density with dose and temperature. The neutron irradiation to 2.5dpa at 250°C also introduces few visible black dots. This indicates a good resistance to radiation damage accumulation. A few faceted cavities were shown up. The carbides become amorphous for the irradiations conducted at room temperature, while at 523°K they remain crystalline.

The **F82H ferritic/martensitic steel** developed in Japan is based on a Fe-9Cr-2W(V,Ta) composition. High energy protons as well as fission neutrons are used to simulate the irradiation effects that the material will suffer in the fusion environment. The differences in PKA spectra and in He production rates between the two types of irradiation may lead to differences in the irradiation damage of the F82H microstructure. Using TEM we investigated a range of F82H samples that

were irradiated (i) with 590MeV protons, (ii) with fission neutrons and (iii) with 590MeV protons in PIREX followed by fission neutrons in the reactor in Studsvik. The latter experiment allows us to vary the He production rate for a given dose. Total doses ranged from 0.3 to 10dpa and temperatures ranged from room temperature to 310°C.

Clusters are visible in TEM for doses of 0.7dpa and above. Defect density and size increase with dose and apparently they follow a unique dependency with it, irrespectively of the type of particle, proton or neutron, see Fig. 2.3.1. For the protons, the defect density does not seem to have reached saturation for the studied doses (1.7dpa). In the case of the neutron irradiations, defect density has reached saturation at a dose value between 2.5dpa and 10dpa. Coarsening occurs above 2.5dpa. At 2.5dpa, the defect clusters have grown enough, relatively to the case of lower doses, to be resolved as dislocation loops. As in OPTIMAX A, carbides are amorphised in the case of the room temperature irradiation with protons to a dose of 1.7dpa. In all other cases it appears that the carbides remain crystalline. Temperature is the controlling parameter for amorphisation. There are no observable cavities, even at the highest studied dose of 10dpa. This indicates a good resistance to swelling.

### **2.3.3 The constitutive behaviour and fracture properties of ferritic/martensitic steels.**

The constitutive and fracture behaviour of an advanced ferritic-martensitic steel of the 7-9Cr class was characterised in support of developing physically based models for accurately predicting defect tolerance in flawed fusion structures, based in large part on small specimen test methods. Special attention was paid to the modelling of the constitutive behaviour and to the reconstruction of the fracture toughness temperature curve. The constitutive behaviour was investigated over the temperature range 77°K-723°K at three different strain-rates ( $2.8 \times 10^{-4} \text{s}^{-1}$ ,  $2 \times 10^{-3} \text{s}^{-1}$ ,  $2 \times 10^{-2} \text{s}^{-1}$ ). It was determined by tensile tests and a multi-term constitutive equation was derived. Small compact tension specimens (0.2TCT) were used for fracture toughness measurements in the ductile-brittle transition region. Finite Elements Modelling (FEM) of compact tension specimens, using the previously determined constitutive behaviour, was carried out with ABAQUS™ 5.8, in order to reconstruct the fracture toughness temperature curve using a critical stress-critical area model.

The mechanical testing and the modelling were performed for the tungsten-stabilised F82H steel (8Cr-2W-VTa). It is a fully martensitic steel, investigated as part of the IEA Fusion Materials program on ferritic/martensitic steels. The steel was heat-treated by normalising at 1313°K for 0.5h and tempering at 1013°K for 2h.

A "parabolic" type of strain-hardening was found at all temperatures and strain rates investigated. The overall flow stress, which depends on the plastic strain  $\epsilon_p$ , plastic strain rate  $\dot{\epsilon}_p$  and temperature T, can be considered as the sum of the yield stress,  $\sigma_y$ , and the contribution from plastic deformation,  $\sigma_{pl}$ , primarily resulting from dislocation-dislocation interactions. The increase of  $\sigma_{pl}$  with strain, *i.e.* the strain-hardening  $\sigma_{pl} = d\sigma_{pl}/d\epsilon_p$ , is determined by the evolution of the dislocation microstructure in the material. It appears that a simple linear relation between  $\sigma_{pl}$  and  $\epsilon_p$  holds for plastic strains larger than 0.01 and at all investigated

temperatures. An exponential type of stress-strain relation results from the previous linear relation and the temperature and strain rate dependence of  $\sigma_{pl}$ , if any, is contained in the parameters which define the exponential law. Simple relations describing the hardening coefficients and the yield stress temperature dependence have been proposed. These sets of relations are further used as an input for the FEM of the fracture behaviour.

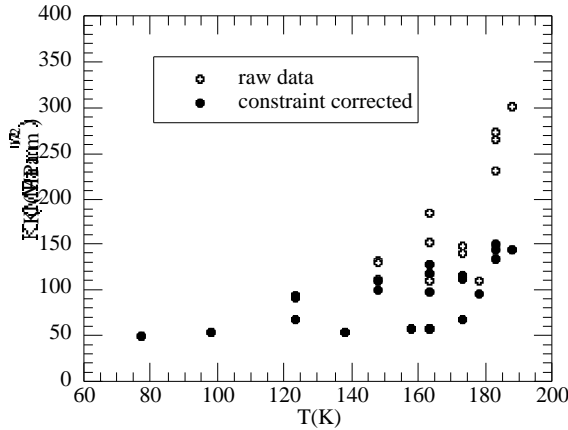


**Fig. 2.3.5** Fracture toughness as a function of temperature for the F82H steel.

As part of an extensive study of the effect of specimen geometry and specimen size on fracture toughness, a series of fracture toughness tests were carried out on fatigue pre-cracked 0.2T compact tension (CT) specimens with  $a/W=0.5$  and a specimen thickness (B) to width (W) ratio of  $B/W=0.5$ . The study was focused on the low temperature transition region. For temperatures lower than 180°K, all specimens failed by quasi-cleavage, in some cases after a large amount of plastic deformation and crack blunting, resulting in the so-called "loss of constraint". Constraint loss is primarily associated with plasticity encompassing a large fraction of the uncracked ligament of length b. A method for accounting for the loss of constraint based on a local criterion for fracture has been used to correct the data, Fig. 2.3.5. This method is based on FEM and the correction is determined by calculating the large scale to small scale yielding ratio of the  $J/J_{ssy}$ , required to produce the same area within a specified non-dimensional principal stress contour normalised by the yield stress,  $R = \sigma_p / \sigma_y$ . The proposed method can be used to scale fracture toughness measurements obtained with different kinds of geometries as well and appears to be a promising technique to deal with small specimens to investigate fracture properties.

### 2.3.4 The behaviour of Titanium-base alloys

The attachment of the first wall modules of the ITER FEAT vacuum vessel is made using flexible connectors made out of titanium alloys. Due to the lack of irradiation data, an assessment of the tensile and fatigue performance has been carried out at CRPP using protons for the simulation of the fusion neutrons.

Two candidate alloys have been looked at: a classical two phase Ti6Al4V alloy and a monophasic alpha alloy Ti5Al2.4Sn. The unirradiated tensile performance of both alloys is roughly identical, the total elongation being slightly higher in the alpha+beta alloy. The irradiated performance is very different as shown in Fig. 2.3.6. The irradiation hardening is much stronger in the alpha+beta alloy

compared with the alpha alloy and the ductility is correspondingly strongly reduced. A precise explanation for the difference in behaviour is not yet available but it is thought that the chemical composition could be the dominating factor. Despite the fact that all fractures were ductile over the strain rate range studied, irradiation embrittlement could be a concern at higher strain rates.

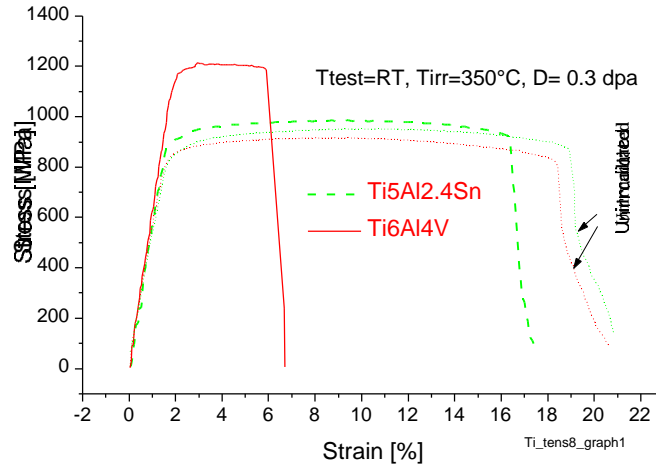


**Fig. 2.3.6** *Deformation curves before and after irradiation with 590MeV protons, tested at room temperature*

Two different regimes have been observed in the behaviour of the cyclic stresses. At a high imposed strain, softening is almost absent in the Ti6Al4V and small in the Ti5Al2.4Sn. At a low imposed strain and for both alloys, during the first period of life, cyclic softening takes place up to about 800 cycles. Subsequently a transition occurs after which a regime of cyclic hardening appears. The TEM observations have shown that the secondary hardening may be due to dislocation interactions with dislocation debris, but this hypothesis needs to be confirmed by more observations.

In both materials and for all test conditions, the compressive stress of the hysteresis loop was found to be larger than the tensile stress. This characteristic has been observed for all tested conditions, in both alloys. The stress asymmetry seems to be triggered by the plastic deformation. The fatigue resistance of the Ti5Al2.4Sn alloy is slightly better than that of the Ti6Al4V alloy. The irradiated fatigue performance of both alloys is acceptable but the fatigue endurance performance is superior in the Ti5Al2.4Sn compared with the Ti6Al4V alloy. SEM micrographs have shown that all fractures were trans-granular and ductile. At this stage of the study it seems that the monophase alloy is more suitable for ITER, from the point of view of the resistance to irradiation.

### **2.3.5 The irradiation hardening of austenitic stainless steels**

In the frame of a study in which the effects of the different parameters that can contribute to Irradiation Assisted Stress Corrosion Cracking (IASCC) in stainless steels were analysed, the basic mechanisms of radiation hardening in stainless steels were investigated. The cracking susceptibility of steels is a relevant problem for the ageing and safety of nuclear power plants and furthermore for any facility

operating under irradiation. However, the amount of data available in the region of interest is insufficient.

The irradiation induced defect density and size distribution were obtained from systematic investigations using transmission electron microscopy (TEM). It was concluded that the irradiation defects are Frank loops and black dots (probably small loops that are not resolved in TEM) at low doses (<0.2dpa). With increasing dose, the Frank loop type defects become more prominent in the distribution. The loops are faulted and no stacking fault tetrahedra were found. The loop density reached saturation at 1dpa. The mean loop size at 0.15dpa is about 2nm and with increasing dose, the mean loop size increases to approximately 8nm. SS316L shows systematically smaller loop sizes than SS304L. The loop density is between  $1.2 \cdot 10^{23} \text{m}^{-3}$  at 0.15dpa and  $3 \cdot 10^{23} \text{m}^{-3}$  at 7.5dpa for SS304L. In SS316L smaller densities are observed, in the range of  $1.7 \cdot 10^{22} \text{m}^{-3}$  and  $1.8 \cdot 10^{23} \text{m}^{-3}$ . The increase in loop density with dose was found to be larger for SS316L than SS304L.

Stress-strain relationships and stress relaxation tests were obtained at different temperatures. The results show that the irradiation hardening increases linearly with the dose to a saturation level around 1dpa, see Fig. 2.3.7. The saturation level is higher for SS316L than for SS304L, indicating a stronger hardening in SS316L.

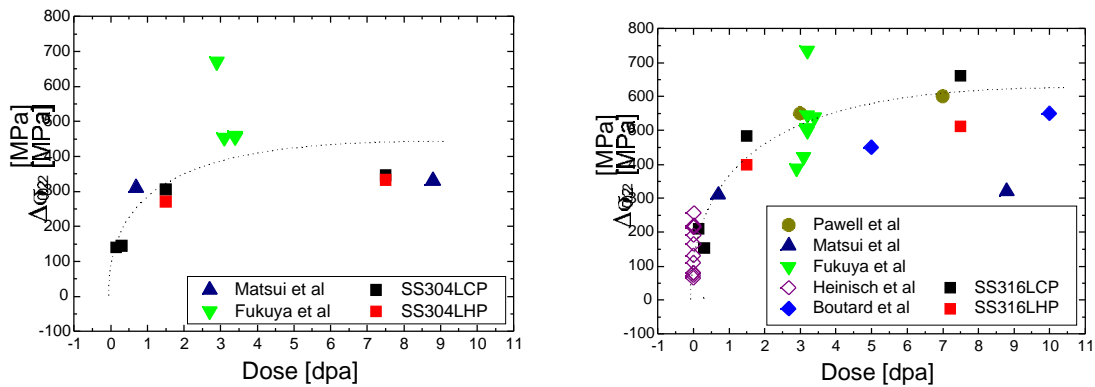


**Fig. 2.3.7** Increase in yield strength as a function of dose for (a) SS304 and (b) SS316, comparison between present results and those in the literature. The sources of the data are indicated in the legends.

As indicated in Fig. 2.3.8, both twinning and channelling deformation modes were found in the stainless steels. SS304L and SS316L show twinning as a mode of deformation at low doses and room temperature. The twins, free of defects, are very narrow and the twin density increases with increasing stress. At higher doses (>1dpa) in high purity SS304L tensile tested at 550°K, dislocation channelling was observed. At the same temperature, the deformation mode of SS316L is twinning, like at room temperature. The dislocation channel density is qualitatively smaller than the microtwin density.

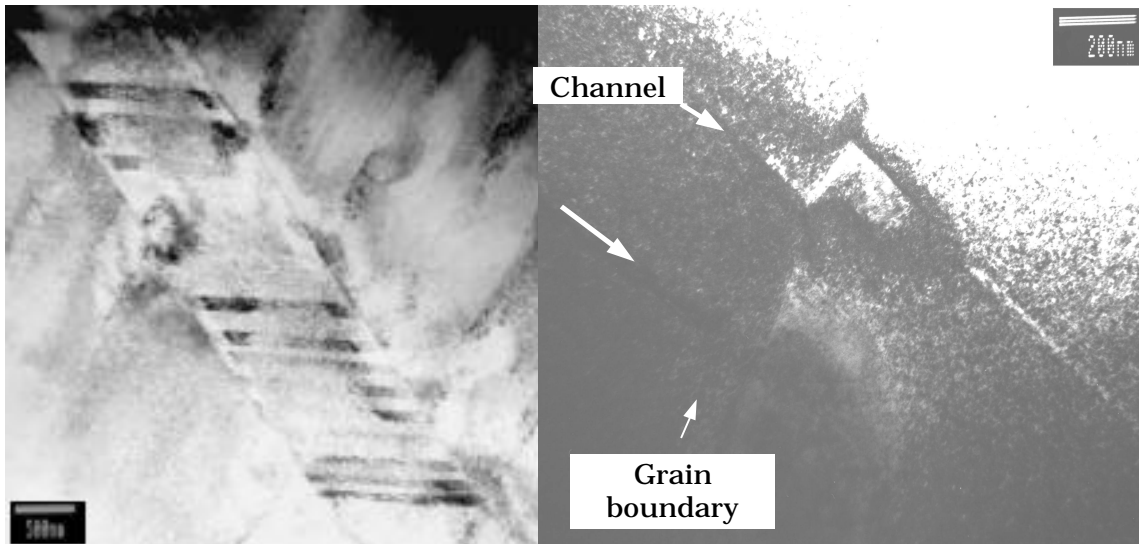


**Fig. 2.3.8** *Stainless steels neutron irradiated to 1.5dpa and tested to necking at 550°K. (a) High purity SS316L, bright field picture shows intersections of different types of twins. (b) High purity SS304L. The bright field picture shows the intersection between a grain boundary and two dislocation channels.*

The strain released at the grain boundaries seems to be important in both cases. However, the high density of microtwins seems to accommodate the strain more easily. The dislocation channels tend to highly localise the strain at grain boundaries and induce cracking.

The observation of surface grain boundaries effectively revealed that SS304L shows microcracking at grain boundaries at lower doses than SS316L. With increasing dose, the cracking seemed to increase and reached a dramatic level, at which the entire gauge length is strongly cracked.

The link between these results and IASCC was provided by a comparison with corrosion studies performed by ABB Sweden on the same steels. It was concluded that the bad resistance to IASCC of SS304L can be explained by the highly localised deformation induced by the dislocation channelling mode of deformation. Furthermore, the hardening by itself seems not to be a good criteria for IASCC susceptibility, but the deformation mode should be considered.

Small Angle Neutron Scattering (SANS) is a non destructive method to characterise the irradiation defect microstructure that samples a larger volume than TEM and is therefore complementary to it. A procedure has been developed to measure the highly radioactive samples using the SANS facility at the SINQ (PSI).

Preliminary SANS measurements have been performed in stainless steel SS316L irradiated up to a neutron dose of 1.5dpa. The purpose of this preliminary investigation was to measure the scattering induced by the irradiation produced defects. The comparison with an unirradiated sample of the same steel showed a clear difference in scattering intensity, which can be related to the presence of irradiation defects and is shown in Fig. 2.3.9, as a function of the scattering vector. It can be clearly seen that the scattering intensities diverge around  $0.4\text{nm}^{-1}$  (the grey zone in Fig. 2.3.9).

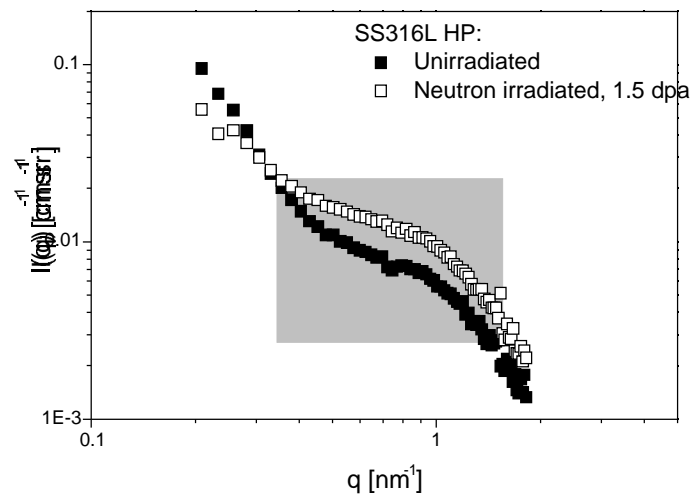


**Fig. 2.3.9** *Scattering intensity as a function of the scattering vector  $q$ . The range of interest is within the grey square, for samples unirradiated and neutron irradiated to 1.5dpa.*

A rough estimation of the defect distribution which could induce such scattering intensities gave an average size about 1.5nm. The investigation performed using TEM gave a mean loop size around 6nm. There are several factors that can contribute to this difference. First, the TEM loop size measurements can lead to an error of up to 15%, because of the contrast conditions and enlargement. Furthermore, the mean loop size takes into account loops which are larger than 1nm. The smaller defects are seen as black dots as they are smaller than the conventional TEM resolution. Furthermore, because of the high loop density, the black dots can not be correctly measured. It can be concluded that the real mean defect size is smaller than that measured using TEM. The TEM and SANS techniques are therefore complementary and will provide a better analysis of the irradiation induced defect microstructure.

## **2.4 Superconductivity**

The development of the huge superconducting magnet systems for the Next Step (ITER) is one of the major areas of fusion technology. Globally coordinated by JCT, a substantial part of the program is contributed by the four leading EU laboratories in close cooperation. Our part is based on traditional expertise in magnet and conductor development, our unique large test facilities and corresponding experience.

CRPP operates SULTAN (SUpraLeiter TestANlage) at PSI-Villigen, a large bore (60cm), high field (11T) superconducting split coil system with a flexible, high power (1.4kW) cryogenic circuit and high current DC transformer (100kA) as a reference test facility for full size prototype conductors and their joints developed by the ITER partners EU, JA, RF and formerly the US, Fig. 2.4.1.

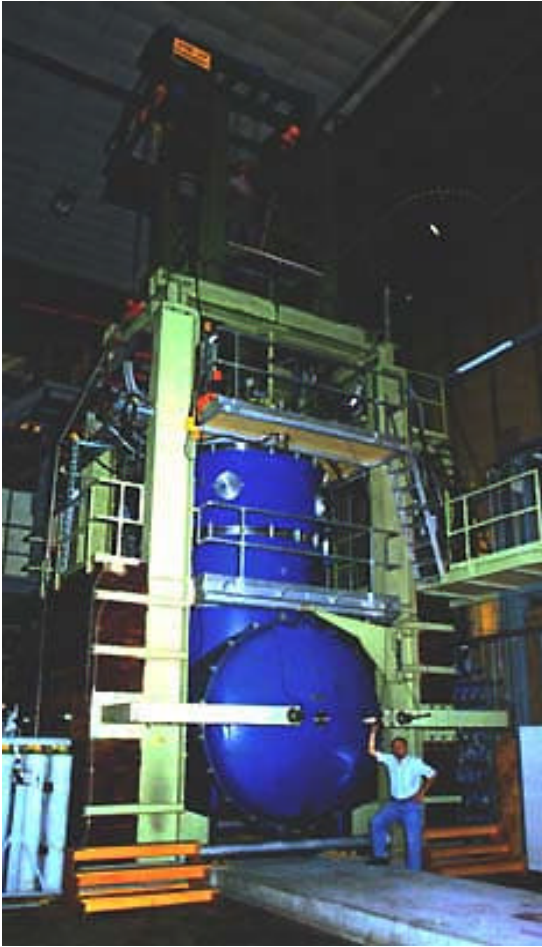


**Fig. 2.4.1** *The SULTAN test facility*

According to the resulting relevant expertise, considerable contributions of the group in conductor R&D provide a useful feedback to the Fusion Technology Program. These efforts are typified by our joint development (Good Joint) and stability investigations (SeCRETS) on the experimental side and our stability and quench analysis calculations on the engineering side.

Recently acquired experience with High  $T_c$  (high critical temperature or  $HT_c$ ) superconductors have enabled us to contribute not only to the development of  $HT_c$  Current Leads for ITER with a significant potential for saving on refrigeration power of the magnet system, but also to the successful development and test of a  $HT_c$  Superconducting Cable for Power Transport, SULEIKA (SUpraLEiterKAbel), a collaborative technology transfer exercise with Swiss industry.

#### **2.4.1** *Superconductivity studies*

The superconductivity studies have focused on the heat slug propagation analysis of the ITER Toroidal Field Model Coil (TFMC). A prerequisite to this predictive analysis has been the validation of the computer code Gandalf vs. heat slug results of the QUench Experiment on Long Length (QUELL), performed in the SULTAN test facility. A renewed interest has arisen concerning the question of heat slug

propagation in dual channel cable-in-conduit conductor (CICC), in connection with the test program of the ITER Model Coils. In the TFMC an experimental evaluation of the superconductor critical properties will only be possible by heating the helium upstream of the joint, then letting it flow through the joint and downstream to the high field region in the conductor, where a quench could be initiated. Whether this strategy works or not will depend on the delicate balance between the probably degraded properties of joint vs. conductor, and the magnetic field dependence of the current sharing temperature. A similar situation will occur in the test program of the inner/outer modules of the Central Solenoid Model Coil (CSMC) experiment. The CRPP studies, performed in collaboration with CERN, have been partially financed by the EU Fusion Technology Program.

### Validation of the QUELL heat slug propagation with the 2-channel model

The Gandalf code was extensively used in the interpretation of the thermal hydraulic results produced by QUELL. One of the major results of this work was that the code is able to reproduce general scaling and overall behaviour of the relevant parameters such as normal zone length, resistive voltage, maximum cable temperature and pressure, with an accuracy which is acceptable for design purposes. At the same time this work has shown that a significant discrepancy was still present on temperature traces especially when slow transients were considered, such as in heat slug propagation experiments. The cable model used in Gandalf up to version 1.8 had independent flow conditions, i.e. velocity in cable bundle and in central cooling channel (hole), but was limited to identical thermodynamic states (Fig. 2.4.2). Following the development of our model, we have increased the capabilities of Gandalf version 2.0 to treat fully independent parallel flows of helium coupled through heat and mass transport at their interface, i.e. a configuration typical of the dual channel CICC in QUELL and in the ITER Model Coils.

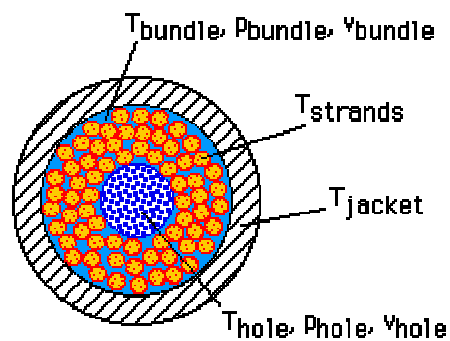
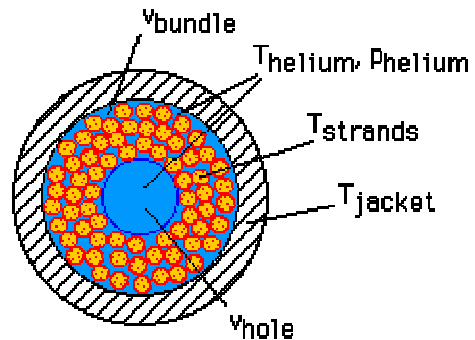
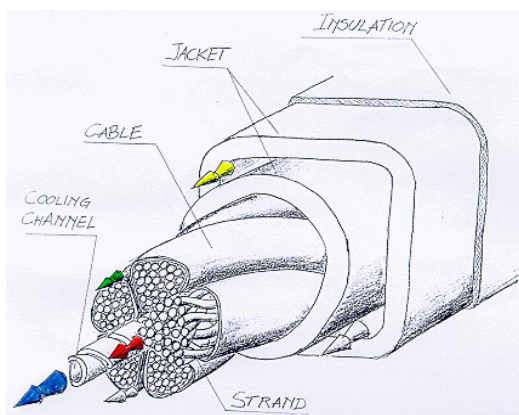


**Fig. 2.4.2** *Left: Sketch of the improved cable model implemented in Gandalf, showing schematically a superconducting cable and an insulated jacket cooled by an arbitrary number of parallel helium flow channels (arrows). Right, top: 1-Channel model implemented in Gandalf up to version 1.8. Right, bottom: 2-Channel model implemented in Gandalf 2.0 ( $T$  is temperature,  $P$  is pressure and  $v$  is velocity).*

Propagation of a heat slug is a relevant way to assess the thermal hydraulic characteristics of a CICC with forced flow cooling. The method is based on the observation of how the conductor reacts to the heat input by an external heater, at zero current and magnetic field. Simulations of these tests have focused on 2 inductively heated runs with input energy of 39J and 303J, and 2 resistively heated runs with 175J and 1591J (run 12). Experimental time histories of the helium pressure at the inlet/outlet were used as hydraulic boundary conditions in the simulations. The agreement between the experimental and the simulated temperatures is good and the improvement introduced by the full two-channel model (Gandalf 2.0) with respect to the single channel approximation (Gandalf 1.8) is remarkable, Fig. 2.4.3. Work is in progress to improve the model still further, implementing an arbitrary number of parallel cooling channels and a more realistic electrical description of the cable, considering the current distribution among the strands.

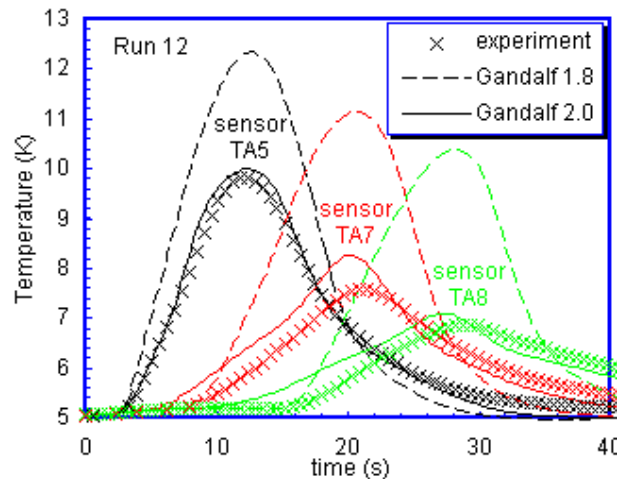


**Fig. 2.4.3** *Validation of the heat slug propagation in QUELL with Gandalf. Comparison of measured and calculated temperature traces at several sensors (TA4, TA5, TA7 and TA8) downstream of the heater during the heat slug run 12.*

### Predictive heat slug propagation in the TFMC

The TFMC, to be tested in the TOSKA facility at FZ Karlsruhe, Germany, is a racetrack coil consisting of 5 double pancakes (DP11/DP12-DP51/DP52), each with two joints at the inner and outer sides of the coil. Only the double pancake DP11/DP12 is equipped with external heaters. The TFMC conductor is a circular CICC using Nb<sub>3</sub>Sn strands and a thin stainless steel jacket. The supercritical helium flows in two channels, namely the central cooling channel and the cable

bundle, separated by a thin stainless steel spiral. The heat slug generated by the external heater propagates through the joint and downstream to the high field region of the conductor. Here we present the predicted heat slug propagation and quench initiation analysis for a single coil test, operating current 80kA, heat slug in pancake DP11, using simplified models of the hydraulic circuit and the joint. The analysis is performed with Gandalf version 2.1. The uncertainty in the presently available set of joint input data is assessed parametrically. The main components of the model are: conductor, joint, heater and cryogenic system. The joint electrically connects adjacent pancakes on the same radial plate. Recent measurements in SULTAN have shown that the electrical resistance of these joints is  $<2\text{n}\Omega$ . A detailed definition of the joint hydraulic properties is difficult and an accurate assessment is in progress. In this analysis, (a) the heat flux generated in the inner joint is uniformly distributed along the 50cm joint length, (b) the joint superconducting properties are not degraded and (c) the heat transfer perimeters are reduced with respect to the conductor values. The complex cryogenic circuit of the TOSKA facility is simulated with a simplified cold closed-loop system model, including a volumetric pump, a heat exchanger, a pressure controller and a pipe hydraulically connected in parallel to DP11, to simulate the remaining 9 pancakes. The analysis is performed in a realistic range of helium mass flow rates  $G$  (6-18g/s). The heat is generated by the DP11 external heater by means of linear ramps, with power and duration as inputs.

When only one of the 10 parallel hydraulic channels is heated, an instability of the cryogenic system occurs referred to as helium choking. The helium temperature increases and the density decreases near the inlet of DP11; as a consequence the mass flow in the latter decreases while more helium flows in the unheated channels. During the heating  $G$  keeps decreasing and reaches a minimum at quench initiation. The global results are presented in the form of the external heater power necessary to initiate a quench  $Q_{\text{qu}}$  at a time  $t_{\text{qu}}$ . For every helium mass flow rate the quantity  $Q_{\text{qu}}$  is plotted as a function of the heating ramp slope. Three characteristic regimes can be identified in Fig. 2.4.4. At low slopes (regime R1)  $Q_{\text{qu}}$  is quasi constant and quenches are initiated in the conductor. At intermediate slopes (regime R2)  $Q_{\text{qu}}$  is quasi constant, but at a lower value, and quenches are still initiated in the conductor. At higher slopes (regime R3)  $Q_{\text{qu}}$  is unchanged but the quench is initiated in the joint. The transition between these limiting cases is continuous. The transition R1-R2 depends on the residence time of the helium in the coil  $t_{\text{res}}$ , a function of  $G$  (e.g. 80s at 6g/s and 160s at 18g/s). Regime R1 is typical of quenches occurring at  $t_{\text{qu}} > t_{\text{res}}$  while regimes R2 and R3 are typical of quenches occurring at  $t_{\text{qu}} < t_{\text{res}}$ .

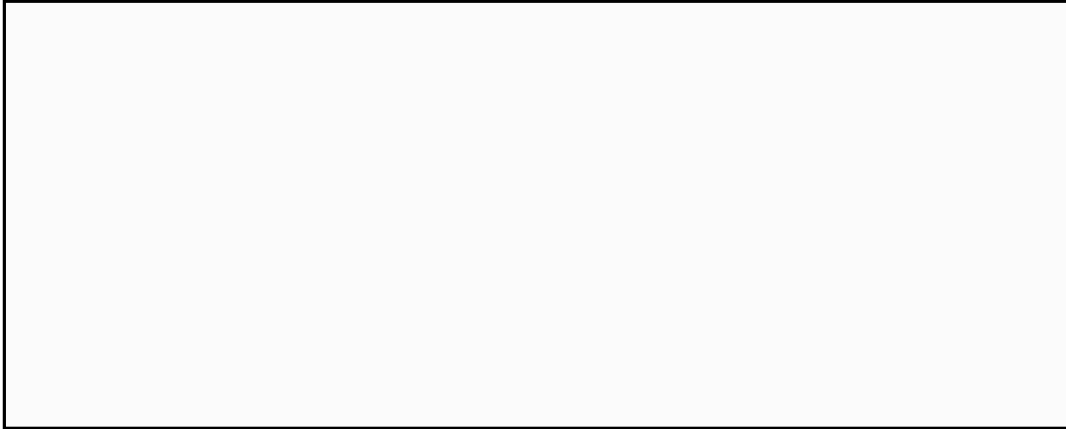


**Figure 2.4.4** *Predicted heat slug propagation in the ITER FT Model Coil. Summary of results using linear heating ramps. Open symbols indicates cases in which the quench is initiated in the high field region of the conductor, solid dots indicate cases in which the quench is initiated in the joint. Left: Nominal conditions (the joint electrical resistance is 2nOhm). Right: details at 6g/s, including cases at nominal/double joint resistance, and cases in which the hydraulic properties of joint and conductor are the same (HPJ=HPC).*

The flow instability between heated and unheated pancakes, stronger at lower mass flows, should be minimised. During the test of the conductor critical properties, the heater must be operated using ramps with low enough slopes to avoid a quench in the joint, i.e. far away from the transition R2-R3. This transition is more dependent on electromagnetic and hydraulic properties of the joint when cooling with low  $G$ . The result of this analysis is twofold. Firstly, the range of the operational regime R1 diminishes considerably when reducing the mass flow, i.e. the margins are acceptable at 18g/s, marginal at 12g/s and insufficient at 6g/s. Secondly, the joint hydraulic properties, in particular at low mass flows, are critical and partly unknown.

Tests of the TFMC are due to start in the second half of 2000. The validation of this predictive analysis against experimental results, still in progress, will determine whether an even finer tuning of the model is necessary.

#### **2.4.2 Short sample and joint testing in SULTAN (Good Joint)**

A joint layout for the ITER Nb<sub>3</sub>Sn conductors has been developed, manufactured and tested at CRPP, based on sections of the CS1 conductor. The design was aimed at improving the original concept proposed by ITER-JCT, using the lessons learned by the past development by the Home Team. A CS1 conductor section has been tested in SULTAN for DC performance, AC losses and transient field stability. The current distribution in the cable cross section has been varied artificially by chopping the hairpin joint of the two conductor sections.

The critical current  $I_c$  test actually turns into a quench current test,  $I_q$ , as early voltage builds up gradually far away from the irreversible take-off. The formulae in the ITER design and the scaling law parameters ( $B_{c20m}=32.2T$  and  $T_{c0m}=17.4^{\circ}K$ ) are used to scale the strand performance, the dotted line in Fig. 2.4.5, to the SULTAN

test conditions. If the interstrand resistance in the cable is very low, the current distribution re-adjusts with minimum voltage to the local field distribution at high field. In this case, all the strands quench simultaneously and only the average self-field must be added to the background field. In the case of more insulated strands, the peak self field must be added. Realistically, we may assume that the interstrand resistance is very low within the individual subcables, and very high between the subcables wrapped with high resistivity Inconel foils, the “one subcable” model. The above predictions assume a balanced current distribution

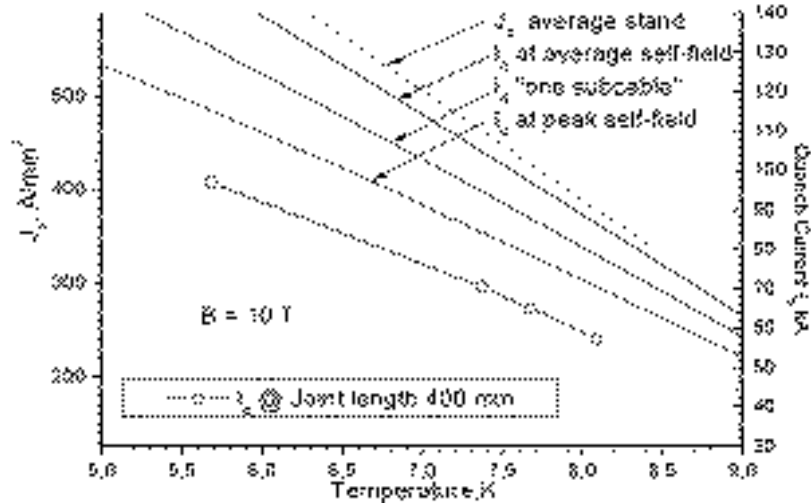


**Fig. 2.4.5** *Quench current with homogeneous current distribution from average strand data (dashed line), with different assumptions on interstrand resistance and self-field (solid lines) and test results*

among subcables. However, the joint is shorter than the cable pitch and some subcables have either poor or no contact to the copper saddle. Figure 2.4.6 summarizes the  $I_q$  results for the three joint lengths, with the “one subcable” prediction corrected respectively by a factor 1.2, 1.35 and 1.48. The model to estimate the correction factors contains many parameters (transverse conductance, number of connected strands and resistance of the connections, additional current re-distribution inside the joint) which can be used or abused to fit the results. However, the general trend of the predictions confirms that the observed  $I_q$  at joint lengths shorter than a cable pitch is an issue of local current distribution, rather than a conductor degradation.

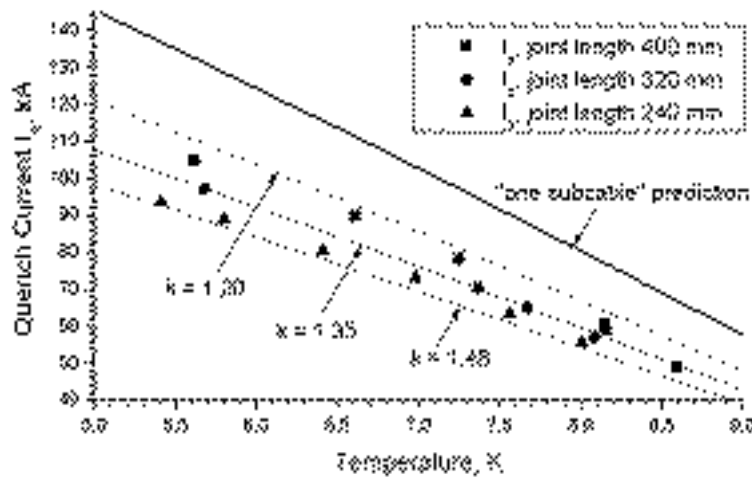


**Fig. 2.4.6** Quench current results at 10T for different joint lengths (symbols) and the “one subcable” prediction, with applied correction factors.

The AC losses are measured by gas flow calorimetry with a sinusoidal transverse field ( $B=0.3T$ ) produced by a set of pulsed coils. From the initial slope of the loss curve, Fig. 2.4.7, the coupling currents constant is  $n=3.1\pm 0.3ms$ . Compared to the interfilamentary loss for a commercial (VAC) strand ( $n=0.62ms$ ), the loss increase is marginal. The loss is also measured as a function of the background field, up to 10T: after subtraction of the hysteresis loss, the coupling loss is half the value observed at 2T, suggesting  $n(10T)$  1.5ms. The AC losses in a CIC of Cr plated  $Nb_3Sn$  strands increase when a transport current is applied with a background DC field. The same field sweep ( $f=2Hz$ ,  $B=0.3T$ ) was applied for different combinations

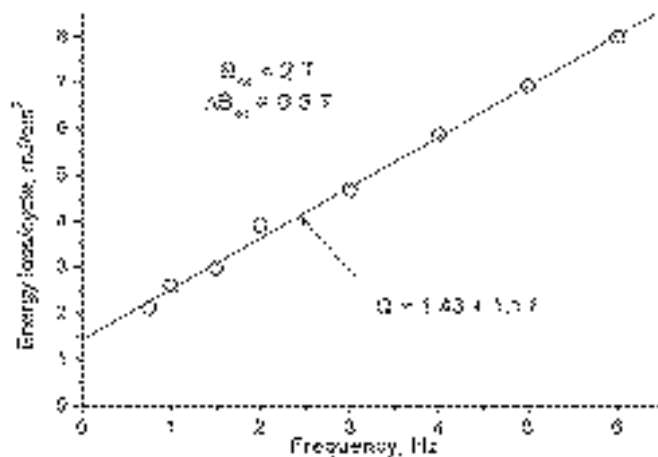


**Fig. 2.4.7** Loss curve for sinusoidal applied field without transport current. The dots are the average of A and B legs

of  $B_{dc}$  and  $I$ , keeping constant the transverse load  $B_{dc}xI$  (600 and 300kN/m). The loss results, after subtracting the hysteresis loss, are plotted in Fig. 2.4.8 as a function of the transport current: the lines interpolate the loss measured at constant transverse load. The slope of the interpolation lines vs. current is evidence that the loss increase is mostly due to saturation loss rather than to a decrease of the interstrand resistance: otherwise the loss should be strictly constant for constant load. The power dissipated by the saturation loss is supplied by the current source, not by the applied AC field. The saturation losses are not reduced by high resistivity barriers, which hamper the interstrand current sharing.

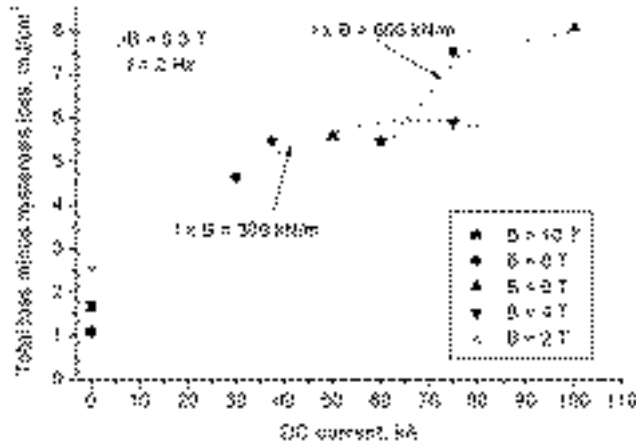


**Fig. 2.4.8 AC loss as a function of the transport current for two constant transverse loads  $I \times B$**

For the stability experiments, the pulsed coils are supplied by a capacitor discharge, at a 9Hz resonance frequency. The discharge is cut by a thyristor switch after one full cycle. For a stability test, the background field and the sample current are set to a constant value. The operating temperature is adjusted to obtain a temperature margin  $\Delta T = T_q - T_{op}$ , where  $T_q$  is the DC quench temperature. Then the pulsed field is applied with increasing amplitude until a quench occurs. The peak-to-peak amplitude of the pulsed field is plotted in Fig. 2.4.9 vs. the temperature margin at 10T background field for two levels of operating current, 50 and 75kA. For the same operating conditions (background field, current and temperature), the ability of the conductor to withstand a transverse field transient decreases after having chopped the joint, i.e. after having imposed a strong current imbalance. The same trend is observed for stability vs. operating current. This behaviour is consistent with the degradation of the DC quench temperature,  $T_q$ , observed after chopping the joint.

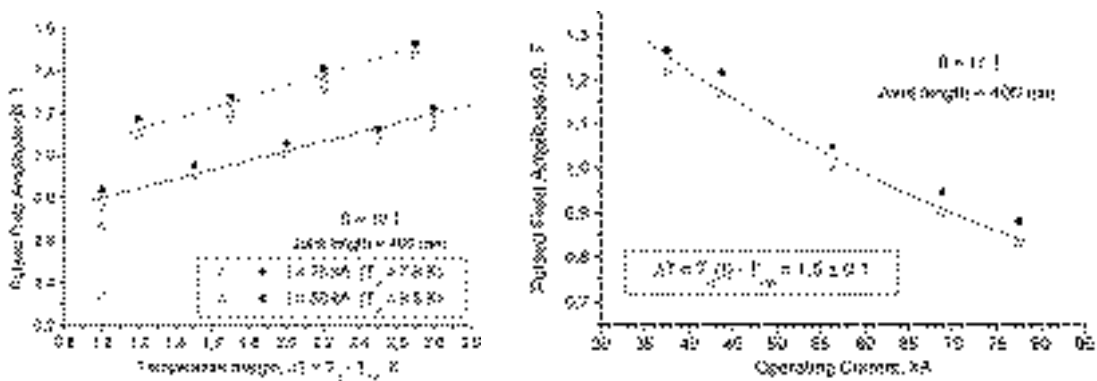


**Fig. 2.4.9 Stability vs. temperature margin, left, and vs. operating current, right.**

The joint resistance results are plotted in Fig. 2.4.10. The quench current at the joint is always larger or equal to the conductor quench current at the same background field. The loss curve of the joint is compared to the one of the conductor in Fig. 2.4.11 and taken at a background field of 2T. From the peak of the loss curve, occurring clearly above 2Hz, an upper limit for the loss constant can

be drawn. The eddy current loss in the copper saddle can be roughly estimated to be in the range of 150ms from the size of the largest cell ( 20 x 18mm). The coupling loss in the subcables soldered to the saddles is likely to be of the same order of magnitude.

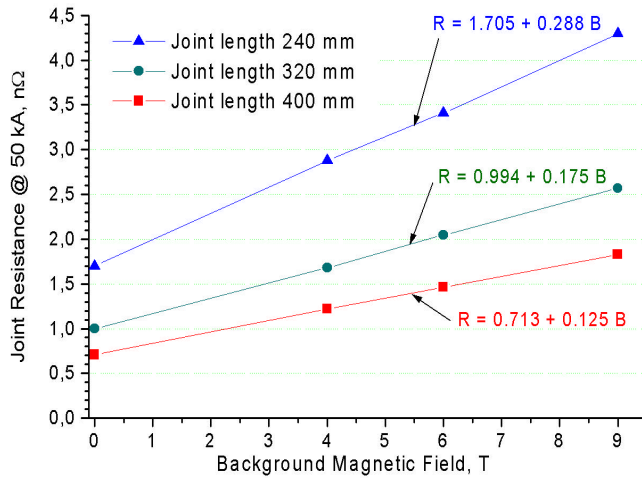


**Fig. 2.4.10** Joint resistance vs. background field for different joint lengths

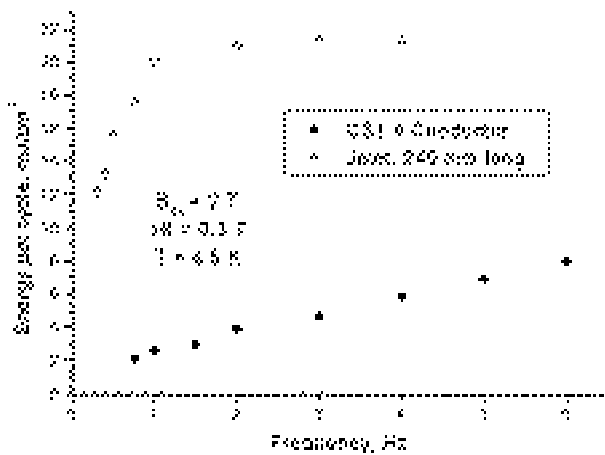


**Fig. 2.4.11** Comparison of conductor and joint losses at the same operating field. The normalization volume is strand + copper for joint and strand for conductor

A comparison of the joint and conductor stability is shown in Fig. 2.4.12 as a function of the temperature margin, defined as the difference between quench temperature and operating temperature. It may sound surprising that both conductor and joint data can be fitted approximately by the same line. However at 9Hz the joint AC loss is well in the screening range, while the conductor is fully penetrated; the loss ratio at 9Hz is much smaller than at low frequency. After chopping the joint, the stability was measured again at the same operating temperature. The stability remained constant from 400 to 320mm length and drops eventually after the second chopping, due to the strong current imbalance.

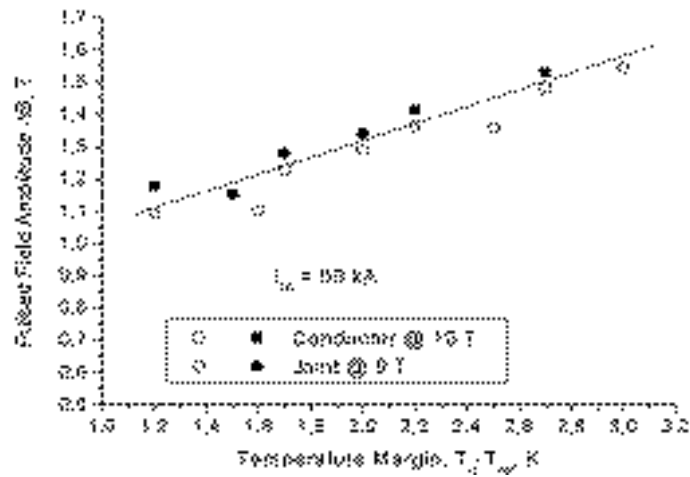


**Fig. 2.4.12** Comparison of joint and plain conductor stability under a transverse pulsed field

### 2.4.3 Preparation of the SeCRETS experiment

The "SEgregated Copper Ratio Experiment on Transient Stability" is a task devoted to the investigation of the role of the segregated copper in the transient stability behaviour of Nb<sub>3</sub>Sn cable-in-conduit conductors. A winding sample was prepared using two conductors with identical partial cross sections, only differing for the distribution of the copper stabiliser: either fully included in the Nb<sub>3</sub>Sn strands (right in Fig. 2.4.13) or partly segregated as bundled copper wires (left).

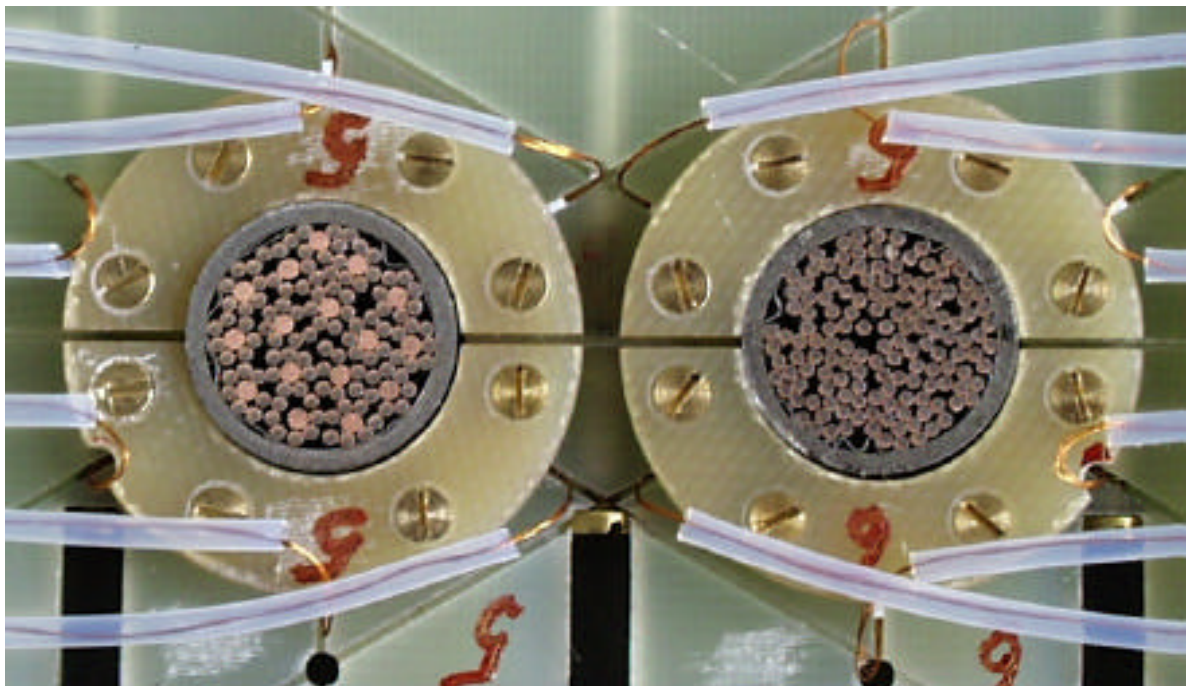


**Fig. 2.4.13** SeCRETS conductors with Hall sensors for current distribution measurements

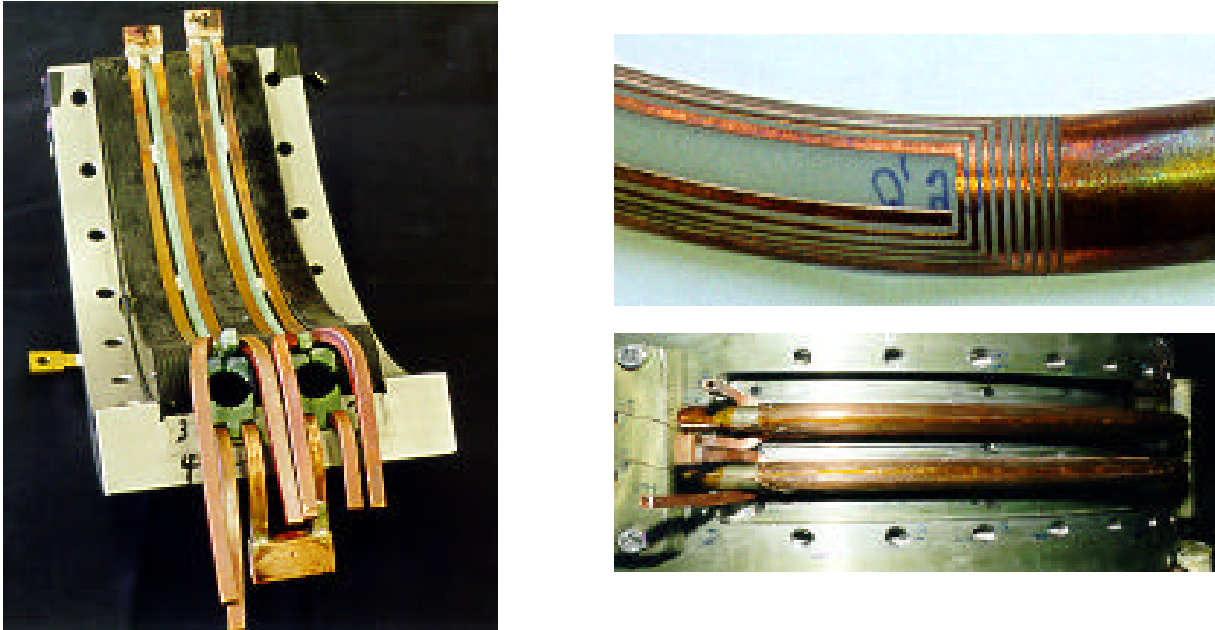


**Fig. 2.4.14(a)** *The pulsed field coils potted in the steel clamp, left, and the pick-up coils as detail and attached to the conductors*

After winding the SeCRETS sample and heat treatment, the joint, termination and instrumentation were completed. A set of transverse pulsed field coils for the stability test were attached to a steel clamp, Fig. 2.4.14(a), and bolted to the main cylinder after heat treatment. To detect the magnetisation under pulsed field, the conductors are surrounded by saddle shaped pick-up coils, manufactured by high precision machining a copper plated glass-epoxy shell, illustrated in Fig. 2.4.14(a), right. The instrumentation includes 14 sensors for in-flow temperature measurements, 58 miniature Hall sensors and 26 voltage tap pairs. A main heater, before the He inlet, and four smaller heaters, glued to the individual conductors are used to adjust the operating temperature, Fig. 2.4.14(b).

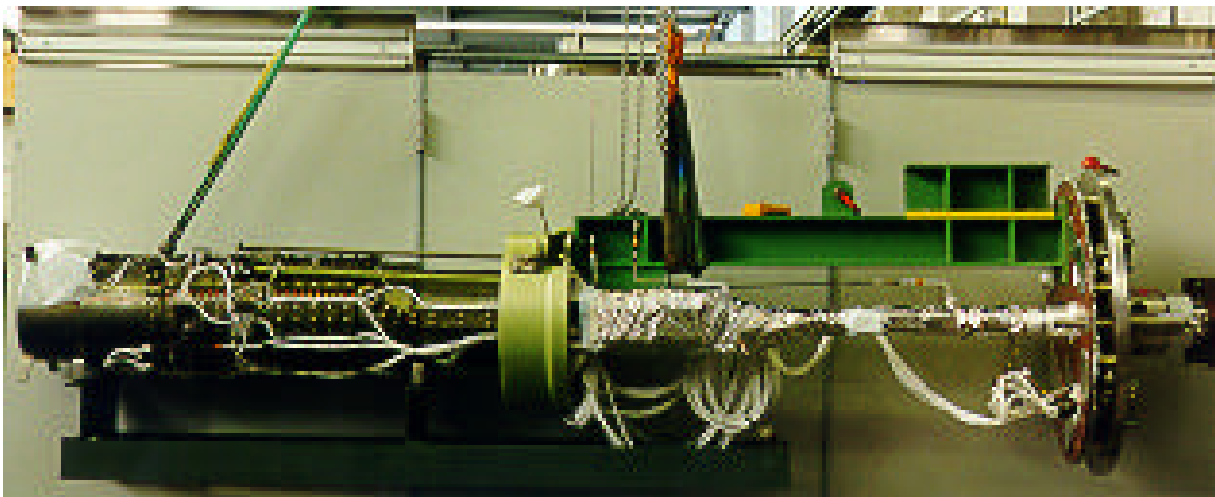


**Fig. 2.4.14(b)** *The winding with current leads and flange, ready for insertion in SULTAN*

#### 2.4.4 HTSC Current Lead

In the frame of the European Fusion Technology Programme, an international co-operation started between CRPP-FT and Forschungszentrum Karlsruhe (FZK) in 1996. The main goal of the task is the design of a 60kA binary current lead using High  $T_c$  Superconductors (HTSC) for further use in the ITER Toroidal Field Coils. The project was divided into three sub-tasks. The first one comprised testing several different HTSC modules at CRPP-FT in 1995/1996. The aim was to find the most suitable candidate for the application. As a result of the larger safety margin, reinforced Bi-2223 tape was chosen for the second step of the development programme, namely the test of a 10kA binary current lead at CRPP-FT. For that purpose a new test cryostat had to be constructed during 1997/1998. Due to some specification problems with the first module, the supplier had to deliver a second one and measurements were finally started at the beginning of 1999.

The module, Fig. 2.4.15, is based on AgAu stabilised Bi-2223 tapes. It consists of a total of seven stacks, each composed of an appropriate number of together sintered tapes. The stacks are positioned between a stainless steel supporting tube of special geometry and a surrounding stainless steel tube. The space between the two tubes is fully soldered. At the cold and warm ends, special copper end caps are placed as the interface to the normal conducting heat exchanger at the warm end, or the copper adapter of the low temperature short cut to the second current lead. The total number of superconducting wires is chosen so as to have a critical current of at least 12kA at 70°K. The total length of a module is 60cm. Four temperature sensors attached at 100%, 90%, 70%, and 50% of the length to provide the temperature distribution. Four of the stacks are equipped with voltage taps for current imbalance measurements and to enable power shut down detection in case of transient measurements.

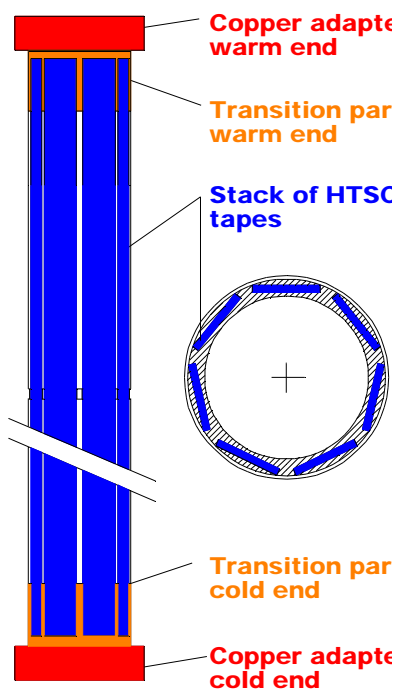


**Fig. 2.4.15** Longitudinal and cross sectional view of the 10kA HTSC module. Cold and warm end caps are also shown.

The test programme consisted of steady state as well as transient measurements. The 4.5°K heat load of the current lead is one of the most important properties. We can distinguish between the conduction heat load and the one generated by the low temperature contacts. The conduction heat losses for both leads were measured to be 1.46W and 1.57W respectively. The low temperature contact heat load was about 0.22W at 7.7kA and 0.53W at 10kA. Taking into account the refrigerator power consumption it was concluded that the current leads tested need about 30% of the value a conventional current lead requires.

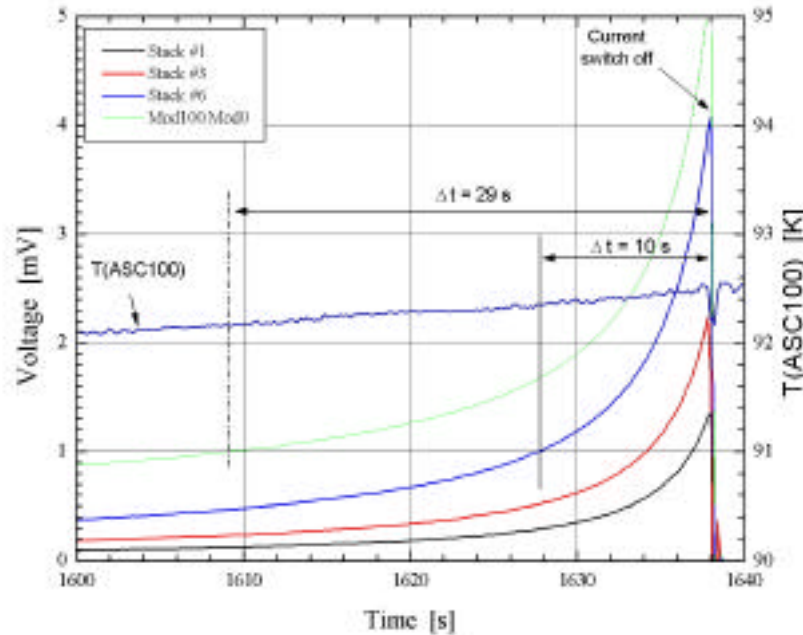


**Fig. 2.4.16** Voltage along HTSC stacks and temperature vs. time.

Transient behaviour in the case of a sudden loss of coolant flow of the current lead plays an important role, Fig. 2.4.16. It took about 29s for the detection voltage to increase to the limit of 5mV. In total it took more than 70s between switching off the coolant and power supply shut down, indicating a high safety margin with respect to the ITER requirement. At present a 20kA current lead composed of the two 10kA modules is being manufactured at FZK. As an alternative to the Bi-2223 tape modules, reinforced melt cast processed Bi-2212 tubes will be investigated at CRPP-FT during 2000. The superconducting part of the 10kA current lead will consist of two 5kA tubes operated in parallel. Beside steady state measurements the major focus will be directed towards the transient behaviour of the AuAg coated modules.

#### **2.4.5 Neon gas-cooled superconducting prototype cable for power transmission\***

Power transmission lines are one of the most promising applications of high temperature superconductors. The use of superconducting cables would allow the

\* The work described under this Section was not performed within the frame of the Association Euratom - Confédération Suisse.

enhancement of the power transmitted. Furthermore, the transmission losses and the cable cross-sections could be reduced. Therefore an increase of the transmitted power can be achieved using the existing underground infrastructure of existing conventional cables, an important economical aspect especially in large urban areas.

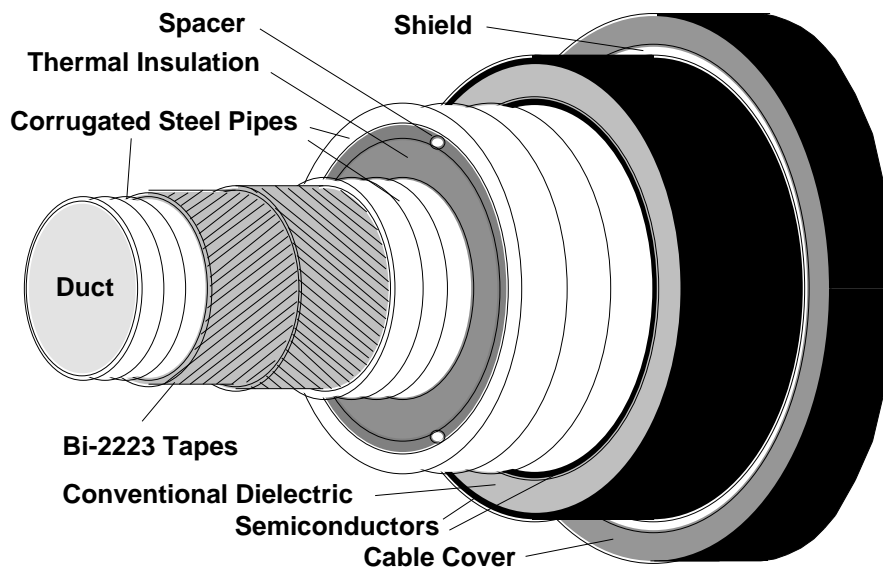
In collaboration with an industrial partner a 5m long, single-phase, superconducting prototype power cable has been constructed and tested. Design studies indicate that for a Bi-2223 based power cable with warm dielectric the optimum operating temperature, with respect to both the transmission losses and the investment costs, is close to 60°K. For the first time a neon refrigerator has been used to operate a superconducting cable between 50 and 70°K.

Figure 2.4.17 shows a sketch of a superconducting single-phase cable with warm dielectric. The main design parameters for the 5m long prototype cable are listed in Table 2.4.1. To avoid the degradation of the brittle oxide superconductor, the winding was carried out in a laboratory cabling unit allowing us to wind all 40 AgMg/Bi-2223 tapes of one layer simultaneously. Figure 2.4.18 shows the cabling process and the finished phase conductor prior to installation in the test assembly.

The cryogenic system is schematically illustrated in Fig. 2.4.19. The cool-down time to reach cable temperatures in the range of 50-70°K is about 3h. The heat leak through the thermal insulation has been found to be 0.6W/m. Figure 2.4.20 shows the cable test set-up with the Ne refrigerator and the operating panel for the cryogenic system in the centre.

Superconductor	2×40 AgMg/Bi-2223 Tapes
Tape Dimensions	3.6×0.25mm <sup>2</sup>
Critical Current (77K, B = 0, 1μV/cm)	30A
Cable Former Diameter	53mm
Outer Cable Diameter	158mm
Peak Current/Line Voltage/Power	2.5kA/110kV/112.5MW
Operating Temperature	60K

**Table 2.4.1** Main design parameters of the 5m long single-phase prototype cable.



**Fig. 2.4.17** *Sketch of a superconducting single-phase cable with warm dielectric. Evacuated superinsulator has to be used to ensure a sufficiently small heat leak of less than 1W/m.*



**Fig. 2.4.18** *Winding of the inner layer onto the flexible steel pipe wrapped with glass-fibre tape (left) and the finished phase conductor prior to installation in the test assembly (right).*

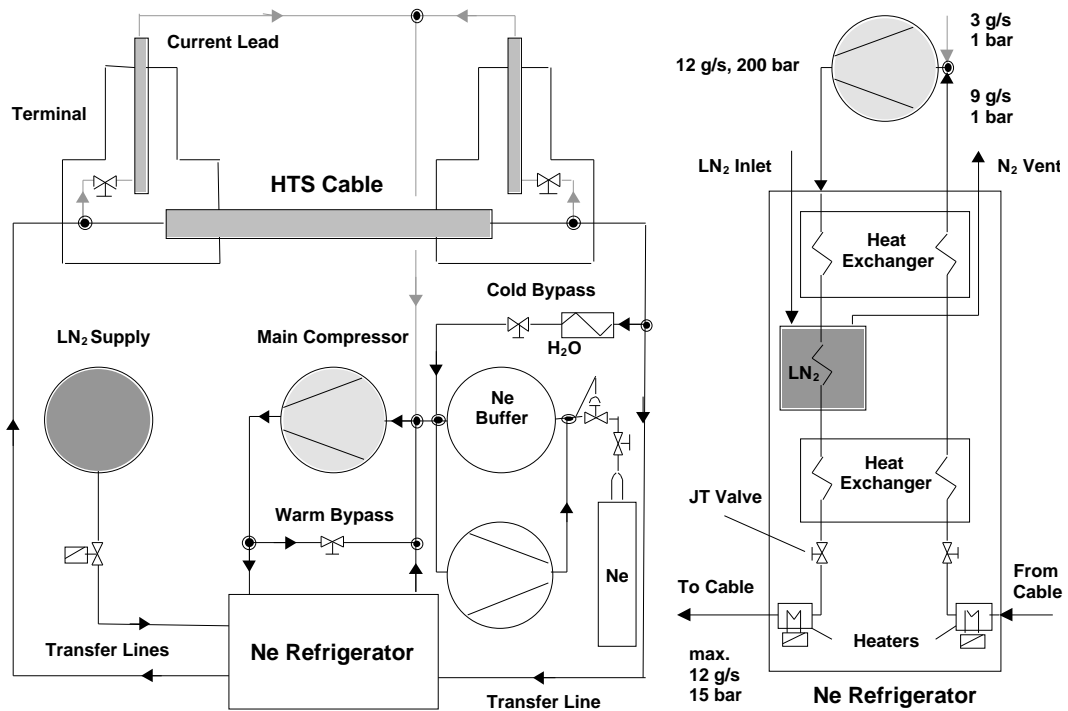


**Fig. 2.4.19** *Sketch of the cryogenic system. The Ne refrigerator consists mainly of 2 Ne-Ne counter-flow heat exchangers and a Ne-LN<sub>2</sub> heat exchanger*

***as pre-cooler. A Joule-Thomson throttle valve reduces the pressure of the pre-cooled Ne from 200bar to 5-10bar in the cable lowering the gas temperature to a minimum of 32°K. The high-pressure gas is supplied by an air-cooled, oil-free Sulzer-Burckhardt compressor.***

The major results are that a 5m long superconducting prototype cable has been fabricated without substantial degradation of the critical current of the AgMg/Bi-2223 tapes. A neon refrigerator developed by the CRPP provided operating temperatures in the range of 32 to 70°K. At 52°K a cable critical current of 4.9kA was reached [ $3 \times I_c(77^\circ\text{K})$ ]. In agreement with the design studies, the AC losses are inversely proportional to the critical current. Thus, the AC losses at 52°K are smaller by a factor of 3 than at 77°K. The 50Hz AC losses at the nominal peak current of 2.5kA are as low as  $0.31 \pm 0.02 \text{W/m}$  at 60K. Based on the test results a 50% reduction of the transmission losses can be expected compared with a conventional cable with a  $2000 \text{mm}^2$  copper cross-section at a line voltage of 110kV. An economical study performed as a part of this project suggests that superconducting power cables could become economically attractive in the mid term.

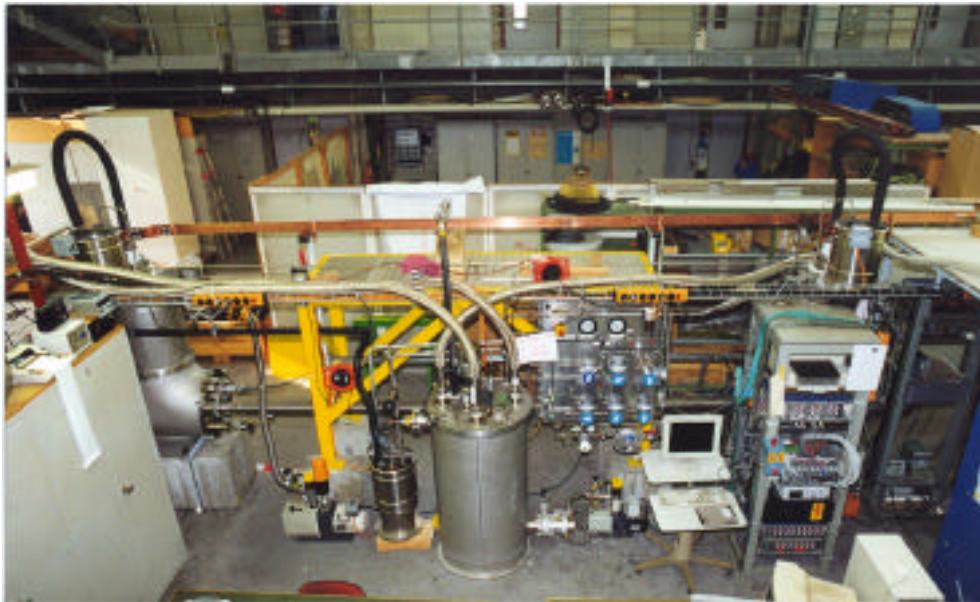


***Fig. 2.4.20 Photo of the cable test set-up.***

Figure 2.4.21 shows the cable critical currents ( $0.1 \mu\text{V/cm}$  voltage gradient criterion) as a function of temperature. The critical current of a 1m long pre-prototype cable measured at 77°K is also included. Figure 2.4.22 shows the AC losses in the superconductor measured by the electrical method as a function of temperature. These are proportional to the third power of the transport current and inversely proportional to the critical current.

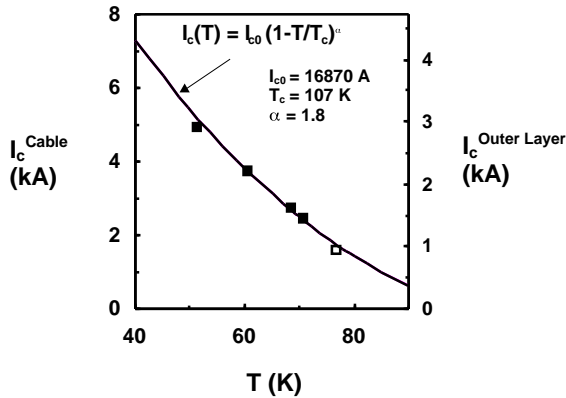


**Fig. 2.4.21** Cable critical current versus temperature. The measurements revealed that only 41% of the current flows in the inner layer. The critical current at 52°K is by a factor of 3 larger than at 77°K and reaches a value of 4.9kA (0.1 $\mu$ V/cm criterion).

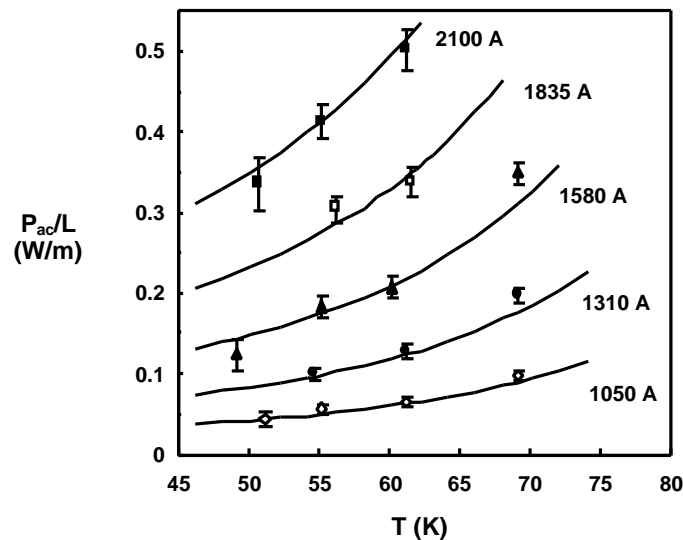


**Fig. 2.4.22** 50Hz AC losses in the superconductor versus temperature for selected values of the AC current rms.

## 2.5 Development of a 140GHz gyrotron for the Wendelstein 7-X stellarator

The Association Euratom-IPP Garching will construct and operate a new large experimental facility for nuclear fusion research, the W7-X stellarator. Among other important specific objectives, this stellarator aims at the demonstration of continuous plasma operation at fusion relevant parameters. A powerful steady-state heating system is therefore a key component of the device. ECH heating with a total power of 10MW in continuous wave (CW) operation at a frequency of 140GHz is foreseen as the main heating system. This RF power will be generated by 10 gyrotrons delivering 1MW each.

In the present state of the art of gyrotron research, 1MW RF power in CW operation at this frequency is very challenging, with the CW aspect being the most difficult one. The development of a prototype gyrotron fulfilling the above mentioned parameters, is being undertaken in a joint collaboration between CRPP, Forschungszentrum Karlsruhe (FZK) in collaboration with IPP Garching and an

industrial partner, Thomson Tubes Electroniques. The design phase started in May 1998 and a first prototype has been constructed and was delivered to FZK in October 1999. First experimental tests are planned to start at FZK in June 2000.

The operating parameters of this gyrotron are listed in Table 2.5.1 and a picture of the constructed gyrotron is shown in Fig. 2.5.1.

<b>Parameter</b>	<b>Design</b>
Frequency	140GHz
Output power in Gaussian Mode	1MW
Losses:	
converter	5%
non-Gaussian output	2%
cryogenic window system	1%
ohmic (cavity+launcher)	6.4%
total	<15%
Cavity output power without losses	1.2MW
Pulse length	CW (1000s)
Cavity mode	TE <sub>28,8</sub>
Cathode voltage	80kV
Depressed collector voltage (collector at ground)	26kV
Beam current	40A
Total system efficiency ( $P_{HE11}/P_{ebeam}$ )	50%
Maximum wall loading	2.0kW/cm <sup>2</sup>
Monomode operation possible	yes

**Table 2.5.1**      *Design parameters of the 1MW/140 GHz CW gyrotron*

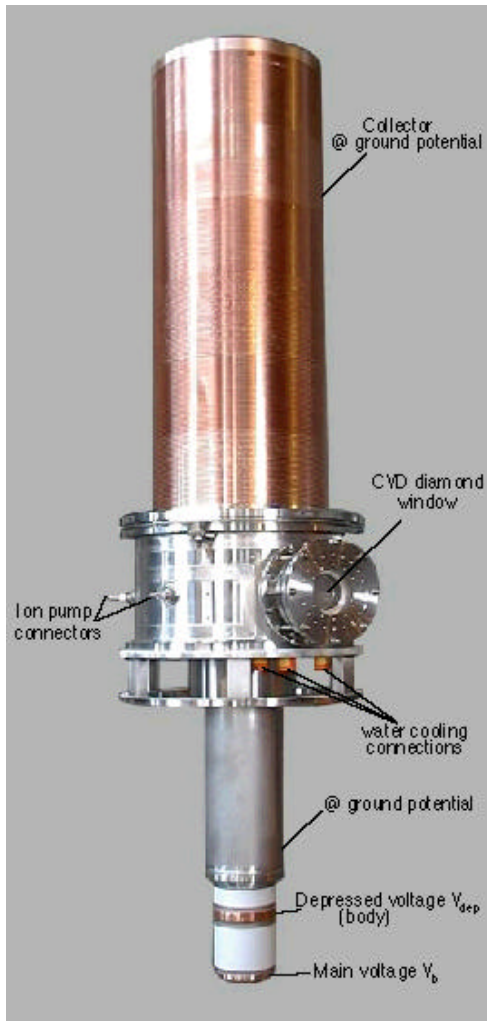


**Fig. 2.5.1**      **Picture of the 140GHz gyrotron**

## **2.6**      **Industrial process plasmas\***

### **2.6.1**      **Deposition of amorphous and microcrystalline silicon for thin-film solar cell application**

Production of microcrystalline silicon requires the deposition of hydrogenated silicon and, at the same time, a mechanism for converting, or 'conditioning', the film into a microcrystalline phase. There are several 'conditioning' mechanisms, but essentially it entails the removal of energetically-unfavourable Si:H groups by an etchant species. In plasmas of silane/hydrogen mixtures, this etchant species is atomic hydrogen. Generally, the silane is completely depleted in the plasma, and the overall deposition process is rate-limited by the generation of atomic hydrogen. Rapid deposition of microcrystalline silicon has been optimised for high power, very high frequency (VHF) plasmas in hydrogen-diluted silane. The deposition rate could be further improved by using a higher silane flow-rate provided that the supply

---

\* The work described under this section was not performed within the frame of the Association Euratom - Confédération Suisse.

and/or etching efficiency of the etchant species could be simultaneously increased. This could be achieved in two different ways :

- Use an alternative plasma chemistry to the standard silane/hydrogen mixture by adding gases containing a more effective etchant species. Atomic fluorine is known to be a strong etchant for silicon, but fluorine gas is extremely corrosive and special precautions must be used. Silicon tetrafluoride ( $\text{SiF}_4$ ) was chosen as a suitable fluorine-containing additive to silane/hydrogen for this work, Fig. 2.6.1.
- Use an alternative plasma source with a more efficient production of atomic hydrogen, while keeping the standard silane/hydrogen mixture. The high current DC arc at CRPP is known to be a prolific source of atomic hydrogen, and this reactor was converted for silicon deposition experiments.

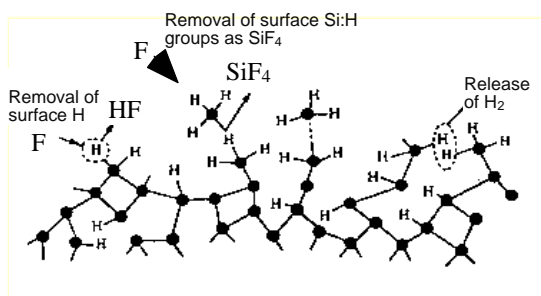


**Fig. 2.6.1 Fluorine etching on amorphous silicon**

### Alternative plasma chemistry for microcrystalline silicon deposition

The potential of  $\text{SiF}_4$  for accelerating microcrystalline silicon deposition has been investigated in our Balzers KAI-1 Plasma-Box industrial reactor (57cm x 47cm), at the VHF frequency of 70MHz as a function of pressure, power, flow-rate and concentration in silane/hydrogen mixtures. The excitation frequency of 70MHz was chosen as a compromise between high deposition rate and voltage non-uniformity at high frequencies. With a central RF feed, a uniform gas showerhead and single side pumping, a film thickness uniformity of better than 5% was obtained. Typical plasma parameters used during this study were, 400W power, 0.05 to 4mbar total pressure, 250°C electrode temperature with 24mm electrode gap, and gas mixtures of silane, hydrogen, silicon tetrafluoride and argon whereby the individual gases, binary mixtures and final triple mixture were systematically investigated.

**Silicon tetrafluoride plasma** was found to deposit very slowly ( $0.1\text{\AA}/\text{s}$ ) on amorphous hydrogenated silicon (a-Si:H), but rapidly etch ( $3\text{\AA}/\text{s}$ ) fluorinated silicon (a-Si:F:H). There is therefore a strong substrate dependence for  $\text{SiF}_4$  plasma, which further complicates the issue by increasing the number of unknown parameters. The deposition rate of silane, for the same plasma conditions, is 60 times faster than for  $\text{SiF}_4$ . Therefore we have an indication, which will be supported and explained below, that  $\text{SiF}_4$  contributes only inefficiently to deposition.

**Silicon tetrafluoride / silane plasma** deposits rapidly ( $6\text{\AA}/\text{s}$ ), but only amorphous material. Strong powder formation also occurred, probably because both gases are electronegative gases which give rise to trapped negative ions.

**Silicon tetrafluoride / hydrogen plasma** gave little or no deposition. There is negligible conversion of the  $\text{SiF}_4$  to  $\text{SiH}_x$ -type precursors. We deduce that deposition originates from silane only, and that if  $\text{SiF}_4$  dissociation products do deposit, they are efficiently removed by other  $\text{SiFx}_4$  radicals. These observations can be understood by considering the order of bond dissociation enthalpies :



This shows that silane is preferentially dissociated in silane / silicon tetrafluoride mixtures, that hydrogen cannot spontaneously replace fluorine in  $\text{SiF}_x$  radicals, and that  $\text{SiF}_4$  and HF are stable etch products.

**Silicon tetrafluoride / silane / hydrogen plasma** was investigated to find the most rapid deposition of microcrystalline silicon given a constraint on RF power density. Different pressure, concentration and flow-rate scans confirmed that the deposition rate was fixed by the silane flow-rate, independently of the other gases, provided that 100% silane depletion prevailed. Therefore the goal was to increase the silane flow-rate until microcrystalline silicon could no longer be obtained.

Microcrystalline silicon films were obtained using plasmas in silane / hydrogen /  $\text{SiF}_4$  mixtures with flow-rate ratio approximately 1:10:10, Fig. 2.6.2. The deposition rate limit was reached for  $3\text{\AA}/\text{s}$ , which was less than twice as fast as silane / hydrogen mixtures without silicon tetrafluoride. For certain plasma conditions, amorphous silicon deposition obtained using a silane / hydrogen mixture could be transformed to microcrystalline deposition by the admixture of  $\text{SiF}_4$ . However, the net deposition rate was not greatly improved at these moderate powers ( $<1\text{kW}$ ). One interpretation is that the high bond energy of  $\text{SiF}_4$ , in comparison with that of silane and hydrogen, limits the dissociation of  $\text{SiF}_4$  in the plasma, thus limiting the etchant supply rate.

In conclusion, the strong bond energy of silicon tetrafluoride means that it is not a sufficiently effective source of atomic fluorine etchant for microcrystalline silicon deposition. A more appropriate plasma chemistry would be fluorine, silane and hydrogen since then the atomic fluorine etchant would be in ample supply; the deposition rate could then be increased by adding more silane whilst remaining microcrystalline. This and other possible plasma chemistries are currently under investigation.

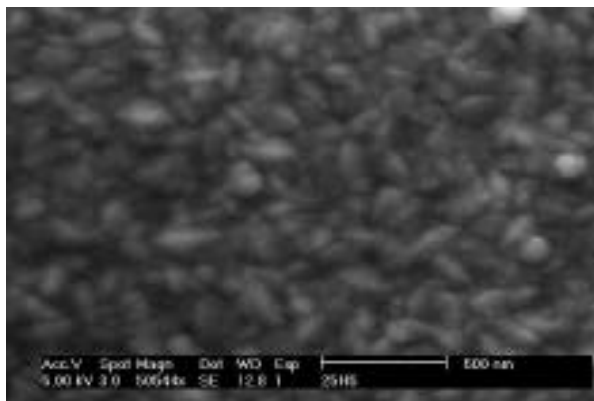


**Fig. 2.6.2** *Electron microscopy of the best microcrystalline sample, showing 10nm pyramidal structures*

### **Alternative plasma source for microcrystalline silicon deposition**

The High Current DC Arc has been used to deposit microcrystalline silicon at extraordinarily high rates, up to  $100\text{\AA}/\text{s}$ . Only microcrystalline silicon is ever produced, with no observable amorphous component. The deposition reactor is a Balzers BAI 450D originally developed for diamond coating processes, Fig. 2.6.3. The configuration resembles the 'hot wire' device where radicals formed at a hot wire diffuse to the substrate, except that the tungsten filament is replaced by a plasma column. Advantages of this plasma over the hot wire technique are the absence of tungsten contamination and higher temperature and radical density. Furthermore, the reactor is robust and has the possibility for scaling-up to large area deposition.

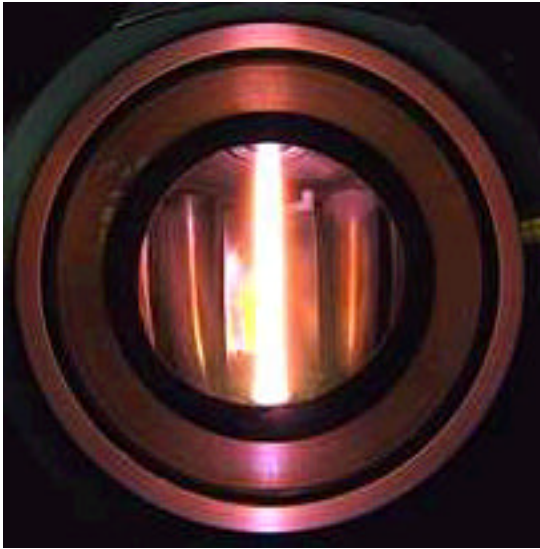


*Fig. 2.6.3 View into the high DC current plasma reactor*

Even at these extremely high deposition rates, the film is highly crystallised, with a mean crystallite size of  $12\pm 3\text{nm}$ , Fig. 2.6.4, and there is no observable transition from amorphous to microcrystalline at the substrate surface, in contrast with other deposition methods. The hydrogen content is approximately 5%. Film adhesion is excellent, even for a thickness of several microns, with none of the peeling often found for RF deposition using substrates which were not carefully cleaned beforehand.

The arc is known to be an efficient source of atomic hydrogen, H, which is undoubtedly the etchant species in this silane / hydrogen / argon plasma. It is likely that this relatively high efficiency of H production is the reason for such a great difference between the RF and DC arc methods. Several explanations can be proposed for this difference: i) the loss of H by recombination on surfaces is greater in RF parallel plate reactors where the surface-to-volume ratio is larger than in the DC reactor; ii) the elevated gas temperature in the DC reactor is a reservoir of thermal energy which supports the stepwise increase in vibrational energy of hydrogen molecules, leading to efficient dissociation, whereas RF reactors operate near ambient gas temperatures; and iii) Penning dissociation via argon metastables will occur in the DC arc reactor.

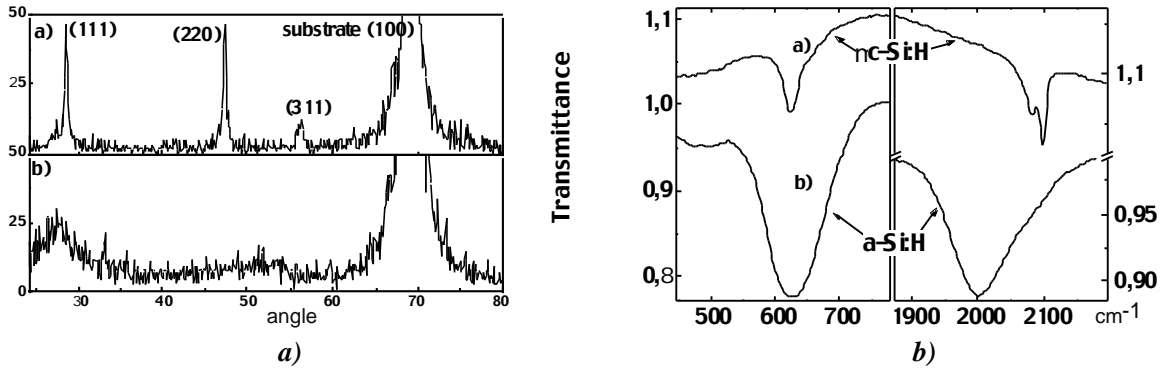


**Fig. 2.6.4** a) X-ray diffraction for: a) Silicon deposited by using DC arc ; b) PECVD amorphous silicon  
 b) Infrared transmission for: a) Silicon using DC arc ; b) PECVD amorphous silicon

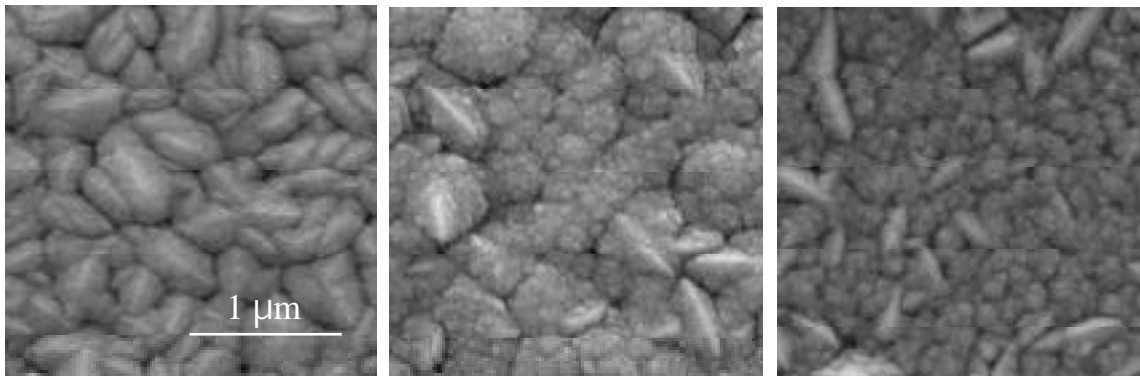


**Fig. 2.6.5** Electron microscopy of film surfaces obtained at distances of 7, 13 and 16cm from the arc axis

The surface morphology can be influenced by placing the substrate at different distances from the arc column as shown in the electron microscopy images in Fig. 2.6.5. The material quality, tested at IMT Neuchâtel, suffers from a rather high defect density, but it must be stressed that these were preliminary tests with no special attention paid to contamination or impurities. Also, post-hydrogenisation could potentially passivate defects. This new deposition technique has now been patented (CH/794/99).

### 2.6.2 Cubic boron nitride deposition

Cubic boron nitride is an important material with outstanding material properties comparable to diamond. Cubic boron nitride films would be of great interest for coatings of cutting and forming tools, in particular for conditions where diamond is not at all applicable. However the deposition of **adherent, pure cubic boron nitride** layers is still in its developmental phase and at present no industrial process exists at all. Cubic boron nitride (c-BN) is an important technological material with thermal, electrical, and mechanical properties close to diamond. In addition c-BN has greater chemical stability with respect to diamond in the presence of oxygen,

iron and nickel at high temperatures. This difference with respect to diamond makes c-BN an ideal material for machining ferrous materials.

Due to its outstanding tribological properties, diamond coating deposition has been studied in collaboration with Balzers AG in the frame of the Priority Program on Materials (PPM). Coatings of tools with interesting tribological properties such as high hardness, chemical stability, low abrasive coefficient are of great interest for industrial applications. Increasing the lifetime of manufacturing tools, subject to extreme requirements with respect to thermo-chemical stability, hardness and fracture (such as cutting or forming tools, artificial thighbone head) by a protective coating saves money, time and protects the environment by dry machining. A new plasma CVD technique of diamond deposition enabling large scale cost-effective coating is being developed.

In the frame of the present project, a high current DC arc reactor similar to the commercial Balzers BAI 730 reactor used for the industrial deposition of diamond, has been adapted to study the deposition of boron nitride, whose cubic phase is similar to the diamond.

The radicals necessary for the deposition were created in a hot arc plasma column produced by a large current (typically 140A) and diffuse out of the plasma. The substrates to be coated were placed in this diffusion region concentric around the plasma column. The basics of the high current DC arc reactor (HCDCA) are similar to the well-known hot wire reactor. The advantages of the high current DC arc reactor are the same as for silicon deposition discussed already.

The basic feature of the reactor is a non self-sustained arc discharge created between an anode and a cathode 40cm apart. Electrons emitted from polarised, hot tungsten filaments sustain a low working pressure, DC discharge with a current up to 340A at a driving voltage of about 50-90V. The typical working pressure is around 1-2mbar. Beside argon, different gases such as hydrogen, nitrogen could be used. A full safety system also allowed the used of highly toxic and corrosive gases such as diborane, silane and ammonia. The gas fluxes depend on the gas but are typically of the order of 1000-2000sccm. Two magnetic field coils in Helmholtz arrangement (0-250G) confine and stabilise the 5cm $\emptyset$  arc plasma column, Fig. 2.6.6. The substrates are concentrically positioned around the arc plasma and are heated up to several 100°C mainly due to the recombination of atomic hydrogen produced by the arc plasma. Measurements performed in the plasma show that the electron temperature is around 2eV (23'000°K). The electron density in the arc column is also very high, in the range of 10<sup>12</sup>-10<sup>13</sup>cm<sup>-3</sup>, measured by electrical probes. The plasma produced in the high current DC arc reactor is a typical plasma out of thermal equilibrium. Line broadening measurements and comparison between calculated and measured molecular bands (N<sub>2</sub><sup>+</sup>) allowed the determination of the gas temperatures, in the range of about 5000°K for the most prominent discharge parameters.

The substrates located in the diffusion zone are mainly heated due to atomic species recombining on its surface. The deposition temperature, varying from 300 to 900°C according to the films deposited, in the absence of external heating or cooling is determined by the substrate position, the arc power and the injected gas mixture and flux.

A 13.56MHz RF generator connected to the insulated substrate holder allowed DC biasing of the samples if necessary. For some experiments investigating the boron plasma chemistry also a conventional capacitively coupled RF reactor (13.56MHz, 40W) has been used.

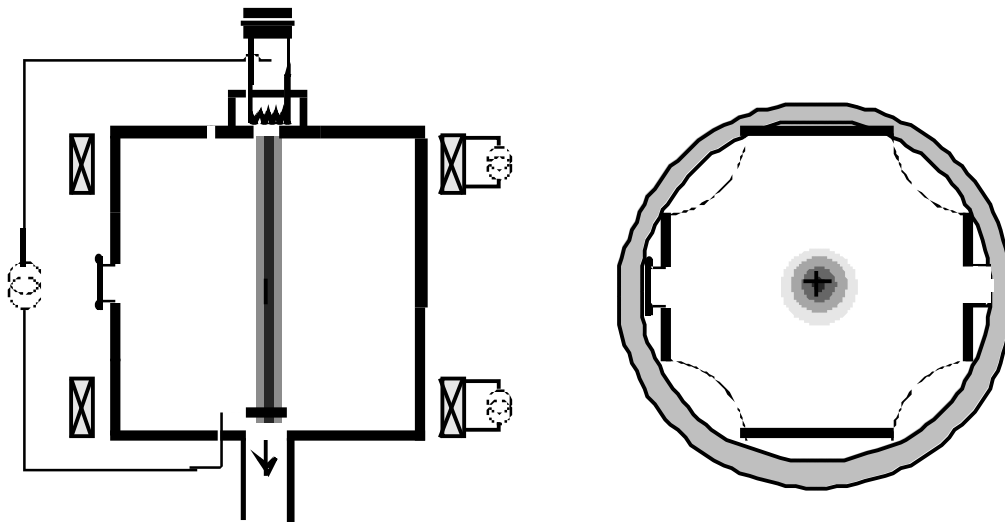


**Fig. 2.6.6** *Schematic of the DC reactor and its cross-section. 1) reactor, 2) heated filaments, 3) ionisation chamber, 4) DC supply, 5) anode, 6) magnetic field coils, 7) plasma column.*

For the deposition of boron nitride films, different precursors were used and wide plasma and reactor parameter ranges were investigated. The extreme difficulties of synthesising cubic boron nitride films by CVD did not allow stabilising the cubic phase in this reactor. Most of the coatings resulted in hexagonal or amorphous boron nitride with a chemical composition close to stoichiometric. Negative biasing of the samples to increase the positive ion bombardment, commonly used to stabilise the cubic phases, did not work in this reactor and only a densification of the films was observed. The lack of cubic boron nitride deposition in the high current DC arc might be attributed to the absence of ion bombardment, a factor known to play an important role in the stabilisation of the cubic phase. Studies of the deposition of boron nitride films were carried out with different precursor gases, such as nitrogen, ammonia and diborane. Process parameters were varied, including gas composition, diborane/nitrogen or ammonia, gas pressure, monomer gas fluxes, discharge current and magnetic field. In all the ranges of deposition parameters scanned, it was impossible to deposit plasma reactor films in the HCDCA with interesting tribological properties. Most of the films obtained were mainly  $sp^2$  bonded (hexagonal or amorphous phase), whereas the desired hard cubic boron nitride phase is  $sp^3$  bonded. ESCA measurements showed that in most of the coatings analysed the necessary 1:1 stoichiometry for boron nitride was obtained, but in general only little  $sp^3$  bonding was found in these layers. From these experiments it can be concluded that the deposition of cubic boron nitride needs sufficient ion bombardment.

Even the direct exposure of samples to the hot arc plasma did not result in deposition of cubic boron nitride. The same conclusion can be drawn from biasing experiments of substrates located in the diffusion zone of the arc plasma. In this case the ion density in the radical diffusion zone is too small to favour the cubic phase transition. In order to influence the boron chemistry, solid boron-ammonia

was evaporated and was used as an alternative boron precursor with a pre-existing B-N bonding. With this monomer, no significant  $sp^3$  bonding in the coatings was found either. Additional experiments injecting solid boron nitride powder into the arc discharge led to no formation of cubic boron nitride.

The plasma chemistry of boron-containing species was studied by infrared absorption spectroscopy in a capacitively coupled radio frequency reactor and demonstrated the usefulness of this diagnostic for understanding the various unknown chemical reactions which occur in this kind of reactive plasma. The dissociation of diborane, the different reactions of the fragments and new species created in the gas phase, such as aminoborane, containing important boron-nitrogen bonding for deposition, reveals the rich chemistry in these reactive plasmas. The unknown plasma chemistry of boron nitride deposition was studied by infra-red absorption spectroscopy in an RF capacitively coupled reactor using a commercial FTIR spectrometer. This study illustrated the use of this diagnostic for determining the chemical reactions that take place in this kind of plasma. Mixing diborane with ammonia leads to the spontaneous creation of diammoniate in the gas phase, whereas in plasma only gaseous amino-borane is observed. When replacing ammonia with nitrogen, no B-N bond formation could be detected at all, even in the presence of plasma. This diagnostic led to a better understanding of the importance of the chemical reactions in the plasma borazine-boramine chemistry and may lead to a better understanding of the stabilisation of the hard phase of boron nitride. In the RF reactor used, only coatings with  $sp^2$  bonded boron nitride could be obtained.

### **2.6.3 Decorative coating**

A CTI (Commission pour la Technologie et l'Innovation) supported project including a Swiss watch industry partner, investigated the production of decorative coatings. Bulk zirconium oxide was nitrided by a high density current plasma giving yellow-golden zirconium nitride, whereas a metallic appearance was obtained by carburizing the white ceramic in the same plasma reactor. It was found that the plasma composition is crucial to obtain industrial nitriding of the ceramics. An  $N_2-H_2$  plasma does not lead to efficient nitriding of the substrate, whereas an  $NH_3$  plasma leads to the yellow-gold zirconium nitride which is a resistive material interesting for the jewellery and watch industry. Load effects from neighbourhood substrates and the substrate holder were found to give rise to inhomogeneity of the layer. This effect can be cured by a modified substrate holder and by optimised substrate arrangements.

The first scientific and industrial surface characterisation of these plasma treated zirconium ceramics has been made. X-ray diffraction confirmed the diffusion of nitrogen and the formation of zirconium nitride. X-photoelectron spectroscopy showed-up a 100nm deep gradient layer, in contradiction to the glow discharge optical emission spectroscopy which indicates a 5000nm thick layer with constant nitrogen concentration.

Measurements by transmission electron microscopy will be made to understand the depth concentration profile better, while the plasma-substrate interaction under different plasma conditions, in particular different plasma compositions, shall be carried out to clarify the dominant nitriding mechanism in the plasma.

### 2.6.4 Plasma spraying

Plasma spray coating is a well-established industrial technology which has achieved outstanding technological and commercial progress in the aeronautics, gas turbine, biomedical industries and others. In spite of this success, the underlying fundamentals are still poorly understood, in particular the behaviour of the arc inside the torch nozzle which experiences instabilities and restrike giving rise to "surging" and "whipping" motions of the plasma jet. This fluctuating behaviour may lead to a non-uniform heating of the injected powder and consequently adversely affects the quality and yield of the spray deposits.

The atmospheric pressure plasma torch investigated at the CRPP is a Sulzer Metco F4 without powder injection equipped with a 6mm $\varnothing$  atmospheric anode nozzle and a thoriated tungsten cathode fitted with either a straight or a swirl gas injector. Typical parameters are: 500A current, 15-80SLM (Standard Litre per Minute) of Ar and with 2-4SLM H<sub>2</sub>. The electrical power is up to 50kW with a torch efficiency between 30 and 60%. The gun is mounted on a 2-axis displacement table with the jet axis horizontal.

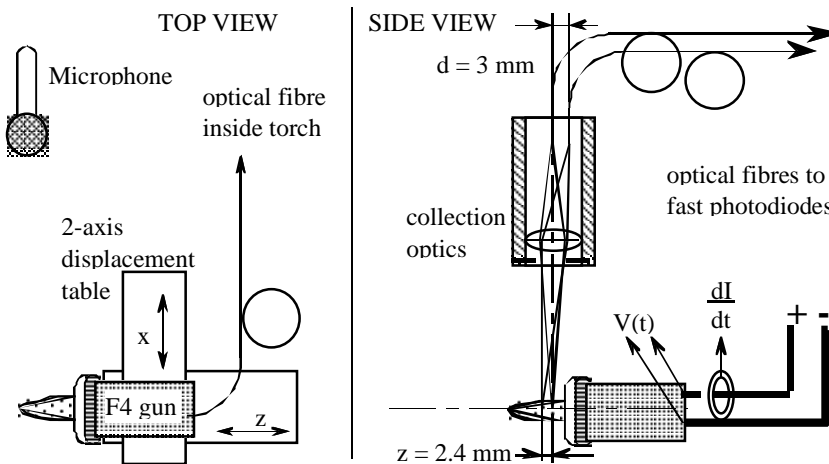


**Fig. 2.6.7** Top and side views of the experimental arrangement

The arc voltage is measured directly at the gun electrodes with a differential passive voltage probe. The time derivative of the torch current is measured with a Rogowskii coil. A microphone is positioned 1.2m from the jet axis. A lens positioned 435mm above the plasma jet, focuses the jet light emission onto two optical fibres with a spatial resolution of about 0.08mm. The fibres placed  $d$  apart along the torch axis collect light from two locations separated by  $z$  mm (see Fig. 2.6.7). This set-up is used for the estimation of the jet velocity by measuring the time of flight of light fluctuations as they propagate with the flow. The collected light is detected by fast Si-PIN photodiodes. In addition an optical fibre has been inserted inside the gun to collect the light emission directly from almost the whole arc length.

#### Time dependence of the fluctuating signals

Figure 2.6.8 shows a typical time dependence of the torch voltage and jet light emission on axis 1mm from the nozzle exit for two gas mixtures. The voltage

pattern for pure Ar operation exhibits fluctuations of weak amplitude and small time derivatives (around 120kV/s), which suggests that the arc experiences the so-called "take-over mode". In contrast the voltage signal for the H<sub>2</sub>/Ar mixture shows a clear sawtooth pattern, which is typical of the "restrike mode". There are two kinds of voltage drops: the large ones (between 20 and 30V, with up to 10MV/s) which might be attributed to the "upstream restrikes", for which a breakdown of the arc occurs with a new arc root closer to the cathode; and the small voltage drops (typically 5 to 15V at 1MV/s) which may originate either from "upstream restrikes" or from short circuiting of the curved part of the arc at the anode root. In the latter phenomenon, which resembles a reconnection, the anode root is maintained at the same position and the arc is not interrupted. This is shown for some of the small voltage drops in Fig. 2.6.8 by the absence of a subsequent reduction in the jet emission.

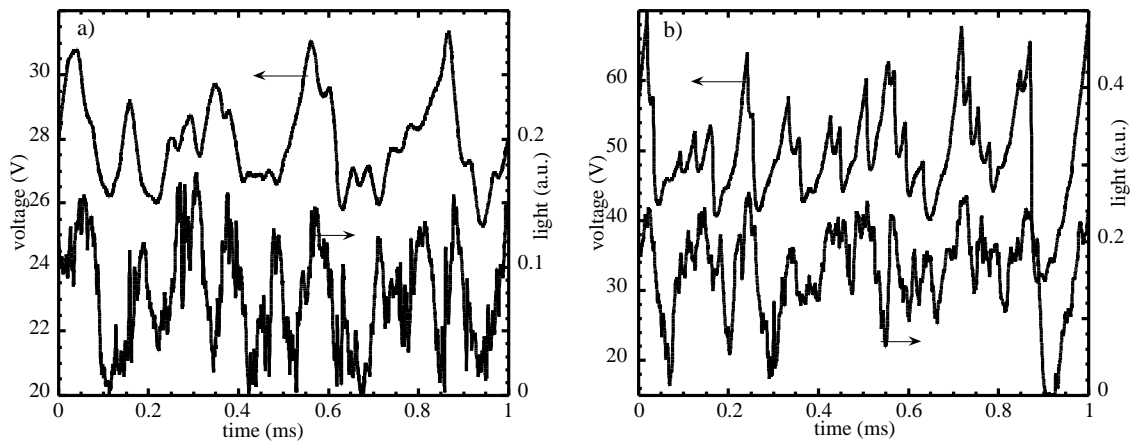


**Fig. 2.6.8** Typical time dependence of the torch voltage and light emission collected on the jet axis at 1mm from the nozzle exit for two gas mixtures: a) 50 SLM Ar and b) 4/50 SLM H<sub>2</sub>/Ar (500A, straight flow gas injector, sampling time 0.2 $\mu$ s).

The jet emission signals show strong fluctuations for both gas mixtures. This is because the plasma visible emissivity is a sensitive function of the local temperature variations in the jet (10-1500°K). The mean light intensity is nearly doubled by the addition of only 7% of H<sub>2</sub> to the plasma gas because the effective power coupled to the plasma jet increases from 6.8 to 14.4kW. The emission signals are clearly correlated with the voltage fluctuations, especially for the H<sub>2</sub>/Ar case. Systematic analysis of the voltage and light signals shows that the deepest voltage drops lead to the strongest reductions in the emission. It seems therefore that the upstream restrikes are responsible for the strongest temperature drops in the jet. Voltage and emission signals are shifted with an average delay of about 15 $\mu$ s corresponding to the transit time of the perturbations from the anode arc root to the detection point (about 24mm in our case which leads to an average velocity of nearly 1600m/s inside the nozzle).

Figure 2.6.9 shows the arc emission fluctuations measured *inside the torch* which exhibit much smaller amplitude variations than the plume emission, probably because of the absence of spatial resolution, and the fact that visible emission is less sensitive to temperature variations at the high arc temperatures (above 20'000°K). Moreover the arc emission signal closely follows the voltage fluctuations, as opposed to the jet emission signals which are distorted due to turbulence before

the nozzle exit. For the low Ar flow case (Fig. 2.6.9(a)) we observe regular, quasi-periodic fluctuations of the signals at about 4.3kHz with alternating small and large drops, whereas for the high Ar flow the fluctuations are much faster and less regular (Fig. 2.6.9(b)).

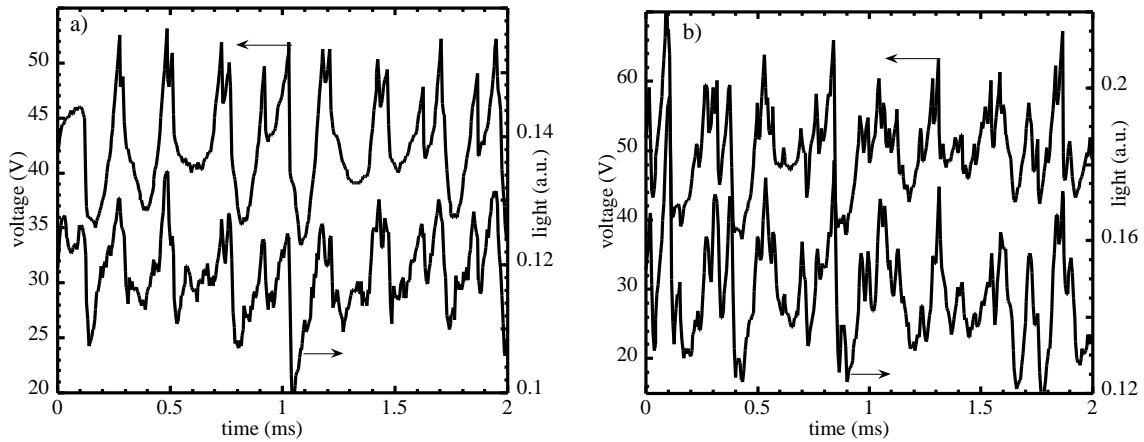


**Fig. 2.6.9** Typical time dependence of voltage and emission from *inside* the torch for two gas mixtures : a) 4/15 SLM and b) 4/50 SLM H<sub>2</sub>/Ar (500A, straight flow, sampling time 5µs).

Except for the current, the pure Ar case shows fewer fluctuations and no clearly defined frequencies in comparison with the H<sub>2</sub>/Ar mixture for which the power spectra of voltage, light and acoustics are dominated by high frequency peaks in the range 3-12kHz. These fluctuations are due to the arc motion and restrike, a quasi-periodic phenomenon. The amplitude and frequency of these peaks change with torch ageing due to electrode wear. On the other hand, the light emission power spectrum shows a significant continuous background level which increases at low frequencies. This is attributed to turbulence of the plasma jet and consequent entrainment of the surrounding air.

### Effect of gas injector geometry

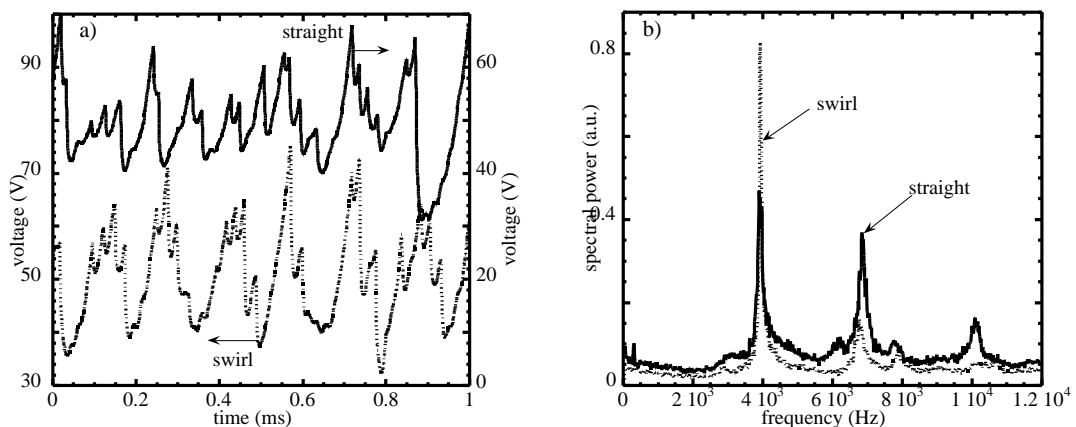


**Fig. 2.6.10** Time dependencies (a) and corresponding power spectra (b) of the voltage fluctuations for swirl (...) and straight (-) gas injection (4/50)

***SLM H<sub>2</sub>/Ar, 500A, 0.2μs sampling time, 12.2Hz frequency resolution).***

In Fig. 2.6.10 the time dependence and power spectrum of the voltage fluctuations are compared for swirl and straight gas injection. For swirl flow the voltage signal shows a similar behaviour to the low Ar flow case, with small fast fluctuations superimposed on regular larger fluctuations. This could be explained by the reduced gas axial velocity with the swirl injector (45° helical angle) and the consecutive reduction of the gas drag on the anode foot in the axial direction. The power spectrum shows the dominance of a characteristic frequency around 4kHz for the swirl flow, whereas multiple higher frequency components are present for the straight flow.

### **Velocity estimation by TOF of light fluctuations**

The time of flight (TOF) technique has been used to estimate velocity profiles in the hottest regions of the plasma jet. The technique is based on the assumption of convective transport of emission fluctuations with the axial velocity of the jet. The TOF of these successive hot/cold puffs is measured by the cross-correlation of the emission signals collected by two optical fibres (Fig. 2.6.7). The velocity is obtained from the ratio of the flight distance to the time shift of the cross-correlation maximum. A better cross-correlation is obtained if the signals are bandpass-filtered in the frequency range related to the arc movements and restrike (3-12kHz). Figure 2.6.11 shows a radial velocity profile obtained between 1 and 3.4mm from the nozzle exit for two plasma conditions. An addition of only 4% H<sub>2</sub> nearly doubles the velocity on axis. The velocity profile is peaked (3 mm FWHM for 6mm nozzle diameter) which has implications for the powder injection geometry in plasma spraying applications.

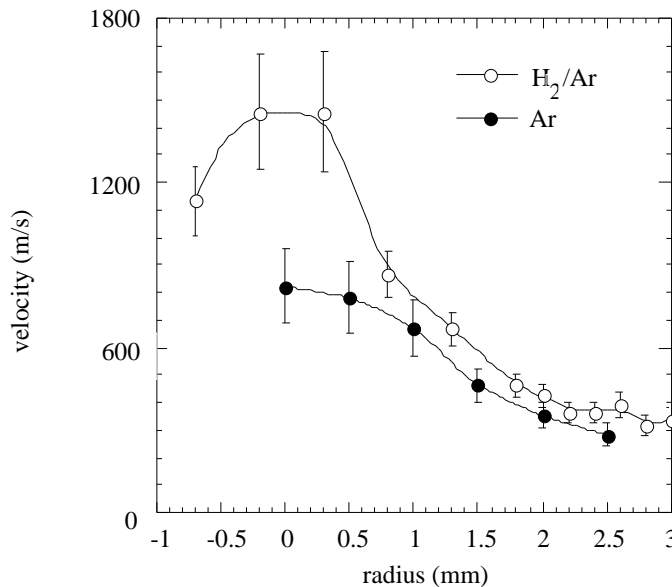


***Fig. 2.6.11 Plasma jet velocity profiles for two plasma condition (2/50 SLM H<sub>2</sub>/Ar (o) and 50 SLM Ar (•) at 500A, swirl injector)***

### **2.6.5 Powder production in reactive RF plasmas**

Powder or particles are found in deposition and in etching plasmas. However, the origin of these particles might be of quite different nature. Powder formation in plasmas used for film deposition in particular in diluted silane RF plasmas, have been intensively investigated during the last few years. The different features of powder formation such as the nature of the powder precursors and the agglomeration and accretion phases have been identified and investigated experimentally and theoretically.

Besides this very reactive plasma, many other plasma processes applied in industry show powder formation. In most cases, the powder formation leads to problems either in the quality of the film or with process interruptions due to prolonged maintenance and cleaning of the reactor. Hexamethyldisiloxane (HMDSO)/helium/oxygen plasmas are used for the deposition of silicon dioxide as a permeation barrier in the packing industry. Nanometer to micrometer sized SiO<sub>2</sub> particles are also formed in these plasmas. Another important category of plasma where strong powder formation can be observed is hydrocarbon plasmas. These plasmas find wide applications in plasma polymerisation and in the production of hard carbon coatings.

Various diagnostics have been applied to investigate powder formation. These include in-situ particle diagnostics and diagnostics covering the plasma composition and parameters. Mass spectrometry, infrared absorption spectroscopy and emission spectroscopy have been applied in order to elucidate the origin and the different phases of the powder development and powder composition as a function of various external parameters and monomer types.

From the point of view of the production of nanoparticle-seeded coatings, diagnostic methods measuring nanometer sized particles and their density are needed. Besides specialised methods such as the laser explosion technique, no in-situ methods are available to measure the size and density of sub-nanometer sized proto-particles. Such a diagnostic would be of great interest for understanding the transition from large clusters to proto-particles.

#### **In-situ powder diagnostics by cavity ring down techniques**

The cavity ring down technique has been applied to investigate powder formation in pure silane plasmas, diluted HMDSO plasmas and pure methane plasmas. The change in the ring down time of the cavity originates from absorption of different origins. Besides photodetachment of negative ions and line absorption due to electronic excitation, the main losses of the circulating laser beam are due to absorption by nanoparticles and scattering. The extinction due to small particles is well described by Rayleigh scattering theory and varies as R<sup>6</sup> (R is the particle radius) whereas absorption depends on R<sup>3</sup> (volume fraction) and on the refractive index. In general, absorption is the dominating effect for very small particles such as silicon- and carbon-containing particles. However the SiO<sub>2</sub> particles must be treated as non absorbing due to the very small imaginary part of this index of refraction in the visible spectrum.

The time development of powder formation in diluted Silane, HMDSO and methane plasmas has been measured. In each case the scattered intensity at 135° and the

single pass extinction of the Ar-ion laser beam were simultaneously monitored. The appearance of any scattered intensity indicates the presence of powder particles in the range of about 40-50nm. Figure 2.6.12 shows the formation of particles in a pure methane plasma. In a cleaned reactor the powder formation lasts for about a few hundred seconds. In a contaminated reactor, powder appearance is much faster, since powder formation could be induced by particles deposited on the electrodes or from contamination from the reactor walls. From our experiments it can be concluded that contamination may strongly influence powder formation and care must be taken to avoid artefacts. The particle size and particle number density were determined by assuming that absorption dominates for very small particles and constant volume fraction during the development. The particle size can be estimated from the ratio of the extinction due to absorption measured early in the particle development, to the measured absorbance proportional to  $R^3$  and from this the number density can finally be obtained. For the case of  $\text{SiO}_2$  particles this estimation cannot be applied due to the non-absorbing character of the particles. In this case only the behaviour of  $NR^6$  can be assumed. For larger particles, scattering is the dominating process. This leads to an increased extinction and therefore large particles even at low density might strongly influence the absorbance and dominate over the contributions from small particulates. In Fig. 2.6.12 the presence of a few large particles is indicated. These large particles arrive near the plasma sheath due to rearrangement of the powder, as was observed visually.

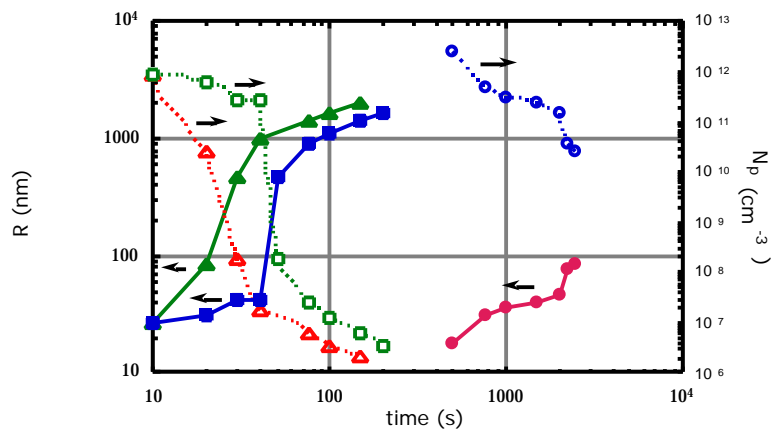


**Fig. 2.6.12** Powder formation in pure methane plasmas. Particle size and density for cleaned reactor (circles), after two (squares) and four (triangle) time developments of the powder formation.

Figure 2.6.13 shows the absorbance in an argon-diluted HMDSO plasma. In these plasmas, first indications of powder formation appear after about 50 seconds. However, adding 0.7sccm oxygen, very fast powder formation is observed. The cavity ring down technique was applied to determine the negative ion density in oxygen plasmas using photodetachment. These investigations show that the electronegativity of the oxygen leads to a large fraction of negative charge carriers being negative ions. Therefore a lot of negative charges must be negative ions in a dusty electronegative plasma. This leads to a further reduction of the particle charge and its consequences on the coagulation (larger particles) and powder dynamics (larger neutral forces and smaller electrostatic forces). It was found that  $\text{SiO}_2$  particles in these plasmas are in the range of 400-500nm, whereas powder

particles in other reactive plasmas such as silane plasmas are typically only around 100 to 200nm; this is a consequence of reduced charging of the particles in these plasmas.

In the case of powder formation in very low power argon diluted silane plasmas, periodically varying absorbances have been observed. These oscillations are characteristic of powder creation/growth/elimination cycles in the reactor as already shown by other diagnostics. However, at low silane dilutions the cavity ring-down signal is rapidly lost. The absorbance presented in Fig. 2.6.13 follows an exponential law. Contrary to  $\text{SiO}_2$ , amorphous silicon shows considerable absorption at the dye laser wavelength and the beam attenuation is determined rather by absorption than by scattering losses. The absorbance signal can therefore be interpreted for particle sizes up to about 40nm (roughly the Mie scattering onset) as the total volume fraction of the powder in the plasma. An exponential increase of the volume fraction can be explained by a simple model in which the total number of particles is influenced by coagulation and growth because of the dependence of the coagulation process on the volume and the total number of particles remains unaffected by the coagulation. So far most theories applied to the coagulation in the plasma assume constant volume fraction. In order to interpret the measurements, more sophisticated theories including simultaneous nucleation, condensation and coagulation in the plasma should be applied. A model including the simplest particle forming system by gas to particulate conversion allowed us to describe the dynamic behaviour of such a system. In addition the influence of the negative ions on the charging of the particles needs clarification since charging influence not only the coagulation and the expected size, but also the governing forces on the particles and therefore the powder dynamics. For powder formation and for powder processing important information on changes in the polydispersity due to the coagulation might be obtained.

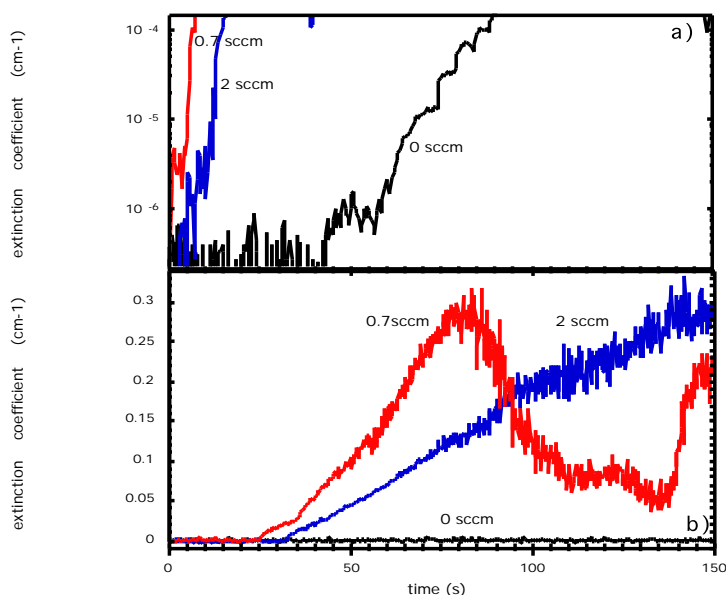


**Fig. 2.6.13** Addition of oxygen to an argon diluted HMDSO plasma (15sccm Ar, 2sccm HMDSO) a) attenuation coefficient from cavity ring down

*method, b) attenuation coefficient determined from Ar ion laser beam (single pass).*

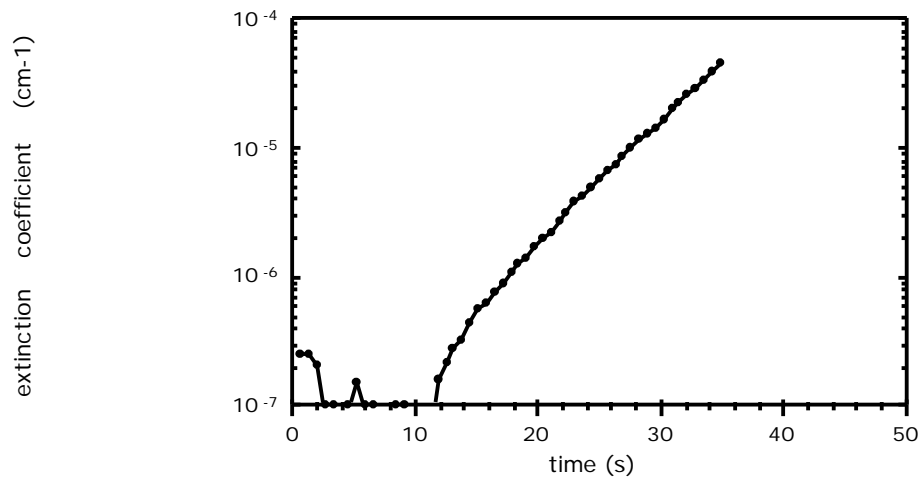


**Fig. 2.6.14** *Extinction coefficient in an argon-diluted silane plasma (500sccm argon, 15.4 silane, 10W and 0.2T).*

### **2.6.6 Industrial mandates**

Several industrial mandates were concluded during 1999. These mandates involve essentially basic research and development of new processes or improvement and control of existing plasma processes. A mandate ordered by BPS (Balzers Process Systems), one of the world leading manufacturers of CD producing equipment, aimed the basic understanding of the RF magnetron discharge, in order to increase the substrate throughput respectively the CD production yield.

The mandate worked on for Balzers Wear Protection was directed toward novel diamond processing for tribological applications. In the frame of this mandate a diploma work on advance diamond processing was performed in collaboration with the Technical University of Vienna.

Plasma processing of SiO<sub>x</sub> coatings as permeation barrier in packaging was a mandate for TetraPak R&D Plasma Technology in Romont. Basic understanding of plasma chemistry and physics and process control were of prime interest. A PhD student was working partly at Tetra Pak.